Scuola Normale Superiore di Pisa
Classe di SCIENZE
Corso di Perfezionamento in Chimica

Dissertation in Doctor of Philosophy

Multigrid QM/MM approaches in *ab initio* molecular dynamics

AUTHOR
Teodoro LAINO

SUPERVISOR
Prof. Michele PARRINELLO

SUPERVISOR
Dott. Alessandro LAIO

ACADEMIC YEAR 2002/2006

Scuola Normale Superiore di Pisa, Pisa 2006
This document was edited with LaTeX
Active hyper-references in the electronic version
by Teodoro LAINO

Index

Part I QM/MM Methods 3

1 Introduction . . . 5

2 QM/MM : an overview . . . 9
- 2.1 The explosion of QM/MM applications . . . 9
- 2.2 General definitions . . . 9
- 2.3 Overview of QM/MM schemes . . . 11
  - 2.3.1 Additive Schemes . . . 11
  - 2.3.2 Subtractive Schemes . . . 12
- 2.4 QM and MM models. How to choose the best one? . . . 13
  - 2.4.1 The choice of the quantum model . . . 13
  - 2.4.2 The choice of the classical model . . . 14
- 2.5 Electrostatic Terms . . . 14
- 2.6 QM/MM boundary . . . 15
  - 2.6.1 Coordinates and Forces of capping sites . . . 17
  - 2.6.2 Modifications of charge distributions at the boundary . . . 19
- 2.7 Variational and Energy conserving schemes . . . 21
- 2.8 Available Software Implementations . . . 21

Part II Overview of QM and MM methods 23

3 Density Functional Theory: An overview . . . 25
- 3.1 Introduction . . . 25
- 3.2 Gaussian and plane waves method . . . 26
  - 3.2.1 Energy functional . . . 26
  - 3.2.2 Pseudo potentials . . . 27
  - 3.2.3 Electrostatic energy . . . 28
  - 3.2.4 Exchange–Correlation Potential . . . 30
- 3.3 GPW forces . . . 34
  - 3.3.1 Deriving the Kohn-Sham matrix from the GPW energy . . . 34
  - 3.3.2 Forces on the ions . . . 35
- 3.4 Basis sets . . . 37
- 3.5 Conclusions . . . 38

4 Molecular Mechanics: Overview . . . 39
- 4.1 Introduction . . . 39

4.2 Potential Functions (Force field) . . . 40
4.2.1 Bonded Potentials . . . 40
4.2.2 Non-bonded Potentials . . . 42
4.3 Molecular Dynamics . . . 44

Part III Theoretical QM/MM Methods 47

5 Regularization of the electrostatic coupling . . . 49
5.1 Introduction . . . 49
5.2 QM/MM Hamiltonian . . . 50

6 An efficient real space multi-grid QM/MM electrostatic coupling 57
6.1 Introduction . . . 57
6.2 Wave-function Optimization . . . 58
6.2.1 GEEP: Gaussian Expansion of the Electrostatic Potential . . . 59
6.2.2 GEEP library . . . 61
6.2.3 Multi-grid Framework . . . 61
6.3 QM/MM Energy . . . 62
6.4 QM/MM Energy Forces . . . 64
6.5 Results and Discussion . . . 66
6.6 Conclusions . . . 67

7 Periodic boundary conditions in QM/MM simulations . . . 69
7.1 Introduction . . . 69
7.2 Methodology . . . 70
7.2.1 Ewald lattice summation for electrostatic interactions . . . 72
7.2.2 QM/MM periodic potential . . . 73
7.2.3 Periodic coupling with QM images . . . 74
7.2.4 QM/MM forces . . . 75
7.3 Tests and Applications . . . 76
7.3.1 Analytical test . . . 76
7.3.2 SiO_2 . . . 78
7.4 GLY-ALA . . . 80
7.5 Conclusions . . . 80

Part IV Applications 81

8 A Quickstep-based QM/MM approach for silica . . . 83
8.1 Introduction . . . 83
8.2 Method of calculations . . . 84
8.3 Validation of the QM/MM approach . . . 86
8.3.1 Geometry of the 6-member ring in α-quartz. . . . 86
8.3.2 Formation energy of an oxygen vacancy in α-quartz. . . . 88
8.3.3 Molecular dynamics . . . 90
8.4 Conclusion . . . 91

9 Migration of positively charged defects in α-quartz 93
9.1 Introduction 93
9.2 Methods 95
9.3 Results and discussion 96
9.3.1 Equilibrium Geometries 96
9.3.2 Migration path energy profile 99
9.3.3 Charge analysis and energy levels 100
9.4 Conclusions 101

10 Conclusions 105

Part V Appendices 107

A Gaussian Distributions 109
A.1 Gaussian product rule 109
A.2 Coulomb Interaction Integrals 109

B Efficient mapping of product Gaussian on the real space grid . . . 113

C Construction of the model charge density 115

D Derivation of the long-range QM/MM potential 117

E Derivation of Coulomb potential for delocalized point-like charges 119

F Splines 121
F.0.1 Multi grid 121
F.0.2 Periodic uniform splines 122
F.0.3 Periodic prolongation/restriction 122
F.0.4 Non-periodic uniform splines 125
F.0.5 Non-periodic prolongation/restriction 128

Bibliography 129

List of Figures

2.1 Publication and Citation analysis 10
2.2 QM and MM System representation in QM/MM schemes 11
2.3 Labeling of atoms in the link atom region 16

3.1 Hartee energy dependence with respect to PW cutoff 29
3.2 Behavior of n and v^{xc} with the BLYP functional 32
3.3 Error in energy and forces due to E^{XC} wiggles 33

5.1 Behavior of several electrostatic interaction potential 51
5.2 Relative Error of electrostatic interaction potential compared with 1/r 54

6.1 GEEP scheme 60
6.2 Collocation within GEEP 63
6.3 QM/MM :Relative error on derivatives 65
6.4 QM/MM :Energy conservation of 3 H_2O 66
6.5 QM/MM :Pair correlation function of water 67
6.6 QM/MM :Pair correlation funtion of ALA-GLY 68

7.1 Decomposition of the QM/MM electrostatic energy within PBC 71
7.2 FCC lattice of Gaussian charges 77
7.3 QM cluster of silicon atoms 79

8.1 Structure of the small Si-O cluster 86
8.2 Si-O cluster with a six-membered ring 87
8.3 Comparison of full QM, MM and QM/MM geometries 87
8.4 Structures of several QM clusters with oxygen vacancy 89
8.5 MD analysis of Si-O system 92

9.1 QM subsystem 96
9.2 Local minima of the charged oxygen vacancy in SiO_2 97
9.3 Optimized Geometries 98
9.4 NEB optimized path 100
9.5 Charge levels along the migration path 101
9.6 Density of states for the E'_δ, E'_1 and $E^\star_1$ 103

F.1 The N^3 function 123
F.2 Parametric cubic splines weights close to the border and x(u) 126
F.3 The border functions $M_{0..2}$ as function of x. 127

List of Tables

6.1 Amplitudes and coefficients of the optimal Gaussians 60

7.1 Interaction energies for the FCC lattice 77

8.1 RMSD of the MM structure and the QM/MM is SiO_2 88
8.2 Energy and geometrical data w.r.t. the size of QM and MM regions . 90
8.3 Energy and geometrical data w.r.t. different basis sets 90

Abstract of the Dissertation

Multigrid QM/MM approaches in *ab initio* molecular dynamics

by

Teodoro LAINO
Doctor of Philosophy in Chimica
Scuola Normale Superiore di Pisa, Pisa, 2002/2006

The seeds of contemporary quantum chemistry were sown as early as 1930, a mere three years after Heisenberg postulated his uncertainty principle but their high computational intensity precluded applications until mid-1960s, when computers were used to simulate the function of proteins and their chemical reactions. These calculations were based on molecular mechanics (MM) techniques derived from Newton's laws of motion.

However classical molecular mechanics (MM) methods cannot describe the electronic changes during a reaction, and are ill-equipped to address ligand-receptor interactions in systems containing metals. *Ab initio* quantum mechanics (QM) is required to study reactive chemistry or interactions involving transition metals in a protein environment. However, even with today's computer technology, full QM calculations of entire proteins are still intractable. An ideal way of simulating a large realistic system would be an embedding of a quantum mechanical calculation into a classical molecular mechanics model of the environment. This alternative approach is named quantum mechanics/molecular mechanics (QM/MM) scheme.

In an hybrid QM/MM treatment, a computationally expensive method is used to describe a small portion of the full system (generally addressed as QM subsystem) while a relatively simple treatment is used to describe the rest of the system (MM subsystem). This places severe demands on the efficiency of the implementation of any QM/MM scheme. Two main bottlenecks can be identified in such calculations: one concerns the evaluation of the QM energy and derivatives while the other is associated with the evaluation of the electrostatic interaction between the QM and the MM part. Though most of the last 20 years have shown algorithmic improvements of quantum mechanical methodologies, leading to an increase of our ability in studying the electronic structure of fragments of biomolecules (e.g. an enzyme active site) or entire biosystems, no significant gains have been recorded in obtaining a fast and reliable QM/MM coupling term that avoids the use of any hierarchical method or multipole technique.

The core of this dissertation focuses on the presentation of a novel scheme, based on the use of multi-grid techniques in conjunction with the representation of the Coulomb potential through a sum of functions with different cutoffs (GEEP), to build a QM/MM coupling fast, reliable and computationally more efficient than other avail-

able versions. The overall speedup is of 1-2 orders of magnitude with respect to other PW-based implementations of the QM/MM coupling Hamiltonian [1, 2]. The lack of tuning parameters and electrostatic cutoffs makes this implementation a totally free parameter scheme, without any significant loss of accuracy. Consequently, very stable simulations can be obtained with optimal energy conservation properties. Moreover the new scheme has been designed to include the effects of periodic boundary conditions into hybrid QM/MM descriptions of chemical/biological systems, avoiding spherical truncation scheme and treating properly the long-range part of the QM/MM electrostatic potential. The effects of the periodic boundary conditions in the evaluation of the QM/MM electrostatic potential is included with a modified Ewald lattice summation. The scheme preserves the linear-scaling property of the GEEP technique and is computationally efficient.

Within a DFT framework, it is shown for the first time that the use of periodic boundary conditions together with a proper treatment of the long-range interactions is necessary for studying ordered systems at QM/MM level.

I will first summarize the state of the art related to QM/MM methods (see Chap.(2)), presenting the argument and all related problems as most abstract as possible, *i.e.* without relying on a particular quantum mechanical method.

In the second part a brief summary of the QUICKSTEP algorithm (Chap.(3)) and of the MM methodologies (Chap.(4)) is provided.

In the third part a novel method (GEEP) to calculate the Coulomb interaction between the QM and MM subsystems is explained and validated (Chap.(6)). A fully consistent periodic extension to this method is discussed and a new decoupling/recoupling scheme to calculate the electrostatic of the QM system is proposed (Chap.(7)).

In the fourth part I will present general applications to solid state physics studying different silica-based systems. In particular a first step involved the validation of the QM/MM approach both for the quantum description and for QM/MM boundary region employing small clusters of SiO_2 (Chap.(8)). A by product of this validation scheme was the discovery of the importance of the shape of the MM cluster when an electrostatic scheme with cutoff is used when computing the QM/MM electrostatic coupling. In particular for small SiO_2 clusters (described at QM level), the shape of the embedding MM cluster may have dramatic consequences, transforming the SiO_2, a well non-known insulator into a metallic conductor. The problem can be fixed in two ways: optimizing the shape of the MM cluster or using the fully periodic QM/MM coupling description.

Relying on the validation of the QM/MM model to small silica clusters we have applied the QM/MM methodology to the study of migration of charged oxygen vacancy defects in α-quartz (Chap.(9)), providing a new interpretation to controversial experimental results.

Acknowledgments

I think if any of us would honestly reflect on who we are, how we got here, what we think we might do well, and so forth, we would discover a debt to others that spans written history. The work of some known and even unknown people makes our lives easier everyday.

There are a couple of persons in my life that, for their untiring support and unlimited belief in me, deserve all my gratitude. I could not start these acknowledgments without telling how much I appreciate all the things my parents did for me. I want let them know how grateful I am and how much their support has meant to me.

However, this page is specifically designed to acknowledge those people who most notably contributed to the success of my PhD and to the content of what you will find on the next pages.

There are special mentors that I want to acknowledge due to their importance in my work. For those of you expecting torrents of reasons for the following acknowledgments I must say you will be disappointed. All the people mentioned in this page contributed somehow. For several different reasons. Many times contributing not only to my intellectual growth. Moreover in several cases the reason is not even easily trackable. So, though it may look like a shopping list, I firmly believe that each of the person mentioned here knows very well the reason why they have been named.

First and foremost I would like to thank Michele Parrinello, who believed in this project since the very beginning and actively supported research and applications. For being directly involved into this work: Fawzi Mohamed, Alessandro Laio, Will I-Feng Kuo, Davide Donadio, Federico Zipoli, Marco Bernasconi, Joost VandeVondele, Juerg Hutter, Christopher Mundy.

My gratitude to the great fellowship I worked with in the last years. Daniele Passerone, Paolo Raiteri, Francesco Gervasio, Yves Mantz, Federica Trudu, Oliviero Andreussi, Davide Branduardi, Matthias Krack, Giovanni Bussi.

I want to express my gratefulness to the full group at SNS and in particular to Fabio Beltram, Valentina Tozzini, Paolo Giannozzi and Riccardo Nifosí.

Finally my thanks to Alessandro Cerri and Roberto Fioravanti, for reasons not directly connected to this thesis.

A Roberto,
Parce que l'essentiel est invisible pour les yeux.

List of Notations

E^{O}_{MM} : Energy of the MM subsystem 11
$E^{I,L}_{QM}$: Energy of the QM subsystem including link atoms 11
$E^{I,O}_{QM/MM}$: QM/MM energy coupling terms 11
$E^{I,L}_{Corr}$: QM/MM energy corrections term 11
$E^{O,B}_{MM}$: MM energy with a QM/MM boundary region 12
$E^{I,B}_{QM}$: QM energy with a QM/MM boundary region 12
$E^{I,O,B}_{QM/MM}$: QM/MM interaction energy with a boundary region 12
E^{E}_{MM} : MM energy of the entire system 12
$E^{I,L}_{MM}$: MM energy of the QM subsystem 12
DFT : Density Functional Theory 13
CAS : Complete Active Space 13
$TDDFT$: Time dependent DFT 13
ACA : Adjusted Connection Atom 16
SCF : Self Consistent Field 15
$LSCF$: Local Self Consistent Field 16
DRF : Direct Reaction Field 15
GHO : Generalized Hybrid Orbital 16
$IMOMM$: Integrated Molecular Orbital and Molecular Mechanics 17
GPR : Gaussian Product Rule 109
F_0 : Boys Function of the first order 110
FFT : Fast Fourier Transform 25
XC : Exchange Correlation functional 30
LSD : Local Spin Density 95
PW : Plane Waves 13
GTO : Gaussian Type Orbitals 59
$DIIS$: Direct Inversion in the Iterative Subspace 96
GGA : Generalized Gradient Approximations 30
$BSSE$: Basis Set Superposition Error 89
RI : Resolution of Identity 25
$GAPW$: Gaussian Augmented Plane Waves 26
GHO : Generalized Hybrid Orbitals 16

Part I

QM/MM Methods

Chapter 1

Introduction

Fueled by breakthroughs in both hardware and algorithm development, the past few decades have witnessed an explosive growth in computational power, which has led to remarkable advances in various fields of science and technology such as the mapping of the human genome.

It also set the stage for addressing even more ambitious goals, many of which could not be achieved through hardware developments alone. Because conventional modeling strategies are typically based on single physical descriptions, they are simply unable to capture the relevant phenomena occurring over many space and time scales. Problems of this type include modeling space weather (where plasma kinetics meets magneto-hydrodynamics), materials science (where ab initio molecular dynamics meets solid mechanics), distributed network performance (where discrete event dynamics meets stochastic fluid models), and nanodevice electronics (where quantum kinetic theory meets quantum hydrodynamics).

Therefore the modeling of complex solid state - biological systems is nowadays still a daunting challenge. The validity of sophisticated first principle methods is not seriously disputed, but their high computational intensity precluded the extensive use until the 1990s. Although computers had been used to simulate the function of proteins and their chemical reactions since the mid-1960s, these calculations were based on molecular mechanics (MM) techniques derived from Newton's equations of motion, that operate at the level of molecules rather than electrons.

However, the weakness of MM methods is that they rely on making simple assumptions. For example, electrons are not considered directly, but are assumed to be in an optimum state determined by the location of their atomic nuclei. MM methods model the full molecule with classical potentials like stretching, bending and torsion together with a fixed or polarized electrostatic description of the effective atomic charges and with an additional dispersive term very often modeled with a Lennard-Jones potential. This works reasonably well in several important cases (proteins, organic and inorganic crystals) but fails to describe reactions that involve binding or recognition in solution, as occurs in most crucial reactions in biology. Most reactions in nature involve bond formation and breaking, with associated changes in electron organization that cannot be described accurately through classical potentials because of the implicit quantum nature of the phenomena. Similarly, reactions involving docking or molecular recognition in solution require the calculation of polarization effects which are determined by the behavior of their orbitals.

Whenever electrons need to be considered explicitly, quantum mechanical (QM) methods steps in. The same is true for studying reactions that involve the recognition

of light (such as in the retina) or stimulation by light (as in photosynthesis), because these processes involve the excitation of electrons. QM methods, which are often named *ab initio* because they are based on first principles without using empirical techniques, also reveal the dynamics of reactions as they are taking place. They make possible to determine and analyze intermediates, such as radicals and oxidation states of metal ions, that exist transiently before the finished products of the reaction are formed.

While significant progress has been made in the development of quantum chemical approaches for large systems [3, 4], it is clear that to shed light on many biological processes we still need to exploit the integration of different computational chemistry methodologies with differing accuracies and costs.

By embedding a quantum mechanics calculation in a classical molecular mechanics model of the environment, the hybrid QM/MM schemes attempt to incorporate environmental effects at an atomic level, including as mechanical constraints, electrostatic perturbations and dielectric screening. Since the first published example from the field of computational enzymology [5], many QM/MM schemes have been implemented and applied in a wide variety of chemical applications.

Traditional mono-methodological approach have proven to be inadequate because of the range of scales and the prohibitively large number of variables involved. However, combining QM/MM with other classical techniques focusing on a small number of crucial variables has proved to be the winning strategy and QM/MM methods are, nowadays, closely identified with the successful technology in the molecular simulation field. Since the early landmark study of Warshel and Levitt [5] (they were the first to employ QM/MM hybrid Hamiltonians) many articles proved and validated this class of hybrid methods (see Chap.(2)).

Despite the large amount of published data none of the QM/MM related papers focused on the computational efficiency of the Hamiltonian coupling term, that can be easily comparable to the cost of the QM calculation. In the present dissertation we address this problem and describe a new QM/MM technique based on the use of multi-grids framework in conjunction with the representation of the Coulomb potential through a sum of functions with different cutoffs, derived from a Gaussian expansion of the electrostatic potential (GEEP for short). The QM/MM implementation we introduce is based on the quantum mechanical program QUICKSTEP and the molecular mechanics driver FIST (both part of the CP2K package). The method itself, through the use of a modified Ewald lattice summation, includes the effects of the periodic boundary conditions in the evaluation of the MM electrostatic potential.

The present implementation makes almost negligible the computational cost of the electrostatic coupling between the QM and the MM subsystems and moreover the use of a GPW (see Chap.(3.2)) scheme makes feasible the treatment of several hundreds of atoms at DFT level on commodity clusters.

The main rule to keep in mind is that any hybrid QM/MM methods represent a compromise, and so require judicious application in order to keep accuracy under control. *I would say that the reliability of any QM/MM simulation strongly depends on the skills and thoroughness of the researcher doing the work, particularly during the planning/testing phase of the simulations*, said Markus Dittrich from the University of Illinois at Urbana-Champaign, USA, who applies such methods to analyze ATP hydrolysis. *Once all the necessary steps have been taken, QM/MM simulations can*

give meaningful qualitative results, in some cases even quantitative ones. Inevitably, this requires extensive testing and benchmarking for each system.

Chapter 2

QM/MM : an overview

In this chapter we provide an overview of hybrid QM/MM (quantum mechanics / molecular mechanics) calculations. We consider the choice of QM and MM methods, the construction of the total QM/MM potential energy, the nature of the QM/MM coupling, and the treatment of bonds between QM and MM regions. Recent reviews, on the variety of ways in which QM and MM calculations can be combined, include those by Gao [6], Thiel [7] and Sherwood [8].

2.1 The explosion of QM/MM applications

Since its birth QM/MM has steadily developed and the last couple of years have seen a rapid increase in the rate of publications of QM/MM applications. It is significant to show what is the amount of papers since the first pioneering work of Warshel and Levitt [5] that use in the title or in the abstract the word "QM/MM " and in the same time what is the number of publication that cite reference [5], that is considered the starting point of all QM/MM related technologies and applications. In Fig.(2.1), we show the number of publications citing the work of Warshel and Levitt (in gray). Since 1976 and for the 20 years later the number of publications was constant at about 30 articles per year. But if we look at the number of articles citing the word QM/MM or QM-MM (in the title or in the abstract) we see that this number is exponentially increasing in the last years, and no article citing these labels has been published until the first 90s [1]. In the 20 years covering the middle 70s-90s much work has been done to validate QM/MM methods, and definitely the exponential growth in the last years is due to the interest on these technologies by Life Science disciplines. At the moment this class of computational methods represent one of the most powerful tools to solve the big computational challenges in molecular biology and biophysics. Last but not least, one reason for the slow uptake of the QM/MM methods has been the computational cost, but the present high availability of computational power has renewed attention to these methodologies.

2.2 General definitions

The first step in a QM/MM approach is to divide the entire system (E), into inner (I) and outer (O) regions and into a link part (L) between the two subsystems. The QM description is used to model processes in the inner region and the MM description is used to model the outer region. As always the devil is in the details, and it

[1] [9] is the most cited article among publications citing the word QM/MM .

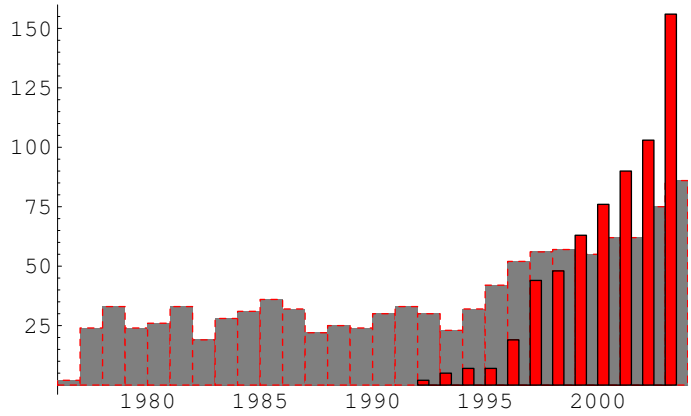

Figure 2.1: In red number of Publications that since the 1976 (the first work based on QM/MM techniques) used the word QM/MM or QM-MM in the title or in the abstract. In gray the number of publications that cite the work of Warshel and Levitt [5]. The analysis is based on ISI web of SCIENCE.

is rarely possible to simply write down the total energy in terms of two, non overlapping subsystems. Very often the interactions between the systems are so strong (the obvious example being the presence of a chemical bond across the two regions) that the reliability of QM calculations restricted to the inner region may be no longer guaranteed. One would like to determine the optimal size of the QM system, in order to minimize this strong interaction and to avoid that a wrong description deprecates the full calculation. The question is quite simple but there is no general answer. The fact is that when applying QM/MM methodologies to new systems (where no general recipes are available in literature) many factors needs to be tested to validate the method itself on that peculiar case. A good chemical know-how gives most of the times a good starting point for the choice of the QM system. Nevertheless some form of termination, or treatment of the boundary is generally required. We can classify the approaches to the QM termination problem into two main groups:

- ⋆ those based on **Capping atoms** [10, 9], additional centers added to the QM calculation but not present in the entire system (E), to saturate the free valence of the QM boundary atoms due to the partitioning of the system. We will refer to **capping atom** as the atom used to satisfy the valence requirements of the QM region and allows for a standard electronic structure calculation to be performed on the QM fragment. It is important to realize that the capping atom is not part of the real system, but is simply an atom that is introduced to truncate the electronic system of the QM region. For every link bond there are three atoms of importance, the capping atom and the two atoms that are part of the real link bond (one from QM region and the other from the MM region). From this point on, we will refer to the MM atom that is part of the real link bond as the **link atom**. It is this atom that is replaced by the capping atom in the electronic structure calculation of the QM model system. The position of capping atoms in the region (L) are either viewed as independent variables or as a function of the positions of atom in both (I) and (O) regions. Capping atoms are generally

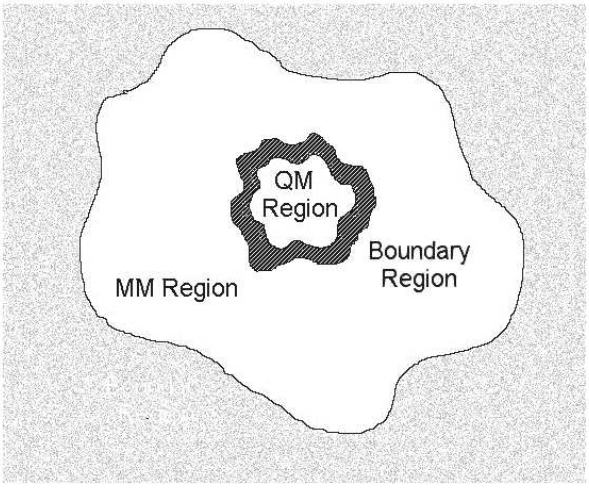

Figure 2.2: QM and MM System representation in QM/MM schemes. The shaded region between QM and MM part represents the QM/MM link part (L), that needs special care (see Sec.(2.3))

invisible to the MM calculations;

- those having a **boundary region**, with both QM and MM features. This boundary region can be described in several different manner, ranging from a re-parameterized semi-empirical Hamiltonian, to an optimized monovalent pseudo-potential or frozen hybrid orbital.

2.3 Overview of QM/MM schemes

According to the form of the interaction Hamiltonian, we can further group QM/MM schemes into two broad classes:

2.3.1 Additive Schemes

For capping atom based schemes (E = entire ; I = inner (QM); O = outer (MM); L = link) the total energy expression takes the form of :

$$E^{E}_{QM/MM} = E^{O}_{MM} + E^{I,L}_{QM} + E^{I,O}_{QM/MM} - E^{I,L}_{Corr} \tag{2.1}$$

where the term E^{O}_{MM} is the energy the MM subsystem, $E^{I,L}_{QM}$ is the energy of the QM subsystem including capping atoms in the QM description, $E^{I,O}_{QM/MM}$ is the QM/MM coupling term, including all terms that couple the two regions, for example MM-style bonding and Van der Waals interactions and modifications to the QM Hamiltonian to reflect the influence of some or all of the atoms in the outer region.

The correction term $E^{I,L}_{Corr}$ represents terms designed to reduce the dependency of the total energy on the nuclei in the link atom region [11]. How this term is handled depends on the choice of link atom coordinates, as discussed in Sec.(2.6.1). However, in most of the cases, this term is often neglected.

Additive schemes are probably the most widely adopted QM/MM approach, particularly in the biomolecular field, AMBER [10, 12, 13] and CHARMM [9, 14, 15, 16] based implementations being important examples.

The main problems within this scheme is the accurate computation of the coupling term $E^{I,O}_{QM/MM}$, in the presence of the capping atoms [17], particularly if electrostatic perturbations to the QM Hamiltonian are included. This problem is due to the presence of the atoms added to the QM subsystem to saturate the dangling valence of the QM boundary atoms. So whenever one computes the electrostatic interaction energy between the QM and MM subsystems one takes in consideration also the charge density due to the electron and nuclei of the capping atoms.

Boundary-region based methods (E = entire; I = inner (QM); O = outer (MM); B = boundary), are usually intrinsically additive. The total energy can be written as

$$E^{E}_{QM/MM} = E^{O,B}_{MM} + E^{I,B}_{QM} + E^{I,O,B}_{QM/MM} \tag{2.2}$$

where $E^{O,B}_{MM}$ is the MM energy of the system including the QM/MM boundary atoms, $E^{I,B}_{QM}$ is the QM energy including the same set of boundary atoms and $E^{I,O,B}_{QM/MM}$ contains all coupling terms (electrostatic, Van der Waals, etc.). There is no need for any link atom corrections, but since the boundary atoms are treated both by QM and MM methods it is important that the classical energy expression is modified to avoid multiple counting of interactions. This class of schemes has been adopted most widely for studies involving strongly ionic materials where boundary region is treated by model- or pseudo-potential. However, as we will show in the later sections, a number of treatments designed for covalent systems also eliminate capping atoms, placing a re-parameterized atomic description or a frozen orbital at the site of the first MM atom.

2.3.2 Subtractive Schemes

In this scheme the entire system is first treated by MM. Then a calculation on the inner region including capping atoms is performed with QM techniques and finally a third calculation on the inner region at the MM level is used to eliminate multiple counting [11]. This approach is generally applied to capping atom based schemes, in which case the total energy can be expressed as

$$E^{E}_{QM/MM} = E^{E}_{MM} + E^{I,L}_{QM} - E^{I,L}_{MM} \tag{2.3}$$

where E^{E}_{MM} is the MM energy of the entire system while $E^{I,L}_{MM}$ is the energy of the QM part of the system, computed at the MM level of theory.

The coupling term $E^{I,O,L}_{QM/MM}$ is no longer required as all interactions between inner and outer regions are handled at the MM level of theory, in the E^{E}_{MM} term. The handling of capping atom corrections here occurs implicitly as a result of the subtraction. It is necessary that the forces in the link region arising from the difference between the QM and the MM representations ($E^{I,L}_{QM} - E^{I,L}_{MM}$) remain small for all reasonable positions of the link atoms. It is therefore particularly necessary in this case to use a classical force field parameterization able to reproduce inside the QM region the same forces obtained at the QM level of theory.

If the process under investigation involves changes in chemical bonding it will become more difficult to provide a suitable force field. However, if the inner region is

large enough, it is possible to ensure that the contribution to the total energy from atoms in the interior of the inner region completely cancels when the subtraction $E^{E}_{MM} - E^{I,L}_{MM}$ is performed, and there is therefore no requirements for the force field to model the energetics of the reaction. Nevertheless, the force field must be able to compute the interaction between the reacting center and the outer region at the MM level of theory, which requires, for example, fluctuating charges for the former. Since the charge density of the inner region may change during the course of the reaction this can be a quite demanding requirement. Subtractive schemes are clearly not suitable for cases in which the electronic structure of the QM region is expected to be significantly perturbed by interaction with the environment [18]. Where good quality force fields are available the approach can be very accurate since there are no problems with interactions between the link atom region and the classical environment. This scheme is actually quite general and can be used to couple different levels of QM theory, as exemplified by the IMOMO [19, 20] or ONIOM [21, 22] of Morokuma and coworkers.

2.4 QM and MM models. How to choose the best one?

2.4.1 The choice of the quantum model

The choice of the quantum model is essentially related to the property one wish to compute with a QM/MM method. Generally speaking the design of a QM/MM scheme is not affected by the QM method involved and its use is mostly governed by the same criteria that apply to pure QM calculations.

One of the most common QM methods, since the pioneering work of Warshel and Levitt [5], are the ones based on semi-empirical [23] Hamiltonians. These methods rely on effective Hamiltonians, parameterized through the fitting of energies and geometric data with the one obtained in experimental measures. As any parameterized method, semi-empirical have a good accuracy in treating molecules similar to the ones used for the parameterization. In general semi-empirical methods can reproduce [24, 25, 26, 27] energies and geometries of fundamental states of a large class of compounds. The low computational cost with respect to the *ab initio* techniques boosted their use especially in the field of biological applications, and for long time such schemes were likely to remain important for applications incorporating molecular dynamics. In the last years, indeed, new powerful methods based on a dual basis set expansion of the wave function, mixed Gaussian and Plane Wave (GPW), have been developed [28, 29] (see also Chap.(3)), making feasible to perform molecular dynamics studies, using Density Functional Theory (DFT) , almost at the same computational cost of a semi-empirical calculation. For molecular dynamics investigations on excited states, the use of semi-empirical Hamiltonians is still preferred to the time dependent DFT (TDDFT) formalism, due to the better representation of the excited state surface through the use of Complete Active Space (CAS) techniques, or Multi configurational ones into a semi-empirical framework [30].

A large number of *ab initio* QM/MM schemes are based on Hartree-Fock [31, 10] and DFT [32, 33] within a Gaussian basis set formalism. Recently a number of approaches based on Car-Parrinello DFT codes (using plane waves (PW) basis set) have been also introduced [34, 35, 2].

2.4.2 The choice of the classical model

The choice of the MM scheme depends on whether the additive or subtractive schemes are chosen, since within the subtractive scheme any force field can be used.

Within additive schemes, instead, the choice of the MM model may have significant influence on the treatment of the boundary, since different classical approaches differ markedly with respect to the handling of both bonded and non-bonded interactions. The most important distinction is that between:

- ⋆ **valence force field**, exemplified by the biomolecular force fields (CHARMM [36], AMBER [37]) and a number of more general purpose force fields including MM3 [38] and the consistent force field (CFF [39]) constructed from energy terms such as bond stretches, angle bends, etc. (See Chap.(4)).
- ⋆ **ionic force fields** in which the principal terms are the electrostatic and short-range (van der Waals interactions type) forces, an example is the shell model [40] or the van Beest, Kramer, van Santen (BKS) potential [41] specifically designed to describe SiO_2 bulk.

The choice of the force field determines the atomic partial charges on MM nuclei, thus affecting the long-range QM/MM interactions, as for most current implementations the same charges are used for MM$\cdots$MM and QM$\cdots$MM interactions. Moreover, the handling of bonding and close inter-ionic contacts between QM and MM regions will generally follow the same approach as the treatment of similar interactions within the MM region.

In the valence force field case it is easy to identify the terms involved, typically bond-stretch, angle-bend and torsion terms that are needed, and it is simple to delete those that correspond to terms handled by the QM interaction. For these reasons, additive schemes based on capping atoms are easier to construct with valence force fields. The ionic class of force fields can be used in boundary-region additive schemes, but only if the force field charges can generate the correct electrostatic potential in the QM region and thus the correct inter-ionic forces. This is more likely to be true for highly ionic materials, unless significant parameterization of the boundary region is carried out.

2.5 Electrostatic Terms

Bakowies and Thiel [11] defined three ways of treating QM/MM electrostatic interaction:

Model-I **mechanical embedding**, in which the QM calculation is essentially performed in the gas phase, without electronic coupling to the environment. The electrostatic interaction between QM and MM regions is either omitted or performed by the MM code, using a classical point charge model for the QM charge distribution (a potential derived charge model).

Model-II **electrostatic embedding**, in which the classical region appears as an external charge distribution (i.e. a set of point charges) in the QM Hamiltonian. The polarization of the QM region by the MM charge distribution thus occurs as part of the QM electronic structure calculation [30]. The partial charges used to describe the MM distribution are frequently taken to be those used in the force field [9], relying on the use of electrostatic properties in the force field charge derivation. Charge equilibration schemes,

which determine the MM charges as a function of geometry have also been implemented [42, 43].

In *ab initio* localized basis schemes it is clear that the electrostatic embedding scheme should be implemented, at least at long range, by adding the contribution of the MM point charges to the 1-electron Hamiltonian. However, within the semi-empirical formalism, the definition of the electrostatic potential is more ambiguous as a result of the overlap approximations used, and alternative formulations for the 1-electron integral terms have been suggested [44] [42].

Model-III **polarized embedding**, in which the polarization of the MM region in response to the QM charge distribution is also included. Intuitively this makes most sense when force fields have been explicitly parameterized with a polarization function. In fact, most unpolarized force fields implicitly incorporate MM polarization in their charge parameterization; hence they tend to overestimate the polarization effects of the MM backbone, if used in a polarized model. Then, care must be taken in using force fields explicitly developed for a QM/MM polarized embedding scheme.

A variety of models for the classical polarization are available, including the shell model [40], and coupled distributed atomic polarizabilities [45], in which the polarization on MM atoms is treated through the use of parameterized dipoles fixed on atoms. In this model, the result of the change in MM charge distribution from the classical polarization is not propagated to the QM calculation, resulting in a non variational total energy.

Model-IV **mutual polarization scheme**, is defined as an extension to the previous model, where QM and MM polarizations are made self-consistent, either by iterative solution of the SCF (Self Consistent Field) and polarizability problems [46, 47], or by matrix inversion techniques, as in the Direct Reaction Field (DRF) model [48, 49, 50, 51, 52]

The treatment of the short-range QM/MM interactions, i.e. Van der Waals, generally follows the model used in the MM calculation. Re-fitting of the non-bonded parameters is often carried out to optimize the performance of the QM/MM potential, particularly in the case of solvation studies [53, 54, 55, 56, 57] or in all that systems in which the details of non-bonded contacts are particularly important.

2.6 QM/MM boundary

If there are bonds or strong ionic interactions between the QM and MM regions it is necessary to introduce some termination in the QM subsystem, either through the capping atom or boundary region approaches. In Fig.(2.3), we show the labeling adopted in the following discussion for those models incorporating capping atoms. For termination of sites where a covalent bond has been broken addition of a capping atom is the most popular approach. An extra nuclear center is introduced, together with basis functions and electrons required to form a covalent bond to the QM region that will mimic the bond to the MM region. The simplest and still most popular choice is the use of a hydrogen atom [9], even though other monovalent (halogen atoms) atoms have used in the last years [58].

There are clearly chemical differences between hydrogen and the chemical group it replaces. Within empirical and semi-empirical schemes, an obvious enhancement

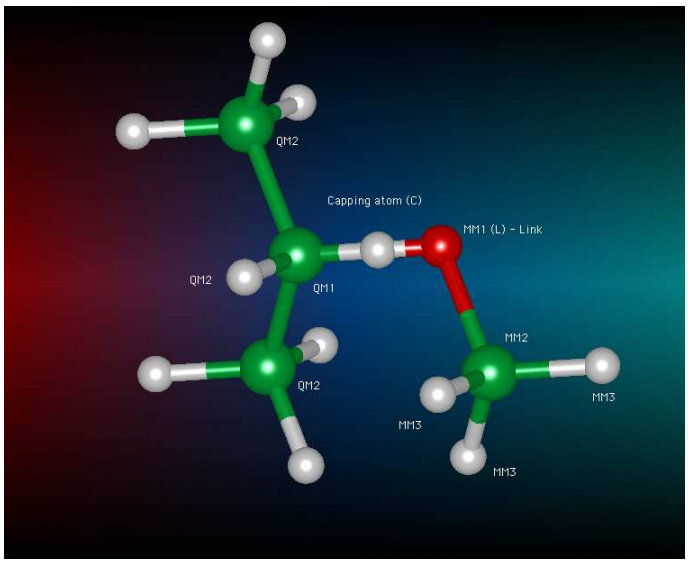

Figure 2.3: QM labels quantum atoms, MM classical atoms and L labels the capping atom.

is to adjust the capping atom parameterization to mimic more closely the modeled group. Recently, Antes and Thiel [59] have described the semi-empirical Adjusted Connection Atom (ACA) scheme, in which the link atom is replaced with a boundary atom parameterized for a single valence electron in order to model a methyl group.

A related approach within *ab initio* based QM/MM methodologies is to place a pseudo-potential at the MM site to mimic the electronic properties of the replaced bond [60]. This avoids the additional atomic center of the capping atom approach.

All the techniques listed above assume that once the termination potential has been set up, a full wave-function optimization (SCF or Conjugate Gradients type optimization) is performed on the resulting system. An alternative approach is to constrain the SCF solution to reflect the influence of the bonds that we have omitted. The local self consistent field (LSCF) scheme [61, 62] of Rivail et al. involves the preliminary calculation of the localized bond orbital, which is then frozen during the calculation. The generalized hybrid orbital (GHO) scheme of Gao et al. [63] constrains the hybridization of the terminating center but allows adjustment of the QM/MM bond itself, allowing changes in local geometry to be handled. This procedure effectively replaces the link atom with a *carbon* with three frozen and one QM active sp^3 hybrids. The QM active hybrid corresponds to half the frozen bond in the LSCF approach.

These approaches have to be considered a great improvement with respect to the atomic capping descriptions. They do not need any parameterization before the computation, *i.e.* the calculation is totally independent from the compounds to be described with QM/MM technologies. Anyway, in spite of its drawbacks, the real appeal of the capping atom approach is its conceptual simplicity, its ease of implementation, and the minimal computational costs. The various frozen orbital (LSCF, GHO) all require substantial programming for implementation. The use of a pseudo-halogen as a link atom adds several electrons to the quantum region and it does not represent a valuable choice. Instead, a one-electron carbon pseudo-potential (as the one developed

by Thiel and co-workers [59] but for *ab initio* quantum systems) [64, 65] should be the right choice to resemble the properties of the cut bond.

All these methods require special care in choosing the frontier bond. Reuter et al. [66] have found that atoms in the MM regions with large charges in close proximity to the frontier can lead to substantial errors in energy. In addition, variations in the electron population of the frozen orbital can have a significant effect on the energy of the system. Based on these findings, they conclude that: *LSCF procedures are less robust than capping atom methods but that similar results are obtained using both methods if special care is taken.*

It is then a combination between the definition of the terminating orbitals and the reparameterization of the link atom region, which allows to obtain accurate conformational energies [67].

2.6.1 Coordinates and Forces of capping sites

In contrast to the boundary atom schemes, the additional QM centers in the capping atom lead to an important ambiguity. Initial coordinates can be chosen by placing the link atom on the bond that is being terminated, but once a geometry optimization or molecular dynamics run has been started there is a number of different ways of updating the coordinates of the capping atom and of handling the forces.

Optimized Capping Atom In these approaches, the capping atom coordinates are added to the atom list used in the geometry optimization or molecular dynamics scheme, and the coordinates are free to vary [9].
Sometimes some additional force field terms may be added to favor the positioning along the M1-Q1 bond. This is particularly important when link atom corrections lead to small and unphysical forces on the link atoms.

Constrained Capping Atom In the Constrained Capping Atom approach, the capping atom coordinates are written as a function of the link atom coordinates:

$$\begin{aligned}\vec{\mathbf{R}}_{MM1} &= \vec{\mathbf{R}}_{QM1} + \alpha(\vec{\mathbf{R}}_{capping} - \vec{\mathbf{R}}_{QM1}) \\ &= (1-\alpha)\vec{\mathbf{R}}_{QM1} + \alpha\vec{\mathbf{R}}_{capping}\end{aligned} \tag{2.4}$$

α is a constant parameter. In this way the bond distance $R_{MM1-QM1}$, between QM- and MM-link atoms is defined as a fraction of the QM-link - capping atom bond distance $R_{capping}$

$$R_{MM1-QM1} = \alpha \cdot R_{capping} \tag{2.5}$$

Using Eq.(2.4) it is possible to eliminate them from the set of *free* coordinates used in the optimization or dynamics. Such an elimination is particularly interesting for molecular dynamics and for the evaluation of vibrational frequencies, which would be modified by coupling to any independent capping atom motions, producing totally unphysical results.
Since the capping atoms have non-zero forces it is necessary to add a term to the link atom forces to counterbalance the changes in the capping atom position resulting from the link atom movements. There are many capping models in the recent literature [68, 69, 70, 71], of which the IMOMM method of Maseras and

Morokuma [72] is the most representative one. In this scheme, the capping atom (C) is constrained to move along the direction (QM1) - (MM1), and this is obtained by working in internal coordinates such that the same internal coordinates were used to update the capping atoms coordinates and to define the position of the corresponding link atom (MM1). The internal coordinate force can then be obtained by adding the QM and MM contributions.
When working in pure Cartesian coordinates the same effect can be realized by using the chain rule to establish the contribution to the forces on the real atoms X_i:

$$\frac{dE}{dX_i} = \frac{\partial E}{\partial X_i} + \sum_l \frac{\partial E}{\partial X_l^{capp}} * \frac{\partial X_l^{capp}}{\partial X_i} \tag{2.6}$$

where the derivative $\frac{\partial X_l^{capp}}{\partial X_i}$ is a 3x3 matrix describing the coupling of the capping atom (X_l^{capp}) and link atom (X_i) motions as a function of the constrain term. There is a term for each atom i which appears in the definition of the position of the capping atom l [73]. This model was chosen to describe QM/MM link regions in the QM/MM driver we developed.
In a recent implementation, the Add-Remove model [74], it is the position of the capping atom (C) that follows the classical atom (MM1). This has the major advantage that one does not remove the degrees of freedom of the real classical atom, therefore the energy does not depend anymore on some arbitrary parameter α. Furthermore the real classical atom (MM1) interacts normally with the real QM system and is allowed to move in the optimization of the MM system. Then, before the QM calculation starts, the positions of the capping atom (C) is updated from the current position of the (MM1) atom. After the QM energy and gradients have been obtained, they are corrected by removing the interactions of the capping atoms: the MM interactions, which the capping atom would have with the atoms in the real (QM+MM) system if it was a classical atom, are subtracted. That is, the capping atom is added and removed. During each step of dynamics or optimization, the charges of the QM system are updated after each QM wave-function optimization cycle, and used in the next MM energy and gradients computation. This step is very important and it will be emphasized during the discussion of our QM/MM implementation though in a slightly different context (see Sec.(7.7)).
This procedure is not variational but the extension of the correction inside each SCF cycle and the computation of the derivatives of the QM charges with respect to the nuclear variables (something similar to Pulay forces in atomic position dependent basis sets) would lead to a totally variational scheme. The formalism is equivalent for multiple link bonds present at the same QM/MM interface.
When using constrained capping atoms in additive schemes some adjustment to the force field is required. The MM force constant for the angle bend (QM2-QM1-MM1) is in effect supplemented by the bending potential for the group (QM2-QM1-L), since the restoring forces acting on H are transferred to atom (MM1) as described in Eq.(2.6). Greater accuracy could be achieved by fitting a modified MM parameter to reflect the presence of the capping atom. Similar considerations apply to the torsion angles build by sequence like (QM3-QM2-

QM1-MM1) or (QM2-QM1-MM1-MM2) etc. One can also try to keep fixed the QM1-H distance, in order to tune the electronic characteristic of the termination [75].

Similar considerations apply to the boundary atom schemes. It is generally assumed, or considered as a requirement for the boundary atom pseudo-potential parameterization, that the QM calculation incorporating a model potential will generate suitable geometries for the QM$\cdots$MM bond.

2.6.2 Modifications of charge distributions at the boundary

Within all of the polarized QM/MM schemes (Model II-IV in Sec.(2.5)) the leading term in QM/MM Hamiltonian formalism (see Sec.(2.3)) is represented by the electrons interaction with MM nuclei charges (see Chap.(6)). In the simplest electrostatic model (Model-II) and for additive schemes the $\mathcal{H}^{I,O}_{QM/MM}$ can be defined in the following way

$$\mathcal{H}^{elec,static}_{QM/MM} = \sum_{\alpha} \frac{q_\alpha}{|\vec{\mathbf{r}}_i - \vec{\mathbf{R}}_\alpha|} \tag{2.7}$$

where α labels MM atoms with coordinates $\vec{\mathbf{R}}_\alpha$ and $\vec{\mathbf{r}}_i$ labels the electrons coordinates.

Problems can be expected when point charges modeling the MM region (q_α) closely approach the QM electronic charge distribution [66]. These problems (generally referred as *electronic spill-out problems*) come from the possibility for the electron density to localize on the classical point charges of the MM atoms, and it is particularly pronounced in a plane waves basis set approach [76]. In the absence of capping atoms, close approach is usually prevented by the non-bonded interaction potentials (Lennard-Jones type or 10-12 terms [77]) which are repulsive at short range. However in the region across the QM/MM boundary some adjustment to the classical charge distribution is essential, as the nearest point charges to the QM region will be at most a single bond distance away. The terminating capping atom (hydrogens or halogens), is almost superimposed on the link atom (MM1 in Fig.(2.3)). Clearly this problem will be more severe when large basis sets are used, or with a plane wave basis set, and in fact it is possible to disregard it in the semi-empirical case [9].

Antes and Thiel [47] have discussed a variety of approaches to the problem, summarized in the classification below. Some of them are applicable only in presence of a localized basis set, while others have a much more wide range of applicability.

Selective deletion of 1-electron integrals

This is a typical treatment that can be applied only to localized basis sets. For QM calculations with small basis sets the leading spurious interaction is that of the basis functions on the capping atom with the classical MM charges. Since the capping atom is an artifact of the QM/MM scheme it has been suggested that the model can be improved simply by deleting the 1-electron Hamiltonian contributions (coming from the interaction term of Eq.(2.7)) involving capping atom basis functions and the full set of MM charges [47]. This corresponds to modify the QM Hamiltonian and therefore is fully variational.

Antes and Thiel also defined a further scheme, in which all 1-electron terms are included with the exception of those that involve only basis functions on the capping atom (C) and the charge on the link atom (MM1).

Deletion of selected atomic charges

Perhaps the simplest way of dealing with charges on the nearby classical centers is to delete them from the Hamiltonian Eq.(2.7). In the original implementation of Singh and Kollman [10], any MM charge less than 4 bonds from any other QM atom was removed. An improvement of this method is to delete only MM charges at the link atom (MM1) sites [12].

The danger of these schemes is that simply deleting charges according to the connectivity will often result in a net charge, as experienced by QM atoms, of the remaining MM atoms. Such an artifact will have particularly serious effects on computed energies for processes in which the total charge of the QM region is modified, such as protonation reactions.

Many biochemical force fields have the feature that sets of neighboring atomic charges can be grouped together such that the total group charge is an integer (usually zero) [78]. This is a convenient feature for a force field as it guarantees a molecule, built by combining these charge groups, to have an integer charge without any other adjustment of the atomic parameters.

So a choice could be to neglect of all MM charges of the group containing atom (MM1) [47]. While this clearly removes some significant physical interactions, the fact that the removed charges will sum to zero will ensure that the total MM charge experienced by the QM calculation is correct. The leading term that is missing will be the dipole moment of the group containing atom (MM1).

A series of tests on protonation reactions were used to benchmark this type of scheme [47], using semi-empirical, DFT and MP2 wave-functions. The differences between the schemes were observed to be more pronounced for the *ab initio* wave-function. In particular the last deletion scheme, was found to be robust for all types of wave-functions.*Ab initio* studies using force field based on neutral groups appears to be the obvious choice.

Charge shifting scheme

In treating aluminosilicates, a different scheme has been developed [75, 79], because in the typical force field used, there is no simple subset of MM atoms that can be deleted without associating an artificial total charge with the local MM environment. The idea is to derive for each atom an electrostatic model from a sum of bipolar contributions from the bonds in which the atom is involved. This idea has been used in the past for general chemical systems, for example the MM3 force field [38] uses an electrostatic model including bond dipole terms.

Gaussian Blur

Brooks has suggested [8] that the problem of close approach of the MM charges to the QM region is largely due to the unrealistic representation of this charge distribution by a point charge. The Gaussian blur approach replaces the point charges for selected MM centers with a Gaussian charge distribution. In Chap.(5) the problem of the regularization and renormalization [2, 80] of the coulomb electrostatic interaction is addressed to remedy the non physical QM/MM coulomb interaction at short distances.

2.7 Variational and Energy conserving schemes

Another important point of QM/MM implementations is whether the scheme is variational and in particular energy conserving. If the energy of the system can be written as $\mathrm{E}(\vec{\mathbf{r}},\lambda)$, where $\vec{\mathbf{r}}$ is a set of external parameters that characterize the physical system and λ a set of wave-function parameters that describe the electronic state (i.e. molecular orbitals), we say that the energy is fully variational with respect to the electronic parameters λ if $\mathrm{E}(\vec{\mathbf{r}},\lambda^\star)$ satisfies the variational conditions for all values of the external parameters $\vec{\mathbf{r}}$:

$$\left.\frac{\partial \mathrm{E}(\vec{\mathbf{r}},\lambda)}{\partial \lambda}\right|_{\lambda_\star} = 0 \tag{2.8}$$

with the partial derivatives calculated at $\lambda = \lambda^\star$. To ensure that the variational condition Eq.(2.8) are always fulfilled, the electronic parameters must change in a particular manner as the molecule deforms. The variational conditions therefore implicitly determine the dependence of the electronic parameters $\lambda(\vec{\mathbf{r}})$ on $\vec{\mathbf{r}}$.

Carrying on the differentiation at $\lambda = \lambda^\star$ and invoking the chain rule, we obtain the molecular gradients

$$\frac{\mathrm{d}\ \mathrm{E}(\vec{\mathbf{r}})}{\mathrm{d}\ \vec{\mathbf{r}}} = \left.\frac{\partial \mathrm{E}(\vec{\mathbf{r}},\lambda)}{\partial \vec{\mathbf{r}}}\right|_{\lambda_\star} + \left.\frac{\partial \mathrm{E}(\vec{\mathbf{r}},\lambda)}{\partial \lambda}\right|_{\lambda_\star} \cdot \frac{\partial \lambda}{\partial \vec{\mathbf{r}}} \tag{2.9}$$

The first term represents the explicit dependence of the electronic-energy function on $\vec{\mathbf{r}}$; the second term represents the implicit dependence of the energy function on $\vec{\mathbf{r}}$. In case of a fully variational scheme the second term gives a zero contribution retrieving the simple well known expression for molecular gradients.

Most of the QM/MM implementations rely on variational schemes [9, 14, 15, 81, 82] though quite few non-variational approaches were presented as well [35]. Beyond being variational or non-variational we stress the importance for QM/MM codes to produce energy conserving dynamics. Even non-variational algorithms can produce conserved dynamics if the proper terms in Eq.(2.9) are taken into account. The importance of performing energy conserving dynamics stays in the possibility to compute thermodynamical quantities, i.e. compute relevant properties like free energy and entropy. The algorithms we will show in the next chapters (Chap.(6) and Chap.(7)) are all variational and energy conserving.

2.8 Available Software Implementations

In many aspects the issue governing implementation of QM/MM computer codes are similar to those associated with the individual QM and MM methods. Most of the coupling terms are readily computed using the modules implemented in either the QM or MM packages. However, it is worth giving some brief comments on some of the usual implementational issues.

1. those based on classical modeling packages, with a QM code integrated as a force field extension
2. those based on a QM packages, incorporating the MM environment as a perturbation
3. modular schemes in which a central control program is provided and a choice of both QM and MM methods is left open

Probably the most popular approach to date has been the (1), because the modeling tools present in a typical MM/MD package are well suited for manipulation of large, complex chemical systems. A good example of this approach is the series of QM implementation within the CHARMM package [9, 14, 15] However, one area in which the functionality of a traditional macromolecular program may need enhancing is the search for transition states.

Option (2) is particularly well suited when the tools required are those associated with small molecule quantum chemistry or as in the present work, a well developed QM formalism (Car-Parrinello Molecular Dynamics) in which embedding all the MM environment.

The last option (3) offers the greatest flexibility, especially when care is taken to ensure that the component packages are modified to a minimal extent, so to provide the best hope in substituting up-to-date versions of the QM and MM packages when they become available [83].

Part II

Overview of QM and MM methods

Chapter 3

Density Functional Theory: An overview

In this chapter we present the Gaussian and Plane Wave (GPW) method and its implementation in QUICKSTEP which is part of the freely available program CP2K [84]. The GPW method allows for accurate density functional calculations in gas and condensed phases and can be effectively used for molecular dynamics simulations. The computation of the total energy and the Kohn-Sham matrix scales linearly with the system size, even for condensed phase systems of just a few tens of atoms. The efficiency of the method allows for the use of large Gaussian basis sets for systems up to 3000 atoms, and the accuracy of the method for various basis sets in gas and condensed phases is excellent. A detailed review on QUICKSTEP was recently published [85].

3.1 Introduction

Density functional theory [86, 87] (DFT) is a well established method to perform electronic structure calculations. The accuracy of the method is such that many properties of systems of interest to chemistry, physics, material science, and biology can be predicted in a parameter free way. The standard computational approach to DFT is already efficient and thus appropriate for fairly large systems, currently about 100 atoms. Nevertheless, the computation of the Hartree (Coulomb) energy and the orthogonalization of the wave functions are not scaling linearly with system size, and these terms therefore dominate the computational cost for larger systems [88]. The hybrid Gaussian and plane waves (GPW) method [89] provides an efficient way to treat these terms accurately at a significantly reduced cost. We present here the implementation of this method in QUICKSTEP, which is part of the freely available program package CP2K[84].

The method uses an atom-centered Gaussian-type basis to describe the wave functions, but uses an auxiliary plane wave basis to describe the density. With a density represented as plane waves or on a regular grid, the efficiency of Fast Fourier Transforms (FFT) can be exploited to solve the Poisson equation and to obtain the Hartree energy in a time that scales linearly with the system size. Fast Fourier Transforms and regular grids are well established in plane wave codes [90] and their efficiency has recently been exploited in a similar method [91, 92, 93, 94, 95].

Another method that is based on similar concepts [96, 97] and has become increasingly popular is the so called resolution of the identity (RI) method or density fitting. Contrary to the GPW method, most RI methods expand the density in an auxiliary

basis of the same nature as the primary basis, but optimized specifically for this purpose [98, 99, 100]. Since a density expanded in plane waves can be represented on a realspace grid, there is a direct connection to methods that use numerical calculation of matrix elements [101, 102] or grid discretization and finite element methods (for a recent review see Ref. [103]).

The GPW method is most similar to methods that employ auxiliary realspace grids but differ by the choice of localized primary basis functions used to represent the wave functions [104, 105, 106, 107, 108, 109].

Periodic boundary conditions follow naturally from the FFT based treatment of the Poisson equation, and the GPW method scales linearly for three dimensional systems with a small prefactor. The GPW method seems therefore best suited for the simulation of large and dense systems, such as liquids and solids, and all recent applications of the method fall in this category [29, 110, 111, 112, 113]. For these systems, it is important to be able to efficiently perform stable molecular dynamics simulations, in order to address finite temperature effects. Plane wave codes and the basic GPW implementation presented here require that the nuclei are described using pseudo potentials. This approximation is highly accurate if e.g. Goedecker-Teter-Hutter (GTH) pseudo potentials are employed [114, 115]. An extension of the GPW method, the Gaussian and augmented-plane-wave (GAPW) method [28] allows for all electron calculations.

The extensive experience with Gaussian-type basis sets shows that basis set sequences that increase rapidly in accuracy can be constructed in a systematic way [116]. At the same time, a compact description of the wave functions is maintained, and this opens the way for efficient methods to solve for the self consistent field (SCF) equations. Furthermore, as Gaussian functions are localized, the representations of the Kohn-Sham, overlap and density matrix in this basis become sparse with increasing system size [88]. This eventually allows for solving the Kohn-Sham (KS) equations using computational resources that scale linearly with system size. We have currently only implemented methods that are scaling cubically with system size, but these have been designed to reach high efficiency for Gaussian basis sets [117].

3.2 Gaussian and plane waves method

3.2.1 Energy functional

The gist of the Gaussian and plane wave (GPW) method [89] is the use of two representations of the electron density. Such a dual representation allows for an efficient treatment of the electrostatic interactions, and leads to a scheme that has a linear scaling cost for the computation of the total energy and Kohn-Sham matrix with respect to the system size. The first representation of the electron density $n(\boldsymbol{r})$ is based on an expansion in atom centered, contracted Gaussian functions

$$n(\boldsymbol{r}) = \sum_{\mu\nu} P^{\mu\nu} \varphi_\mu(\boldsymbol{r}) \varphi_\nu(\boldsymbol{r}) \tag{3.1}$$

where $P^{\mu\nu}$ is a density matrix element, and $\varphi_\mu(\boldsymbol{r}) = \sum_i d_{i\mu} g_i(\boldsymbol{r})$ with primitive Gaussian functions $g_i(\boldsymbol{r})$ and corresponding contraction coefficients $d_{i\mu}$. The second representation employs an auxiliary basis of plane waves, and is given by

$$\tilde{n}(\boldsymbol{r}) = \frac{1}{\Omega} \sum_{\boldsymbol{G}} \tilde{n}(\boldsymbol{G}) \exp(i\boldsymbol{G} \cdot \boldsymbol{r}) \tag{3.2}$$

where Ω is the volume of the unit cell, and $\boldsymbol{G}$ are the reciprocal lattice vectors. The expansion coefficients $\tilde{n}(\boldsymbol{G})$ are such that $\tilde{n}(\boldsymbol{r})$ is equal to $n(\boldsymbol{r})$ on a regular grid in the unit cell. This choice allows for a rapid conversion between $n(\boldsymbol{r})$, $\tilde{n}(\boldsymbol{r})$ and $\tilde{n}(\boldsymbol{G})$ using an efficient mapping procedure (see App.(B)) and fast Fourier transforms (FFT).

Using this dual representation, the Kohn-Sham DFT energy expression [86, 87] as employed within the GPW framework is defined as

$$\begin{aligned} E[n] =& E^{\mathrm{T}}[n] + E^{\mathrm{V}}[n] + E^{\mathrm{H}}[n] + E^{\mathrm{XC}}[n] + E^{\mathrm{II}} \\ =& \sum_{\mu\nu} P^{\mu\nu} \left\langle \varphi_\mu(\boldsymbol{r}) \right| -\frac{1}{2}\nabla^2 \left| \varphi_\nu(\boldsymbol{r}) \right\rangle \\ &+ \sum_{\mu\nu} P^{\mu\nu} \left\langle \varphi_\mu(\boldsymbol{r}) \right| V^{\mathrm{PP}}_{\mathrm{loc}}(r) \left| \varphi_\nu(\boldsymbol{r}) \right\rangle \\ &+ \sum_{\mu\nu} P^{\mu\nu} \left\langle \varphi_\mu(\boldsymbol{r}) \right| V^{\mathrm{PP}}_{\mathrm{nl}}(\boldsymbol{r}, \boldsymbol{r}') \left| \varphi_\nu(\boldsymbol{r}') \right\rangle \\ &+ 2\pi\,\Omega \sum_{\boldsymbol{G}} \frac{\tilde{n}^*(\boldsymbol{G})\,\tilde{n}(\boldsymbol{G})}{\boldsymbol{G}^2} \\ &+ \int e^{\mathrm{XC}}(\boldsymbol{r})\, d\boldsymbol{r} \\ &+ \frac{1}{2} \sum_{I \neq J} \frac{Z_I Z_J}{|\boldsymbol{R}_I - \boldsymbol{R}_J|} \end{aligned} \tag{3.3}$$

where $E^{\mathrm{T}}[n]$ is the electronic kinetic energy, $E^{\mathrm{V}}[n]$ is the electronic interaction with the ionic cores, $E^{\mathrm{H}}[n]$ is the electronic Hartree energy and $E^{\mathrm{XC}}[n]$ is the exchange–correlation energy. The interaction energies of the ionic cores with charges Z_A and positions $\boldsymbol{R}_A$ is denoted by E^{II}. $E^{\mathrm{V}}[n]$ is described by norm-conserving pseudo potentials [118] with a potential split in a local part $V^{\mathrm{PP}}_{\mathrm{loc}}(r)$ and a non-local part $V^{\mathrm{PP}}_{\mathrm{nl}}(\boldsymbol{r}, \boldsymbol{r}')$.

The pseudo potential terms are described in more detail in Sec.(3.2.2), the electrostatic contributions to the the total energy in Sec.(3.2.3), and the exchange and correlation term in Sec.(3.2.4). Deeper comments about the linear scaling computational cost can be found in the main review on QUICKSTEP [85].

3.2.2 Pseudo potentials

An expansion of an atomic all-electron density or wave function in plane waves is computationally inefficient. However, to describe a wide range of chemically interesting events, such as bond breaking and formation, an accurate description is required only for the valence electrons. Such an accurate description can be obtained using a pseudo potential description of the nuclei. This technique is well established in the plane wave community. The GPW method use the pseudo potentials of Goedecker, Teter, and Hutter (GTH) [114, 115].

The norm-conserving, separable, dual-space GTH pseudo potentials consist of a local part including a long-ranged (LR) and a short-ranged (SR) term

$$V^{\mathrm{PP}}_{\mathrm{loc}}(r) = V^{\mathrm{LR}}_{\mathrm{loc}}(r) + V^{\mathrm{SR}}_{\mathrm{loc}}(r) \tag{3.4}$$

$$= -\frac{Z_{\mathrm{ion}}}{r} \mathrm{Erf}\left(\alpha^{\mathrm{PP}} r\right) + \sum_{i=1}^{4} C_i^{\mathrm{PP}} \left(\sqrt{2}\alpha^{\mathrm{PP}} r\right)^{2i-2} \exp\left[-\left(\alpha^{\mathrm{PP}} r\right)^2\right] \tag{3.5}$$

with

$$\alpha^{\mathrm{PP}} = \frac{1}{\sqrt{2} r_{\mathrm{loc}}^{\mathrm{PP}}}$$

and a non-local part

$$V_{\mathrm{nl}}^{\mathrm{PP}}(\boldsymbol{r}, \boldsymbol{r'}) = \sum_{lm} \sum_{ij} \langle \boldsymbol{r} \,|\, p_i^{lm} \rangle \, h_{ij}^l \, \langle \, p_j^{lm} \,|\, \boldsymbol{r'} \rangle \tag{3.6}$$

with the Gaussian-type projectors

$$\langle \boldsymbol{r} \mid p_i^{lm} \rangle = N_i^l \, Y^{lm}(\hat{r}) \, r^{l+2i-2} \exp\left[-\frac{1}{2} \left(\frac{r}{r_l} \right)^2 \right]$$

where N_i^l are normalization constants and $Y^{lm}(\hat{r})$ spherical harmonics. The set of parameters ($r_{\mathrm{loc}}^{\mathrm{PP}}$, C_i^{PP}, r_l, and h_{ij}^l) have been optimized with respect to atomic all-electron wave functions as obtained from fully relativistic density functional calculations using a numerical atomic program. The optimized pseudo potentials include all scalar relativistic corrections via an averaged potential [115], and improve therefore the accuracy for applications involving heavier elements. The emphasis in the construction of these pseudo potentials has been on accuracy, and hence these pseudo potentials are computationally demanding if a plane wave method is used, as a large plane wave basis typically is required. The GPW method is less sensitive to the hardness of the pseudo potential since the kinetic energy (see Eq.(3.3)) and the short range pseudo potential terms are computed in the Gaussian basis. The long range term can be efficiently treated as part of the electrostatic energy (see Sec.(3.2.3)), whereas the short range terms can be easily computed as two and three center overlap integrals. An extended database (H–Rn) with GTH pseudo potential parameters based on the local density approximation is available [84] for use with QUICKSTEP. In addition, parameters for the common elements have been optimized for the gradient-corrected exchange-correlation potentials of Becke, Lee, Yang, and Parr (BLYP) [119, 120, 121], Becke and Perdew (BP) [119, 122], Hamprecht, Cohen, Tozer and Handy (HCTH/120, HCTH/407) [123] and Perdew, Burke and Ernzerhof (PBE) [124].

3.2.3 Electrostatic energy

The electrostatic energy in a periodic system is defined by a conditionally converging sum in which the separate contributions of ions and electrons are infinite. All terms of the electrostatic energy are therefore treated simultaneously

$$E^{\mathrm{ES}} = \int V_{\mathrm{loc}}^{\mathrm{PP}}(r) n(\boldsymbol{r}) d\boldsymbol{r} + 2\pi \, \Omega \sum_{\boldsymbol{G}} \frac{\tilde{n}^*(\boldsymbol{G}) \, \tilde{n}(\boldsymbol{G})}{\boldsymbol{G}^2} + \frac{1}{2} \sum_{I \neq J} \frac{Z_I Z_J}{|\boldsymbol{R}_I - \boldsymbol{R}_J|} \tag{3.7}$$

using the Ewald sum method [125] as it is commonly implemented in plane wave electronic structure codes [90]. The long range part of all electrostatic interactions is treated in Fourier space, whereas the short range part is treated in real space. This separation is conveniently achieved for the ionic cores if a Gaussian charge distribution ($n_{\mathrm{c}}^I(\boldsymbol{r})$) for each nucleus is introduced and defined as

$$n_{\mathrm{c}}^I(\boldsymbol{r}) = -\frac{Z_I}{(\mathrm{R}_I^{\mathrm{c}})^3} \, \pi^{-3/2} \, \exp\left[-\left(\frac{\boldsymbol{r} - \boldsymbol{R}_I}{R_I^{\mathrm{c}}} \right)^2 \right] \quad , \tag{3.8}$$

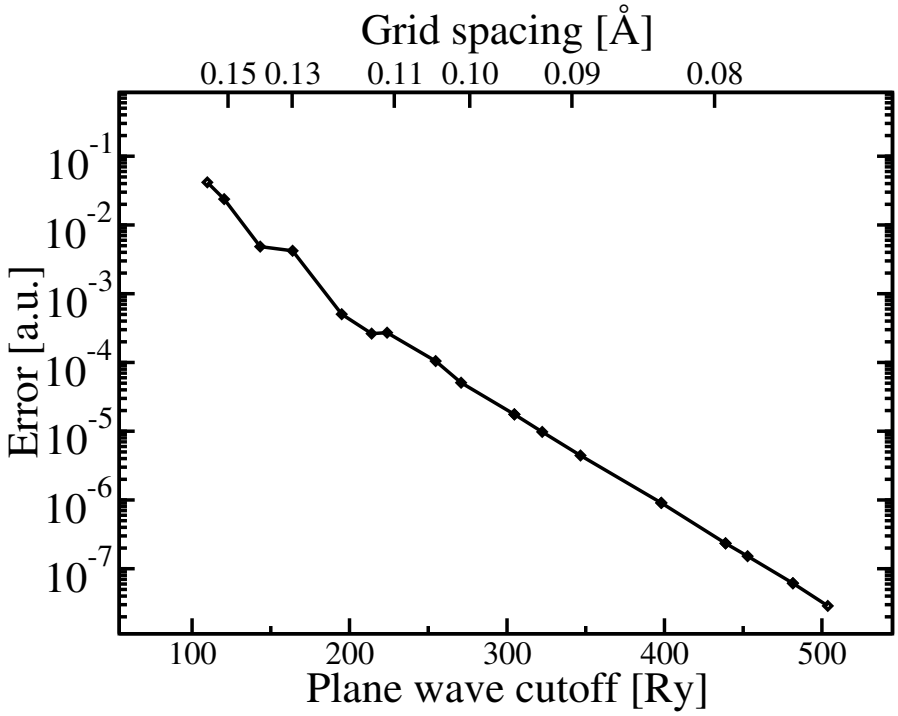

Figure 3.1: Convergence of the absolute error in the electrostatic energy Eq.(3.11) with respect to plane wave cutoff at fixed density matrix. The system is a single water molecule described with a GTH pseudo potentials and a TZV2P basis in a 10Å cubic cell. The relation $E_{\text{cutoff}} = \frac{\pi^2}{2h^2}$ is used to convert the grid spacing h to the corresponding plane wave cutoff. Figure taken from Ref. [85].

in which the parameter R_I^{c} can be chosen for optimal performance. In QUICKSTEP, this parameter is set to

$$R_I^{\mathrm{c}} = \sqrt{2} r_{\mathrm{loc}}^{\mathrm{PP}} \tag{3.9}$$

so that the corresponding potential of the Gaussian charge distribution

$$V_{\mathrm{core}}^I(\boldsymbol{r}) = \int d\boldsymbol{r'} \frac{n_{\mathrm{c}}^I(\boldsymbol{r'})}{|\boldsymbol{r} - \boldsymbol{r'}|} = -\frac{Z_I}{|\boldsymbol{r} - \boldsymbol{R}_I|} \mathrm{Erf}\left[\frac{|\boldsymbol{r} - \boldsymbol{R}_I|}{R_I^{\mathrm{c}}}\right] \quad , \tag{3.10}$$

cancels exactly the long-ranged term $V_{\mathrm{loc}}^{\mathrm{LR}}(r)$ of the local pseudo potential.

We rewrite the expression for the energy Eq.(3.7) using Eq.(3.8) as

$$\begin{aligned} E^{\mathrm{ES}} = & \int V_{\mathrm{loc}}^{\mathrm{SR}}(r) n(\boldsymbol{r}) d\boldsymbol{r} \\ & + \frac{\Omega}{2} \sum_{\boldsymbol{G}} \tilde{n}_{\mathrm{tot}}^*(\boldsymbol{G})\, v^{\mathrm{H}}(\boldsymbol{G}) \\ & + \frac{1}{2} \sum_{I \neq J} \frac{Z_I Z_J}{|\boldsymbol{R}_I - \boldsymbol{R}_J|} \mathrm{Erfc}\left[\frac{|\boldsymbol{R}_I - \boldsymbol{R}_J|}{\sqrt{{R_I^{\mathrm{c}}}^2 + {R_J^{\mathrm{c}}}^2}}\right] - \sum_I \frac{1}{\sqrt{2\pi}} \frac{Z_I^2}{R_I^{\mathrm{c}}} \quad , \end{aligned} \tag{3.11}$$

where erfc is the complementary error function, the Hartree potential $v^{\mathrm{H}}(\boldsymbol{G}) = 4\pi \tilde{n}_{\mathrm{tot}}(\boldsymbol{G})/\boldsymbol{G}^2$, and a total charge distribution $\tilde{n}_{\mathrm{tot}}(\boldsymbol{G}) = \tilde{n}(\boldsymbol{G}) + \tilde{n}_{\mathrm{c}}(\boldsymbol{G})$ has been introduced. The last three terms of Eq.(3.11) define the total Hartree energy ($E^{\mathrm{H}}[n_{\mathrm{tot}}]$), the overlap energy ($E^{\mathrm{ovrl}}$) and self energy ($E^{\mathrm{self}}$) respectively.

The two representations of the electrostatic energy Eq.(3.7) and Eq.(3.11) are strictly equivalent if an infinite sum over $\boldsymbol{G}$ vectors is employed. In practice, a difference between the two energy expressions, due to the use of finite density grids, can be observed, but this difference is rapidly converging with respect to $\boldsymbol{G}$ space cutoff i.e. the grid spacing used. The rapid convergence of the electrostatic energy Eq.(3.11) with respect to the plane wave cutoff, and thus the size of the auxiliary basis is shown in Fig.(3.1).

3.2.4 Exchange–Correlation Potential

A necessary ingredient in practical application of DFT is the introduction of an approximate exchange and correlation functional E^{XC}. In the present implementation of QUICKSTEP typical generalized gradient approximations (GGA) and meta-GGAs based on the kinetic energy density τ such as BLYP [119, 120, 121], PBE [124], HCTH [123, 126, 127], OLYP [128], TPSS [129] can be computed efficiently. These functionals have the general form

$$E^{\mathrm{XC}}[n] = \int e^{\mathrm{xc}}\big(n_\uparrow(\boldsymbol{r}), n_\downarrow(\boldsymbol{r}), \nabla n_\uparrow(\boldsymbol{r}), \nabla n_\downarrow(\boldsymbol{r}), \tau_\uparrow, \tau_\downarrow\big) d\boldsymbol{r}. \tag{3.12}$$

This form does not cover functionals where the Hartree-Fock exchange term is explicitly introduced [130, 131] such as the popular B3LYP functional[132]. Currently, no implementations of Hartree-Fock exchange can approach the efficiency with which Eq.(3.12) can be evaluated.

To compute Eq.(3.12) and its derivatives with respect to the density matrix we use a discrete representation of E^{XC} on the same uniform density grid that has been

used for the Hartree energy as is common in plane wave based calculations [133] and other grid based methods [134]. This avoids the use of the more accurate techniques employed within the quantum chemistry community [135, 136, 137] as these methods would, within the GPW scheme, dominate the total cost of the calculation by a relatively large factor.

For the evaluation of the exchange and correlation contribution, in the spin unpolarized case, the following operations are performed for each grid point:

1. computation of $n(\boldsymbol{r}) = \sum_{\mu\nu} P^{\mu\nu}\varphi_\mu(\boldsymbol{r})\varphi_\nu(\boldsymbol{r})$
2. computation of $\tau(\boldsymbol{r}) = \sum_{\mu\nu}(1/2)P^{\mu\nu}\nabla\varphi_\mu(\boldsymbol{r})\cdot\nabla\varphi_\nu(\boldsymbol{r})$
3. numerical approximation of ∇n based on the values of $n(\boldsymbol{r})$ on the grid
4. evaluation of e^{xc} and its derivatives $\partial e^{\mathrm{xc}}/\partial n$, $\partial e^{\mathrm{xc}}/\partial\nabla n$, $\partial e^{\mathrm{xc}}/\partial\tau$ on each point of the grid
5. computation of v_n^{xc} and v_τ^{xc} on the grid

$$v_n^{\mathrm{xc}} = \frac{\partial e^{\mathrm{xc}}}{\partial n} - \nabla\cdot\left(\frac{\partial e^{\mathrm{xc}}}{\partial|\nabla n|}\frac{\nabla n}{|\nabla n|}\right) \tag{3.13}$$

$$v_\tau^{\mathrm{xc}} = \frac{\partial e^{\mathrm{xc}}}{\partial\tau} \tag{3.14}$$

6. calculation of the matrix element of the sum of v_n^{xc} and the Hartree potential $v^{\mathrm{H}}(\boldsymbol{r})$ (see section Sec.(3.2.3)) between the Gaussians

$$\int \left(v_n^{\mathrm{xc}}(\boldsymbol{r}) + v^{\mathrm{H}}(\boldsymbol{r})\right)\varphi_\mu(\boldsymbol{r})\varphi_\nu(\boldsymbol{r})d\boldsymbol{r} \tag{3.15}$$

7. calculation of the matrix element of v_τ^{xc} between the Gaussians

$$\int v_\tau^{\mathrm{xc}}(\boldsymbol{r})\nabla\varphi_\mu(\boldsymbol{r})\cdot\nabla\varphi_\nu(\boldsymbol{r})d\boldsymbol{r} \tag{3.16}$$

these operations are discussed in more detail in Sec.(3.3.1) and App.(B).

The presence of terms such as

$$t = -\frac{|\nabla n|^2}{n^\alpha} \qquad \frac{\partial t}{\partial|\nabla n|} = -2\frac{|\nabla n|}{n^\alpha}. \tag{3.17}$$

in GGAs and meta-GGAs leads to very sensitive behavior in regions of vanishing density such as the tails of the atomic densities. The near singularities encountered in Eq.(3.17) are in that case customarily resolved by removing the contributions to e^{xc} and v^{xc} of the regions where the density n is lower than a given cutoff ϵ . In addition, care should be taken to fulfill numerically the exact relationship $|\nabla n| < 8n\tau$ for functionals that depend on the kinetic energy density. However, using pseudo potentials, the density can also be small in the core region, where gradients are typically larger. This is especially true for the GTH pseudo potentials that by construction have a zero pseudo charge density at the core for all elements except H. We illustrate in Fig.(3.2) that for these pseudo potentials the core region is by far the most problematic part of the exchange and correlation potential. The pronounced spike of v^{xc} in the core gives rise to small variations in the total energy as atoms move relative to the grid.

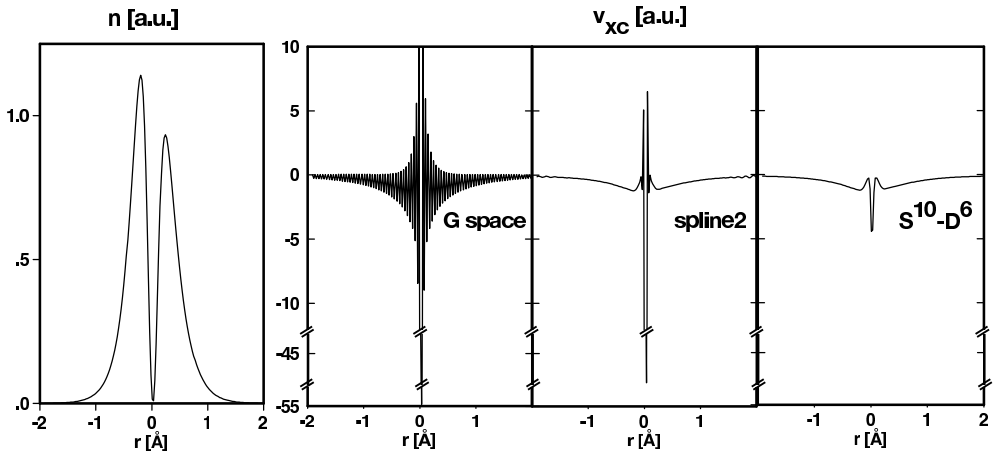

Figure 3.2: Behavior of n and v^{xc} with the BLYP functional close to the core of an O atom in a water molecule along the bisector of the HOH angle with an unusually large cutoff of 5000 Ry. The left panel shows the electron density, whereas the three right panels show v^{xc} as calculated using a derivative in $\boldsymbol{G}$ space, using a quadratic spline ($D^6(S^6)^{-1}$) and using the operators $S^{10} - D^6$ as defined in the text. It can be observed that the latter methods lead to a more physical exchange and correlation potential surface. Figure taken from Ref. [85].

The $\boldsymbol{G}$ space differentiation is commonly used in plane waves codes but is not the best choice with the GPW method. Whereas $\boldsymbol{G}$ space differentiation of the density on the grid yields the exact derivative $\nabla n(\boldsymbol{r})$ in the former case, the approximate $\nabla \tilde{n}(\boldsymbol{r})$ is obtained in the later case. When used, the differentiation of a small spike of $\partial e/\partial|\nabla n|$ in Eq.(3.13) gives rise to the strong 'ringing' effects illustrated in Fig.(3.2). Even though integration effectively filters out the highest frequencies, the energy oscillates significantly when the system is translated (see Fig.(3.3-b)).

Different schemes to compute the exchange and correlation energy more accurately were explored, and a nearest neighbor smoothing operator S^q was introduced [85]

$$(S^q f)_{i,j,k} = \frac{q^3}{q^3 + 6q^2 + 12q + 8} \sum_{l=-1}^{1} \sum_{m=-1}^{1} \sum_{n=-1}^{1} q^{-|l|-|m|-|n|} f_{i+l,j+m,k+n}, \qquad (3.18)$$

together with a smoothed finite differences operator D^q, that for the x derivative is

$$(D_x^q f)_{i,j,k} = \frac{q^2}{2(q^2 + 4q + 4)} \sum_{l=-1}^{1} \sum_{m=-1}^{1} q^{-|l|-|m|} (f_{i-1,j+l,k+m} - f_{i+1,j+l,k+m}) \qquad (3.19)$$

and likewise for the other directions.

To avoid the 'ringing' a numerical derivative that assumes less continuity can be used. $D^6(S^6)^{-1}$ calculates the derivative of the quadratic spline interpolating n on the grid. It behaves better than the $\boldsymbol{G}$ derivative, but the energy oscillations are not sufficiently reduced. D^6 alone, i.e. without sharpening step $(S^6)^{-1}$, gives information on the neighborhood rather than on the grid point itself, and damps the oscillations more, at a cost in the accuracy of the energies (see Fig.(3.3-a) and Fig.(3.3-b)).

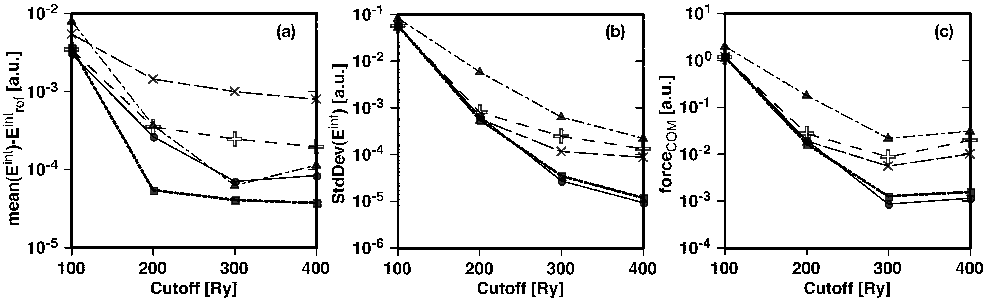

Figure 3.3: Panel (a) shows the average systematic error in the interaction energy with the BLYP functional for water dimer configurations ($\sim$ 5 kcal from the minimum), panel (b) the oscillations of the interaction energy due to imperfect translation invariance, and panel (c) the forces on the center of mass. Derivatives, and the combined n smoothing-derivative operators $S^{50} - D^6(S^6)^{-1}$ and $S^{10} - D^6$ are compared with respect to the cutoff (triangles, +, $\times$, squares and circles). The reference interaction energies were calculated with a cutoff of 2000 Ry using the usual $\boldsymbol{G}$ space derivatives. The oscillations of the energy and the magnitude of the forces on the center of mass of the last two methods are at an acceptable level for cutoffs of about 300 Ry. Figure taken from Ref. [85].

For a translationally invariant evaluation of the integral of a function f over the grid points (i, j, k) it is appropriate to associate to each mesh point not the value of the function itself, but rather an estimate of its average value in a neighborhood of (i, j, k). For a highly non-linear term such as the exchange correlation energy this average can not easily be estimated. We therefore evaluate the xc functionals using a locally averaged density $\hat{n}(\boldsymbol{r})$ employing the smoothing operator S^q. Typical values for q are 10 or 50 depending on the required amount of smoothing. Such a smoothing is equivalent with a redefinition of E^{XC} that reduces to the identity as the cutoff is increased. $\hat{v}^{\mathrm{xc}}_{\hat{n}}$ can be calculated as function of $\hat{n} = S^q\, n$ as

$$v^{\mathrm{xc}}_n = \hat{v}^{\mathrm{xc}}_{\hat{n}} \frac{\delta \hat{n}}{\delta n} = S^q\, \hat{v}^{\mathrm{xc}}_{\hat{n}}. \tag{3.20}$$

Combining the quadratic spline and D^6 derivatives with the smoothing on n brings the oscillations of the energy to an acceptable level. $S^{50} - D^6(S^6)^{-1}$ has good convergence characteristics, and implies only a small grid spacing dependent re-normalization of E^{XC}. The operator $S^{10} - D^6$ implies a significant amount of smoothing, resulting in even less grid dependence in the forces, and is fast to calculate since an inversion step is not necessary, but might be less appropriate to study systems where significant charge reorganization takes place. The exchange and correlation potentials obtained with these methods are well behaved, which also helps the convergence of the SCF procedure.

Nevertheless, none of the methods presented here is fully satisfactory, as a balance between the different accuracy goals is difficult to achieve. Non linear core corrected pseudo potentials [138] could provide a more elegant solution since the problematic region of small density would be removed. It is likely that these pseudo potentials can be treated efficiently, and they would bring additional benefits for strongly spin

polarized systems. The Gaussian and augmented-plane-wave (GAPW) method [28, 29] could also solve the issues described here in a more fundamental way.

3.3 GPW forces

3.3.1 Deriving the Kohn-Sham matrix from the GPW energy

In this section we present how the *exact* derivative $H_{\mu\nu} = \partial E/\partial P^{\mu\nu}$ of the total energy is computed taking into account all approximations that lead from the Gaussian based density $n(\{P^{\mu\nu}\})$ to the density represented on the grid $\tilde{n}(\{P^{\mu\nu}\})$. This includes the mapping from the Gaussian basis to the grid using finite radii, the use of multi-grids, and of grid based methods to compute $\nabla\tilde{n}(r)$. This derivation is presented in [85]. We use the notation $\tilde{n}_i$ to denote a value of $\tilde{n}(r)$ on a particular grid point with coordinates r_i. Truncation to a finite radius of the products $\phi_\mu(r)\phi_\nu(r)$ is equivalent to summing over a subset $\{\mu', \nu'\}$ of $\{\mu, \nu\}$ in the definition

$$\tilde{n}_i = \sum_{\{\mu',\nu'\}} P^{\mu'\nu'} \phi_{\mu'}(r_i)\phi_{\nu'}(r_i). \tag{3.21}$$

The derivative of $E(\{P^{\mu\nu}\}, \tilde{n}(\{P^{\mu\nu}\}))$ will be obtained explicitly using the chain rule as

$$H_{\mu\nu} = \frac{\partial E}{\partial P^{\mu\nu}} + \frac{\partial E}{\partial \tilde{n}_i}\frac{\partial \tilde{n}_i}{\partial P^{\mu\nu}}, \tag{3.22}$$

where summation over repeated indices, such as i, is implicit. We refer to $\partial E/\partial\tilde{n}_i$ as the potential on the grid, and use v_i as an abbreviation.

An example is the Slater exchange energy which we compute as

$$E_x^{\text{slater}} = \sum_j dr\, C\, \tilde{n}_j^{\frac{4}{3}} \tag{3.23}$$

where dr is a volume element, and the corresponding derivative is given as

$$\begin{aligned}\frac{\partial E_x^{\text{slater}}}{\partial \tilde{n}_i}\frac{\partial \tilde{n}_i}{\partial P^{\mu\nu}} &= \sum_j dr\, C\, \frac{4}{3}\tilde{n}_j^{\frac{1}{3}}\delta_{ij}\frac{\partial \tilde{n}_i}{\partial P^{\mu\nu}} \\ &= dr\, v_i \frac{\partial \tilde{n}_i}{\partial P^{\mu\nu}}.\end{aligned} \tag{3.24}$$

The sum in Eq.(3.21) is only over a subset μ', ν'. This amounts to performing the following integration (with respect to r_i)

$$v_i \frac{\partial \tilde{n}_i}{\partial P^{\mu\nu}} dr = v_i \phi_\mu(r_i)\phi_\nu(r_i) dr \tag{3.25}$$

over exactly the same grid points that have been used in the mapping of $\phi_\mu(r)\phi_\nu(r)$.

Only slightly more involved is the case where the density functional depends on the density and on the gradient of the density. The gradient is $g_j = D_j(\{\tilde{n}_i\})$, where the derivative operator D_j can be a function of all grid points, e.g. if the discrete Fourier transform is employed for computing the gradient, or a local function of the

grid for a finite difference approximation $g_j = (\tilde{n}_{j+1} - \tilde{n}_{j-1})/(2\Delta)$. Using the chain rule leads to

$$\frac{\partial E(\tilde{n}_i, g_i)}{\partial P^{\mu\nu}} = \frac{\partial E(\tilde{n}_i, g_i)}{\partial \tilde{n}_i}\frac{\partial \tilde{n}_i}{\partial P^{\mu\nu}} + \frac{\partial E(\tilde{n}_i, g_i)}{\partial g_j}\frac{\partial g_j}{\partial \tilde{n}_i}\frac{\partial \tilde{n}_i}{\partial P^{\mu\nu}} \tag{3.26}$$

$$\frac{\partial E(\tilde{n}_i, g_i)}{\partial P^{\mu\nu}} = \frac{\partial E(\tilde{n}_i, g_i)}{\partial \tilde{n}_i}\frac{\partial \tilde{n}_i}{\partial P^{\mu\nu}} + \frac{\partial E(\tilde{n}_i, g_i)}{\partial g_j}\frac{\partial D_j(\{\tilde{n}_i\})}{\partial \tilde{n}_i}\frac{\partial \tilde{n}_i}{\partial P^{\mu\nu}}, \tag{3.27}$$

valid for all choices of D. Computing $\partial E(\tilde{n}_i, g_i)/\partial g_j$ and $\partial D_j(\{\tilde{n}_i\})/\partial \tilde{n}_i$ is the numerical equivalent of performing a partial integration.

Furthermore, we consider, as an extension of the basic scheme, a multi-grid method in which $\phi_\mu(r)\phi_\nu(r)$ is mapped to a different grid, according to the smoothness of the Gaussian product. The total density needs to be obtained on the finest grid using an operator that performs the interpolation. The value on the fine mesh is obtained as $n_j^f = I_j(\{n_i^c\})$ where the superscripts f and c imply the fine and the coarse mesh respectively, and the interpolating operator I_j might depend on all grid points. Therefore the derivative will involve terms like

$$v_j \frac{\partial I_j(\{n_i^c\})}{\partial n_i^c}\frac{\partial n_i^c}{\partial P^{\mu\nu}}. \tag{3.28}$$

The index j in the above expression runs over all grid points of the fine mesh, whereas the index i goes over the coarse mesh. The term $v_j \partial I_j(\{n_i^c\})/\partial n_i^c$ can be interpreted as constructing the potential on the coarse grid.

Finally, we note that in the particular cases of a Fourier space derivative for D_j and a Fourier interpolation for I_j, it is advantageous to use a g-space representation for all densities and operators involved, as all derivatives such as $\partial D_g(\{\tilde{n}_g\})/\partial \tilde{n}_{g'}$ are diagonal (i.e. $\propto \delta_{gg'}$).

3.3.2 Forces on the ions

The ionic forces can be evaluated by computing explicitly the gradient of the GPW energy as defined by Eq.(3.3) and Eq.(3.11) with respect to the atomic positions. This derivative must take the atom centered nature of the Gaussian basis set and the orthogonality constraints on the wave functions into account. We list the required derivatives in the following. These are computed analytically for all terms except for the Coulomb and exchange and correlation terms that are computed on the grids, consistent with their definition.

The derivatives of the density independent terms are given by

$$\nabla_I E^{\text{ovrl}} = \sum_{J\neq I} \frac{\boldsymbol{R}_J - \boldsymbol{R}_I}{|\boldsymbol{R}_I - \boldsymbol{R}_J|^2}\left\{\frac{Z_I Z_J}{|\boldsymbol{R}_I - \boldsymbol{R}_J|}\text{Erfc}\left[\frac{|\boldsymbol{R}_I - \boldsymbol{R}_J|}{\sqrt{{R_I^c}^2 + {R_J^c}^2}}\right] + \frac{2}{\sqrt{\pi}}\frac{Z_I Z_J}{\sqrt{{R_I^c}^2 + {R_J^c}^2}}\exp\left[-\frac{|\boldsymbol{R}_I - \boldsymbol{R}_J|^2}{{R_I^c}^2 + {R_J^c}^2}\right]\right\}$$

$$\nabla_I E^{\text{self}} = 0$$

All other terms depend directly on the density matrix $P^{\mu\nu}$, but involve only derivatives of Cartesian Gaussian functions, that can easily be computed, since these are again

Cartesian Gaussian functions, but with different l quantum number. In this derivation, we follow closely Ref. [139] and introduce explicitly the derivatives $\nabla_I P^{\mu\nu}$ which are afterwards related to the orthogonality constraints on the wave function. We define E^{core} and $H^{\text{core}}_{\mu\nu}$ as the energy and matrix elements due to the electronic kinetic energy, the short range part of the local pseudo potential, and the non-local pseudo potential

$$\begin{aligned}
\nabla_I E^{\text{core}} &= \sum_{\mu\nu} (\nabla_I P^{\mu\nu}) H^{\text{core}}_{\mu\nu} + \sum_{\mu\nu} P^{\mu\nu} (\nabla_I H^{\text{core}}_{\mu\nu}) \\
&= \sum_{\mu\nu} (\nabla_I P^{\mu\nu}) H^{\text{core}}_{\mu\nu} \\
&\quad + \sum_{\mu\nu} P^{\mu\nu} \big[2\langle \nabla_I \varphi_\mu(\boldsymbol{r})| - \frac{1}{2}\nabla^2 |\varphi_\nu(\boldsymbol{r})\rangle \\
&\quad + 2\langle \nabla_I \varphi_\mu(\boldsymbol{r})| V^{\text{SR}}_{\text{loc}}(r) |\varphi_\nu(\boldsymbol{r})\rangle \\
&\quad + 2\langle \nabla_I \varphi_\mu(\boldsymbol{r})| V^{\text{PP}}_{\text{nl}}(\boldsymbol{r}, \boldsymbol{r'}) |\varphi_\nu(\boldsymbol{r'})\rangle \\
&\quad + \langle \varphi_\mu(\boldsymbol{r})| \nabla_I V^{\text{SR}}_{\text{loc}}(r) |\varphi_\nu(\boldsymbol{r})\rangle \\
&\quad + \langle \varphi_\mu(\boldsymbol{r})| \nabla_I V^{\text{PP}}_{\text{nl}}(\boldsymbol{r}, \boldsymbol{r'}) |\varphi_\nu(\boldsymbol{r'})\rangle \big]
\end{aligned} \tag{3.29}$$

where the number of terms is already reduced by regrouping terms, exploiting symmetry of $P^{\mu\nu}$ and $H^{\text{core}}_{\mu\nu}$. Furthermore, the translational invariance of the first derivatives is exploited for the force calculation in QUICKSTEP using identities such as e.g.

$$\begin{aligned}
\langle \nabla_I \varphi_\mu(\boldsymbol{r})| - \frac{1}{2}\nabla^2 |\varphi_\nu(\boldsymbol{r})\rangle &= -\langle \varphi_\mu(\boldsymbol{r})| - \frac{1}{2}\nabla^2 |\nabla_J \varphi_\nu(\boldsymbol{r})\rangle \\
\langle \nabla_I \varphi_\mu(\boldsymbol{r})| V(\boldsymbol{r}) |\varphi_\nu(\boldsymbol{r})\rangle + \langle \varphi_\mu(\boldsymbol{r})| V(\boldsymbol{r}) |\nabla_J \varphi_\nu(\boldsymbol{r})\rangle &= -\langle \varphi_\mu(\boldsymbol{r})| \nabla_K V(\boldsymbol{r}) |\varphi_\nu(\boldsymbol{r})\rangle
\end{aligned}$$

where $\varphi_\mu(\boldsymbol{r})$, $\varphi_\nu(\boldsymbol{r})$ and $V(\boldsymbol{r})$ are located on the atoms I, J and K respectively.

The density dependent energy terms are computed using the chain rule with the density as an intermediate variable to yield the following derivatives

$$\begin{aligned}
\nabla_I E^{\text{H}}[n_{\text{tot}}] + \nabla_I E^{\text{xc}}[n] &= \sum_{\mu\nu} (\nabla_I P^{\mu\nu}) V^{\text{tot}}_{\mu\nu} \\
&\quad + 2\sum_{\mu\nu} P^{\mu\nu} \int (\nabla_I \varphi_\mu(\boldsymbol{r})) v^{\text{tot}}(\boldsymbol{r}) \varphi_\nu(\boldsymbol{r}) d\boldsymbol{r} \\
&\quad + \int (\nabla_I n^I_{\text{c}}(\boldsymbol{r})) v^{\text{H}}(\boldsymbol{r})\, d\boldsymbol{r}
\end{aligned} \tag{3.30}$$

where $v^{\text{tot}}(\boldsymbol{r}) = v^{\text{H}}(\boldsymbol{r}) + v^{\text{xc}}(\boldsymbol{r})$.

In the above equations, the terms involving $\nabla_I P^{\mu\nu}$ can be collected and rewritten using the Kohn-Sham matrix $K_{\mu\nu}$ as

$$\sum_{\mu\nu} (\nabla_I P^{\mu\nu}) \left(H^{\text{core}}_{\mu\nu} + V^{\text{tot}}_{\mu\nu}\right) = \sum_{\mu\nu} (\nabla_I P^{\mu\nu})\, K_{\mu\nu} \tag{3.31}$$

The derivative of the density matrix can be eliminated by expanding the density matrix in terms of the wave function coefficients, inserting the Kohn-Sham equations

(Eq.(3.32)), and simplifying the expression using the derivative of the orthogonality constraints on the wave functions (Eq.(3.33)).

$$\sum_{\nu} K_{\mu\nu} c_i^{\nu} = \varepsilon_i \sum_{\nu} S_{\mu\nu} c_i^{\nu} \tag{3.32}$$

$$\begin{aligned} \nabla_I \sum_{\mu\nu} c_i^{\mu} S_{\mu\nu} c_i^{\nu} &= 0 \\ 2 \sum_{\mu\nu} (\nabla_I c_i^{\mu}) S_{\mu\nu} c_i^{\nu} &= - \sum_{\mu\nu} c_i^{\mu} (\nabla_I S_{\mu\nu}) c_i^{\nu} \end{aligned} \tag{3.33}$$

This leads to

$$\begin{aligned} \sum_{\mu\nu} (\nabla_I P^{\mu\nu})\, K_{\mu\nu} &= \sum_{\mu\nu} \sum_{i}^{\text{occ}} \left[(\nabla_I c_i^{\mu}) K_{\mu\nu} c_i^{\nu} + c_i^{\mu} K_{\mu\nu} (\nabla_I c_i^{\nu}) \right] \\ &= 2 \sum_{\mu\nu} \sum_{i}^{\text{occ}} \varepsilon_i (\nabla_I c_i^{\mu}) S_{\mu\nu} c_i^{\nu} \\ &= - \sum_{\mu\nu} \sum_{i}^{\text{occ}} \varepsilon_i c_i^{\mu} c_i^{\nu} (\nabla_I S_{\mu\nu}) \\ &= - \sum_{\mu\nu} W^{\mu\nu} (\nabla_I S_{\mu\nu}) \\ &= -2 \sum_{\mu\nu} W^{\mu\nu} \langle \nabla_I \varphi_{\mu}(\boldsymbol{r}) | \varphi_{\nu}(\boldsymbol{r}) \rangle \end{aligned} \tag{3.34}$$

where the energy weighted density matrix $W^{\mu\nu}$ is introduced. It can be observed that this force contribution is easily calculated as it only involves derivatives of overlap matrix elements. This term was originally derived by Pulay [139] and is only present if the basis set depends on the atomic positions. For complete basis sets this term vanishes.

3.4 Basis sets

The Kohn-Sham orbitals are expanded in Gaussian orbital functions in the framework of the GPW method as described in Sec.(3.2). Significant experience exists with Gaussian basis sets and they are available in a number of formats [140, 141]. Whereas polarization and diffuse functions can normally be adopted from published basis sets, the valence part of the basis has to be generated for the usage with the GTH pseudo potentials. A systematically improving sequence of basis sets for use with the GTH pseudo potentials was optimized for all first- and second-row elements, using the procedure detailed below.

Exponents of a set of primitive Gaussian functions were optimized to yield the lowest pseudo atom energies for all first- and second-row elements with an atomic DFT code employing the appropriate GTH potential for each element. The atomic DFT code allows for the calculation of first analytic derivatives of the total atomic energy with respect to the Gaussian orbital exponents. A family basis set scheme was adopted using the same set of exponents for each angular momentum quantum number of the occupied valence states, i.e. s and p orbitals for the elements from H to Ar. A growing

number of primitive Gaussian functions, typically four to six, was included into these sets to provide an increasingly good description of the pseudo atomic wave function. Finally, these primitive Gaussian functions were contracted using the coefficients of the respective pseudo atomic wave functions. In addition, a split valence scheme was applied to enhance the flexibility of the valence basis part. The splitting was increased in line with the number of primitive Gaussian functions employed from double- (DZV) over triple- (TZV) up to quadruple-zeta valence (QZV). For instance, the basis set sequence for oxygen starts with four primitive Gaussian functions on the DZV level, uses five functions for TZV, and finally six on the QZV level. Moreover, these basis sets were augmented by polarization functions which were taken from the all-electron basis sets cc-pVXZ (X = D, T, Q) of Dunning [116, 142], but only the first p or d set of polarization functions was used depending on the actual element. In that way a new sequence of basis sets was created with an increasing number of primitive Gaussian functions and polarization functions for each first- and second-row element. The basis sets were labeled DZVP, TZVP, TZV2P, QZV2P, and QZV3P due the applied degree of splitting and the increasing number of provided polarization functions. If required, these basis sets can be further augmented by diffuse functions, analogous to the aug-cc-pVXZ basis sets, resulting in a sequence aug-DZVP, aug-TZVP, aug-TZV2P, aug-QZV2P, and aug-QZV3P. The inclusion of diffuse functions may significantly improve the accuracy of certain molecular properties, especially in the gas phase, but require treatment for the near linear dependencies that typically arise in condensed phase calculations.

3.5 Conclusions

In this chapter, we have described the current implementation of the GPW method in the QUICKSTEP program. A number of novel computational techniques make the computational cost of increasing the basis set size rather modest, effectively growing linearly with basis set size. At present, without controversy, QUICKSTEP algorithm can be considered the state of the art in molecular simulation programs.

Chapter 4

Molecular Mechanics: Overview

In this chapter we provide a general insight into the main potential energy functions used in Molecular Mechanics (MM) methods, relevant for QM/MM applications.

4.1 Introduction

The modeling of the properties of molecules using appropriate potential functions is called molecular mechanics (MM). This name reflects the fact that a molecular force field considers a molecule as a collection of balls connected by springs and that examination of the mechanical properties of such a system is similar to the study of the properties of the corresponding molecule. The aim of MM techniques is to perform computer simulations, or to do chemical experiments with a computer rather than a laboratory bench. Though the results of such simulations have to be validated by experiment, it is known that in many cases you may rely on them as much as on the true experimental values.

The MM approach includes several techniques that are aimed at determining different molecular properties. In particular, with a given set of analytical potential functions one can evaluate the molecular equilibrium geometries and the vibrations around these configurations. The task can be accomplished in the simplest way using the Cartesian representation. That is, the potential surface for a molecule with N atoms can be expanded formally around the equilibrium configuration $\vec{\mathbf{R}}_0$ and give

$$V(\vec{\mathbf{R}}_0 + \delta\vec{\mathbf{R}}) = V(\vec{\mathbf{R}}_0) + \sum_{i\alpha}\left(\frac{\partial V}{\partial R_{i\alpha}}\right)\delta R_{i\alpha} + \sum_{i\alpha,j\beta}\left(\frac{\partial^2 V}{\partial R_{i\alpha}\partial R_{j\beta}}\right)\delta R_{i\alpha}\delta R_{j\beta} + \ldots \tag{4.1}$$

where the indices i and j indicate atoms while α and β run over the x, y, z and coordinates of each atom. The first term is just the energy of the molecule at the equilibrium geometry. The second and third terms can be used to evaluate the equilibrium geometry and the vibrational frequencies.

4.2 Potential Functions (Force field)

It is well known from structural chemistry and from quantum calculations that bond lengths and valence angles in typical units and groups are very similar even if they appear in different molecules. The single bond between two sp^3 hybridized carbon atoms is around 1.5 Å long and the valence angle for an sp^3 carbon is usually close to 109°. On the other hand, these values are frequently distorted in some strained ring systems (like cyclopropane) or crowded molecules (like tetramethylmethane). The concept of molecular strain can be rationalized considering bonds as elastic springs whose distortion is reflected by a positive increment (i.e., thermodynamically unfavorable) to the potential energy of the molecule. These approaches were originally called *empirical potential energy functions* but the term *molecular mechanics* is now in common use. The mathematical form of this potential energy function (also called potential energy surface) is:

$$V(\vec{\mathbf{R}}_1, \ldots, \vec{\mathbf{R}}_N) = \sum_{i=1}^{k} V^i(\vec{\mathbf{R}}_1, \ldots, \vec{\mathbf{R}}_N) \tag{4.2}$$

where V represents the potential energy of the molecular system and depends upon the Cartesian coordinates of all atoms denoted here as $\{\vec{\mathbf{R}}_1, \ldots, \vec{\mathbf{R}}_N\}$. V^i are individual energy terms representing contributions from individual interactions which depend upon the Cartesian coordinates of atoms. Having V one can calculate the potential energy of the molecular system as well as the forces acting on atoms and groups. Individual energy terms, V^i, are functions of coordinates (usually internal coordinates) and parameters, i.e., constants, called *force field parameters*. The set of such parameters and the functional form of the potential is called a force field. In a good force field, parameters are well balanced and produce consistent results. There are many different force fields which differ substantially in the values of corresponding parameters and in the functional form of the energy terms. The functional forms and parameters of molecular force fields are usually estimated from studies of small molecules with the implicit assumption that these functions are transferable from small to large molecules. Individual potential terms V^i are conventionally grouped into two classes:

Bonded terms describe contributions from atoms which are covalently bound. They include bond stretching, angle bending, out-of-plane distortions, and torsional terms. Some force fields include cross-terms, e.g., stretch-stretch, stretch-bend, etc.

Non-bonded terms represent contributions to potential energy coming from interactions between atoms which are not covalently bound, i.e., Van der Waals interactions, electrostatic interactions and hydrogen bonds.

See Ref.[143] for an excellent monograph on MM topics and on implementational issues.

4.2.1 Bonded Potentials

Stretching Potential

The bond stretching term, V_{ij}^{bond} , for a covalent bond between atoms i and j, represents a contribution to the potential energy resulting from deformation of the optimal bond

length. Most frequently a simple symmetric parabola (i.e., harmonic approximation) is used:

$$V_{ij}^{bond} = \frac{1}{2} K_{ij}^{bond} (d_{ij} - d_{ij}^{0})^2 \tag{4.3}$$

where K_{ij}^{bond} is a bond stretching parameter (frequently called a bond stretching force constant) and its value represents the stiffness of the bond (i.e., the ease with which the bond can be distorted). Large values of K_{ij}^{bond} correspond to "hard" bonds and small values to "soft" bonds. The value of d_{ij}^{0} corresponds to the optimal (i.e., unstrained) bond length. Contribution from this term is never negative and is equal to zero only when the actual bond length, d_{ij} , is exactly equal to the optimal bond length . The actual bond length d_{ij} is calculated from the Cartesian coordinates of atoms i and j. For accurate calculations more elaborate expressions for the bond stretching term are used, e.g., a Morse potential, which takes into account the fact that the potential for bond deformation is not symmetric and it is easier to stretch the bond than to squeeze it.

Bending Potential

The form of the angle bending term is very similar. In most cases the contribution to potential energy, V_{ijk}^{angle}, is represented by a harmonic expression depending upon the bending force constant, K_{ijk}^{angle}, the actual value of the valence angle θ_{ijk} and its "natural", optimal value, θ_{ijk}^{0}

$$V_{ijk}^{angle} = \frac{1}{2} K_{ijk}^{angle} (\theta_{ijk} - \theta_{ijk}^{0})^2 \tag{4.4}$$

The out-of-plane term is used to account for the energy contribution from distorting an aromatic or conjugated system of bonds from planarity and is most frequently a harmonic term:

$$V_{\chi}^{angle} = \frac{1}{2} K_{\chi}^{angle} \chi^2 \tag{4.5}$$

where in the case of sp^2 hybridized carbon, χ is an angle between one of the bonds originating at the central atom and a plane passing through the other two bonds.

Torsional Potential

The functional form of the torsional depends, in most cases, on the cosine of the product of a torsional angle and the periodicity

$$V_{ijkl}^{torsion} = \frac{1}{2} V_n [1 + s \cos(n\theta_{ijkl})] \tag{4.6}$$

where V_n is the height of the torsional barrier; s is -1 if a minimum occurs for the eclipsed conformation and +1 if a minimum corresponds to the staggered conformation; n is a periodicity, i.e., the number of maxima per full revolution; and θ_{ijkl}

is a torsional angle.For the torsional angle involving C–C bond in ethane, s=1 and n=3, while for the double bond in ethylene s=-1 and n=2. More elaborate force fields use as a torsional term the sum of several cosine functions with different periodicities to account for smaller "humps" appearing on the torsional energy dependence. On occasion, the harmonic potential is used for torsional angles around double bonds due to their stiffness.

4.2.2 Non-bonded Potentials

Non-bonded terms describe contributions brought by the interaction of atoms which are not covalently bonded. Atoms which are two bonds apart (1-3 interactions), are usually not included in the non-bonded interaction list, since it is assumed that their interaction is satisfactorily accounted for by the angle bending term. However, non-bonded interactions of atoms separated by 3 covalent bonds in the molecular graph (1-4 interactions) are routinely included in spite of the fact that they appear in the torsional term. Generally, the non-bonded interactions represent contributions to energy from Van der Waals interactions, electrostatic interactions and they frequently account explicitly for hydrogen bonds.

The non-bonded terms are usually represented mathematically as two-body interactions. They depend on the coordinates of only two interacting atoms, i.e., are represented as pairwise potentials. This is an approximation, and it is well known that the interaction between two atoms depends significantly upon the positions of other atoms, especially those at close proximity. However, even for pairwise potentials, calculation of non-bonded terms is at present a significant computational effort since it is approximately proportional to the square in number of atoms. For three-body potentials (i.e., functions which depend on positions of three non-bonded atoms), the computational effort would be proportional to the cube of the number of atoms and this is unmanageable for large molecules. For that reason, the three-body potentials are not routinely used. The quadratic scaling of two body potentials can be in some cases reduced up to linear scaling by omitting the interactions of distant atoms (i.e., skipping calculation of the non-bonded term for atoms which are further apart than some predetermined cut off distance). However, checking if atoms are outside the cut off distance is also a substantial computational effort for larger molecules, and it is considered to represent the most computationally expensive part of MM codes.

Van der Waals terms

The Van der Waals interaction energy, V^{vdW}, is represented by the sum of two terms, a repulsive term ($V^{overlap}$) and an attractive term ($V^{dispersion}$):

$$V^{vdW} = V^{overlap} - V^{dispersion} \tag{4.7}$$

The repulsive term, $V^{overlap}$, rapidly grows at close inter-atomic distances due to the overlapping of the electron clouds of the two atoms which results in the disruption of their electronic structure. This gives rise to a strong repulsion . At moderate distances between atoms, i.e., larger than the sum of their Van der Waals radii, the dispersion term, $V^{dispersion}$ dominates. These attractive forces were first identified by London in 1930, and exist even when molecules have no permanent charge or dipole moment. The dispersion energy is of quantum mechanical origin and cannot

be described in classical terms. The electrons in an atom are in continuous motion and the electron distribution around the nucleus is constantly fluctuating giving rise to instantaneous dipole moments. Though on the average the dipole moment of an atom is zero, at any given moment there is some temporary dipole moment present which by induction produces a dipole moment of opposing direction in the neighboring atom. The attraction of these instantaneous dipoles results in a dispersion energy. The simplest and most widely used equation approximating this behavior is due to Lennard-Jones [144]. For two atoms i and j as a function of their distance r_{ij}:

$$V_{ij}^{vdW} = \frac{n\epsilon_{ij}}{n-m}\left[\frac{m}{n}\left(\frac{r_{ij}}{\sigma_{ij}}\right)^{-n} - \left(\frac{r_{ij}}{\sigma_{ij}}\right)^{-m}\right] \tag{4.8}$$

where ϵ_{ij} is the depth of a well (i.e., the maximal attraction energy), n and m are exponents (typically n=12 or 9, and m=6), and σ_{ij} is the distance between atoms which corresponds to a minimum.

BKS potential

Among the numerous number of pair potential types developed to describe the most desperate systems we want to focus our attention on the one that successfully describes the behavior of silicon dioxide in the glass phase, relevant for the discussion in the next chapters (see Chap.(7), Chap.(8) and Chap.(9)). Among the most widely used, is the so-called BKS potential developed by van Beest, Kramer, van Santen (BKS) [41]. We choose to use the BKS potential, as it allows for faster simulation than the other available three-body [145, 146] potentials while leading to similar results; the three body information necessary to create the tetrahedra network in silicon dioxide is not lost with the BKS potential, but is implicitly present by the choice of the po- tential parameters derived from the cluster model of van Beest et al. [41]. The BKS potential is a two-body potential based on the Buckingham potential with an added Coulombic term. It describes the interaction between two atoms i and j with an interatomic distance r_{ij} through the functional form:

$$V_{MM} = \sum_{ij}\left(\frac{q_i q_j}{r_{ij}} + V_{ij}\right) \tag{4.9}$$

$$V_{ij} = A_{ij}e^{-b_{ij}r_{ij}} - \frac{C_{ij}}{r_{ij}^6}, \tag{4.10}$$

The parameters for the short range interaction A,b,C are given in Ref.[41].

Electrostatic terms

The electrostatic interaction energy, V^{elec}, between two non-bonded atoms i and j is usually represented by Coulomb's law:

$$V_{ij}^{elec} = \frac{q_i q_j}{\epsilon r_{ij}} \tag{4.11}$$

where q_i and q_j are the net atomic charges of atom i and j, respectively, r_{ij} is the inter-atomic distance, and ϵ is the dielectric constant of the medium between the

interacting charges. The dielectric constant, ϵ, is a well defined quantity only for macroscopic systems. At the molecular level, a common approximation is to use its value for a vacuum (i.e., ϵ=1). To take into account the presence of other atoms in the molecule or to incorporate the influence of the solvent, implicit solvent models [147, 148, 149] have been developed, in which the polarization effects due to the presence of the solvent is approximated using different values for ϵ and solving the Poisson equation for the system.

The major ambiguity in the Coulomb potential is the concept of atomic charge itself. The atom is made up of a nucleus and electrons orbiting around it, and its charge is zero by definition. However, in the molecule, averaged electron trajectories are no longer centrosymmetric around nuclei, due to the formation of chemical bonds between atoms, and the resulting average electron density can be a very complex function in three dimensions. Electrons are on average closer to more electro-negative atoms and farther from atoms with low electro-negativity. The net effect of this unequal electron distribution can be approximated by placing a number of point charges in such a way that they reproduce the electrostatics of the molecule with reasonable accuracy. Usually, these charges are placed at the positions of atomic nuclei and are called net atomic charges.

There are several ways of deriving atomic charges depending on which molecular property is chosen to be represented best. In many popular force fields they are chosen to reproduce known experimental data, e.g.: dipole moments, geometries, vibrational spectra, etc. They are frequently derived theoretically from a variety of electro-negativity equalization schemes and quantum calculations at different levels of sophistication. In the case of quantum chemical calculations, the charges may be derived either from population analysis [150, 151, 152, 153, 154, 155] or fitted by least squares [156, 157, 158, 159] to the electrostatic potential. The charges derived from *ab initio* electrostatic potential are considered superior but this method is also the most computationally demanding.

Hydrogen bonds

The effect of hydrogen bonding is incorporated into the potential energy surface of a molecular system in a variety of ways. In general, hydrogen bonds are formed between hydrogen donor and hydrogen acceptor groups: –D–H...A–AA–. The simplest approach, which at the same time performs very well, is to assume that the proton does not contribute to the Van der Waals energy. In this model [160], the proton and the acceptor atom attract each another since they possess opposing net charges. This results in the stretching of the D–H bond and driving atom A towards the hydrogen. Balance is achieved by contributions from the D–H stretching term, and electrostatic and Van der Waals repulsions of atoms D and A. This approach does not impose any directionality on the hydrogen bonds but the balance of all of these forces usually yields a geometry close to linear (i.e., when atoms D, H, A and AA lie on the straight line). Some more elaborate models explicitly use powers of $\cos(\theta_{D-H...A})$ and $\cos(\theta_{H...A-AA})$ to enforce the linearity of the observed hydrogen bond geometry and incorporate the 12-10 Lennard-Jones potential for the distance between H and A [77].

4.3 Molecular Dynamics

Molecular Dynamics (MD) simulations evaluate the motion of the atoms in a given system and provide the positions or trajectory of these atoms as a function of time.

The trajectories are calculated by solving the classical equation of motion for the molecule under consideration. This alike to the well known approach in which one evaluates the speed and position of a bullet starting from the initial velocity, the mass and the forces by using Newton's equation of motion. In the case of molecules, one obtains the relevant forces on each atom from the first derivatives of the given potential functions. The actual evaluation of classical trajectories is done numerically, expressing the changes in coordinates and velocities at a time increment, Δt, by

$$\vec{\mathbf{R}}_i(t+\Delta t) = \vec{\mathbf{R}}_i(t) + \dot{\mathbf{R}}_i(t)\Delta t \tag{4.12}$$

$$\dot{\mathbf{R}}_i(t+\Delta t) = \dot{\mathbf{R}}_i(t) + \ddot{\mathbf{R}}_i(t)\Delta t \tag{4.13}$$

Using the Newton's law:

$$M_i\vec{\mathbf{R}}_i = \vec{F}_i = -\frac{\partial V}{\partial \vec{\mathbf{R}}_i} \tag{4.14}$$

and starting with a given set of initial conditions (e.g. with the values of $\vec{\mathbf{R}}_i(t=0)$ and $\dot{\mathbf{R}}_i(t=0)$) you can evaluate the trajectory of the system. Advanced several numerical schemes can be used for integrating numerically Newton equation of motions, for instance the Verlet Algorithm [161].

The strength of MD approaches is associated with the fact that they have the ability to simulate, at least in principle, the true microscopic behaviors of macromolecules. The weakness is associated with the fact that some properties reflect extremely long time processes which cannot be simulated by any current computer.

The emergence of MD simulations in studies of biological systems can be traced to a simulation of the dynamics of the primary event in the visual process [162] that correctly predicted a photoisomerization process of around 100 femtoseconds. A subsequent study [163] attempted to examine the heat capacity of BPTI by a very short simulation of this protein in vacuum. However, at the early stages of the development of this field, it was not possible to obtain meaningful results for average properties of macromolecules due to the need for much stronger computers to reach a reasonable convergence (the heat capacity was drastically underestimated in Ref. [164], reflecting artificial relaxation motions). Nevertheless, ultrafast reactions such as those that control the photo-biological process could be simulated even at this early stage [162].

Eventually with the increase of computer power it has become feasible to reach simulation times of microseconds and to start to obtain meaningful average properties of macromolecules.

Part III

Theoretical QM/MM Methods

Chapter 5

Regularization of the electrostatic coupling

In this chapter the problem of defining a regularized and renormalized electrostatic coupling Hamiltonian for hybrid QM/MM calculations is addressed. For honesty sake we specify that the choice of the functional form used for the electrostatic coupling Sec.(6.3) was originally driven by empirical considerations and only later, in 2005, a theoretical justification was proposed [80].

5.1 Introduction

The development of an appropriate coupling Hamiltonian between the two subsystems is the biggest challenge in such hybrid methods [2, 57, 63]. The manner in which bonded interactions between MM and QM atoms are treated was already discussed in Chap.(2.3). On the other hand, the electrostatic part of nonbonded interactions face a different challenge. The point-like description of the MM-atom charges and their interactions with the QM electrons at short ranges can cause an artificial and non physical polarization of the QM electron density [2, 57, 165]. Such an artificial polarization can influence the outcome of a chemical reaction study, the dipole moment, and other properties based on electronic charge density [2, 57, 165].

As it stands, the point charges are meant to reproduce the electrostatic potential between atoms in a molecule where the atom-atom separation is of the order of an angstrom or above. However, for the QM/MM Hamiltonian, the separation between a point charge and QM electrons can take any value from zero to the size of the system. Obviously, the point-charge description for the MM atom cannot provide a compatible picture for the QM/MM Coulomb interaction at distances close to zero and this can be a source of non physical polarization of QM electrons and divergent forces on the MM atoms. To remove this divergence, arising from a point-like charge description of the MM atom, an empirical description of a renormalized Coulomb potential was introduced [2, 165]. Recently [80] a theoretical derivation based on a localized partial-wave expansion of the MM charge was proposed, adjusting the extension of the charge distribution in order to normalize the Coulomb potential near interatomic separations of the order of twice the covalent radius. Exploiting the s-wave expansion of the point charge, the scheme leads naturally to large scale cancellations in the Coulomb potential. At short distances, the potential intrinsically reduces to a value of $1/\mathrm{r}_c$ (r_c = covalent radius) thus avoiding non physical localization of QM electrons on a positively charged MM atom, in full agreement with the original semi-empirical hint.

5.2 QM/MM Hamiltonian

The central issue of a QM/MM hybridization scheme is the definition of the QM/MM coupling part $\mathcal{H}_{QM/MM}$ [57, 10, 166, 63]. $\mathcal{H}_{QM/MM}$ accounts for the interaction between the quantum system and the MM atoms. In general, $\mathcal{H}_{QM/MM}$ contains Coulomb (long-range) and short-range interactions (Van der Waals attraction and short-range repulsion) and is taken as [57, 10, 166, 63]

$$\mathcal{H}_{QM/MM} = \sum_{a\in MM}\int d\mathbf{r}\frac{\rho_e(\mathbf{r},\mathbf{r}_\alpha)q_a}{\mathbf{r}-\mathbf{r}_a} + \sum_{a\in MM}\sum_{\alpha\in QM}\frac{Z_\alpha q_a}{|\mathbf{r}_\alpha-\mathbf{r}_a|} + \sum_{a\in MM}\sum_{\alpha\in QM} 4\epsilon_{\alpha,a}\left\{\left(\frac{\sigma_{\alpha,a}}{|\mathbf{r}_\alpha-\mathbf{r}_a|}\right)^{12} - \left(\frac{\sigma_{\alpha,a}}{|\mathbf{r}_\alpha-\mathbf{r}_a|}\right)^{6}\right\} \tag{5.1}$$

where $\mathbf{r}$, $\mathbf{r}_\alpha$ and $\mathbf{r}_a$ represent the position vector for electrons, QM nuclei with charge Z_α and MM nuclei with atom partial charge q_a, respectively. ρ_e represents the electron density. The short-range repulsion and attractive mutual average polarization (Van der Waals) between QM and MM atoms are modeled using the Lennard-Jones (LJ) potential [167]; σ and ϵ are parameters defining the LJ potential.

If an interaction Hamiltonian like Eq.(5.1) is used, artifacts may arise due to the presence of unscreened Coulomb charges of the MM atoms. This effect is ultimately due to the absence of Pauli exclusion repulsion for the QM electrons by the MM atoms. The atom included in the MM subsystem should exert Pauli repulsion due to its own electrons (which are replaced together with the nuclear charge by an effective point charge) and would deter the QM electrons to penetrate the atom valence shell. In a purely classical force field calculation, the $\frac{1}{|\mathbf{r}_\alpha-\mathbf{r}_a|}$ term of the Lennard-Jones potential [167] take into account this effect and provides sufficient repulsion between atoms at short range, thus keeping the attractively interacting MM atoms at appropriate separations. For QM theories, the Pauli exclusion repulsion is incorporated either properly antisymmetrizing the electronic wave function or by employing an exclusion hole concept (for methods with DFT origin). Nevertheless, incorporating the Pauli exclusion repulsion between the QM electronic charge distribution and the MM point charges in a hybrid QM/MM calculation remains a formidable challenge. One idea is to seek a comprehensive description of the QM/MM Coulomb interaction considering a localized expansion of the charges which regularizes the potential at short range while reduces to the Coulomb potential for larger distances ($\mathbf{r} >> 2\mathrm{r}_c$). As the charge reflects the overall electrostatic potential acting at a point in the configuration space, it accounts for the Pauli exclusion effect too. However, this conjecture is valid only beyond a certain radius and not at short distances where the notion of point charge looses its validity. Thus it is customary to regularize the potential at these short distances without affecting its value for distances grater than r_c.

Earlier Eichinger *et al.*[35] and recently Das *et al.*[165] proposed to replace the MM point charge with a Gaussian delocalized charge density to remedy the short-range artifact. They used a multistep approach to evaluate the Coulomb interaction between an MM atom and the quantum system. The Coulomb part of their hybrid QM/MM Hamiltonian is given by

$$\mathcal{H}_{\rho_e,q_a} = \int d^3r\rho_e(\mathbf{r},\mathbf{r}_\alpha)q_a\frac{\mathrm{Erf}(|\mathbf{r}-\mathbf{r}_a|/\sigma)}{|\mathbf{r}-\mathbf{r}_a|} \tag{5.2}$$

Here $\rho_e(\mathbf{r}, \mathbf{r}_\alpha)$ is the electronic charge density, Erf is the error function, $\mathbf{r}_a$ is the position of the a^{th} MM atom and the value of σ is the same for all atoms (0.8Å). As the error function (which integrates the Gaussian distribution over a certain radius) asymptotically reaches the value of unity, the above function has the correct asymptotic behavior of the Coulomb interaction at large distance. At short distances, the error function is less than unity and it tends to zero as distance goes to zero, thus removing the discontinuity in the QM/MM interaction potential. We compare the functional behavior of this form of the potential vis-a-vis the pure Coulomb interaction in Fig.(5.1). It appears that the potential does not saturate near twice the covalent radius of the atom, which is supposed to be a key issue in the modeling of the Coulomb QM/MM interaction. Afterwards, Laio *et al.*[2] introduced another

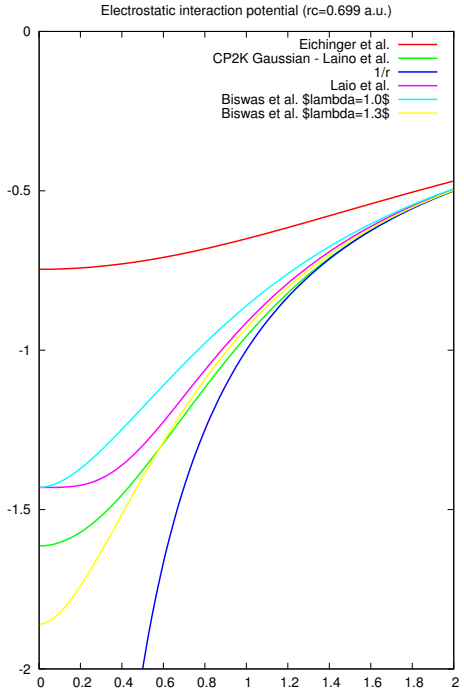

Figure 5.1: Electrostatic interaction potential between an electron (a.u.) and a unite positive charge. The r_c value is equal to 0.699 a.u..

functional form that takes into account the short range effect with the Coulomb potential saturating near the covalent radius of the MM atom. The Coulomb part of their hybrid QM/MM Hamiltonian is given by

$$\mathcal{H}_{\rho_e, q_a} = \int d^3 r \rho_e(\mathbf{r}, \mathbf{r}_\alpha) q_a \frac{r_{c,a}^n - \tilde{\mathbf{r}}^n}{r_{c,a}^{n+1} - \tilde{\mathbf{r}}^{n+1}} \tag{5.3}$$

where $\tilde{\mathbf{r}} \equiv |\mathbf{r} - \mathbf{r}_a|$. In the above prescription, the usual Coulomb interaction of $\frac{1}{\tilde{\mathbf{r}}}$ is being replaced by $v(\tilde{\mathbf{r}}) = \frac{r_{c,a}^n - \tilde{\mathbf{r}}^n}{r_{c,a}^(n+1) - \tilde{\mathbf{r}}^(n+1)}$. This functional form also has the correct

asymptotic behavior of $\frac{1}{\tilde{\mathbf{r}}}$ and as $\tilde{\mathbf{r}} \to 0$, it smoothly converges to $\frac{1}{r_{c,a}}$. In Fig.(5.1) we show the behavior of the potential $\mathrm{v}(\tilde{\mathbf{r}})$ for $r_{c,a} = 0.699 a.u.$ (0.37 Å). This corresponds to the electrostatic potential of a QM electron with a unit positive charge. The functional form, although appears very useful for QM/MM electrostatic interactions, has not been derived theoretically and thus may be considered as empirical. The functional forms of Eichinger *et al.*[35] and Laio *et al.*[2] mentioned above reduce both the attractive and repulsive Coulomb interactions at short distances while having the correct asymptotic behavior. Another crucial aspect of these prescriptions is that they lead to zero forces (finite potential) at very short ranges, thus avoiding the artificial localization of the electronic charge density on a positive MM point charge. Laio *et al.*[2] also remarked that they were not successful in finding a functional form that provides repulsion at short distances and could mimic the Pauli exclusion between electronic charge density and the MM point charge.

The problem has been finally solved by Biswas *et al.*[80] who obtained a regularized and renormalized description for the QM/MM electrostatic interaction by arguing that the point like description of the charge must be valid at interatomic separation but at short distance the Coulomb potential must be given by a localized charge distribution. To seek a comprehensive model for the QM/MM Coulomb interaction that could account for the short-range effect, we first consider a localized wave function $\phi(\mathbf{r}-\mathbf{r}_a)$ for the charge present at $\mathbf{r}_a$ so that the normalization of the wave function provides the charge q_a,

$$\int |\phi(\mathbf{r}-\mathbf{r}_a)|^2 d^3r = q_a \tag{5.4}$$

where $\mathbf{r}$ is an arbitrary point in space. For ϕ, a good representation is a partial-wave expansion in terms of an orthonormal basis set $\phi_{lm} = \mathcal{R}_l(u)Y_{lm}(\hat{u})$ of a hydrogen-like wave function and take

$$\phi(\mathbf{u}) = \left(\frac{q_a}{\sum_l |C_l|^2}\right)^{1/2} \cdot \sum_{lm} C_l \mathcal{R}_l(u) Y_{lm}(\hat{u}) \tag{5.5}$$

where $\mathcal{R}_l(u)$ is similar to the radial part of the hydrogen-like wave function and $Y_{lm}(\hat{u})$, the spherical harmonics, represent the angular part; C_l is the expansion coefficient. Similar partial-wave expansion to construct a wave function is frequently used in atomic molecular physics [168]. The next approximation is to adopt a first-order approximation (l=0) to the expansion scheme which would allow to account for the delocalized effect of the charge in the s-wave approximation

$$\phi(\mathbf{r}-\mathbf{r}_a) = \left(\frac{q_a \xi^3}{\pi}\right)^{1/2} \exp^{-\xi|\mathbf{r}-\mathbf{r}_a|} \tag{5.6}$$

The Slater function (see Eq.(5.6)) provides a consistent picture with the localized description of a charge and also enables us to arrive at analytical forms for the potential and force as shown below for the s wave. A similar expansion scheme, but using Gaussian orbitals, has been employed earlier by Das *et al.*[165] to study QM/MM systems. Although both the Gaussian and Slater orbitals are known to provide competitive results, the Slater orbitals have the proper behavior (cusp) at the origin while

the Gaussian orbitals are generally easier to deal with computationally. However, the analytical form for the Coulomb potential using Slater orbitals provides the same computational advantage as Gaussian orbitals. The parameter ξ of the Slater orbital has the dimension of an inverse length and it is *natural* associate it to the reciprocal of the covalent radius $r_{c,a}$: $\xi \approx \frac{1}{r_{c,a}}$. More generally the parameter ξ can be represented as $\xi = \lambda / r_{c,a}$, where the λ parameter will be used to renormalize the Coulomb energy at $2r_{c,a}$ (the interatomic separation). λ controls the spread of the wave function, and for $\lambda >> 1$ the charge distribution collapses to a point like charge.

With the above wave-function description for the charge, we now write the Coulomb interaction potential (static potential) between the a^{th} MM atom and the QM system as

$$\mathcal{H}_{\rho_e,q_a} = \int d^3r \int d^3r' \frac{\rho_e(\mathbf{r},\mathbf{r}_\alpha)|\phi(\mathbf{r}'-\mathbf{r}_a)|^2}{|\mathbf{r}'-\mathbf{r}|} \tag{5.7}$$

$$\mathcal{H}_{\rho_N,q_a} = \int d^3r \int d^3r' \frac{\rho_N(\mathbf{r}_\alpha)|\phi(\mathbf{r}'-\mathbf{r}_a)|^2}{|\mathbf{r}'-\mathbf{r}|} \tag{5.8}$$

where $\mathcal{H}^{Coul}_{QM/MM} = \mathcal{H}_{\rho_e,q_a} + \mathcal{H}_{\rho_N,q_a}$; ρ_N is the charge distribution of the ionic core of the α^{th} QM atom (i.e. sum of the nuclear and inner electron charges). In CP2K the ionic cores are distributed over the grid used also for the electronic charge density. This manner of distributing ionic core charges would not lead to any appreciable modification to the Coulomb energy as the separation between the QM nuclei and the MM atoms becomes of the order of interatomic separation in a molecule and thus would be quite compatible with the point-charge description. Thus, focusing on the effect of the spatial distribution of the MM charges over the QM electron density will not lead to any loss of accuracy. After performing the integrals (as shown in App.(E)) the following analytical expressions are obtained:

$$\mathcal{H}_{\rho_e,q_a} = \int d^3r q_a \rho_e(\mathbf{r},\mathbf{r}_\alpha) \cdot \left[\frac{1}{|\mathbf{r}-\mathbf{r}_a|} - \frac{\exp^{-2\xi|\mathbf{r}-\mathbf{r}_a|}}{|\mathbf{r}-\mathbf{r}_a|} - \xi * \exp^{-2\xi|\mathbf{r}-\mathbf{r}_a|}\right] \tag{5.9}$$

$$\mathcal{H}_{\rho_N,q_a} = \int d^3r q_a \rho_N(\mathbf{r}_\alpha) \cdot \left[\frac{1}{|\mathbf{r}-\mathbf{r}_a|} - \frac{\exp^{-2\xi|\mathbf{r}-\mathbf{r}_a|}}{|\mathbf{r}-\mathbf{r}_a|} - \xi * \exp^{-2\xi|\mathbf{r}-\mathbf{r}_a|}\right] \tag{5.10}$$

From the above, we see that asymptotically (i.e. for $|\mathbf{r}-\mathbf{r}_a| \to \infty$), $\mathcal{H}_{\rho_e,q_a}$ converges to the coulomb potential $\frac{1}{|\mathbf{r}-\mathbf{r}_a|}$. Also for $\xi \to \infty$ (which recovers the point-charge description of the MM charge), the expression reduces to the usual Coulomb potential, as expected. At short distance the effect of the localized distribution of the MM charge introduces large cancellation to the Coulomb interaction and leads to a finite potential given by ξ (ξ has the dimension of 1/r). Thus this potential leads to zero forces as the distance approaches zero.

It is interesting and worthwhile to mention that the empirical form of the Coulomb potential proposed by Laio *et al.*[2] provides a very similar behavior; the two expressions differ marginally only at low and intermediate ranges, since both potentials converge to the value of $\frac{1}{r_{c,a}}$ at zero distance. As the value of the parameter λ is increased, one gradually approaches towards a point-charge description for the MM atom. At 0.97 Å (typical H-O separation in water) the value of the electrostatic potential of Eichinger *et al.*[35], Laio *et al.*[2] and the one derived by Biswas *et al.*[80]

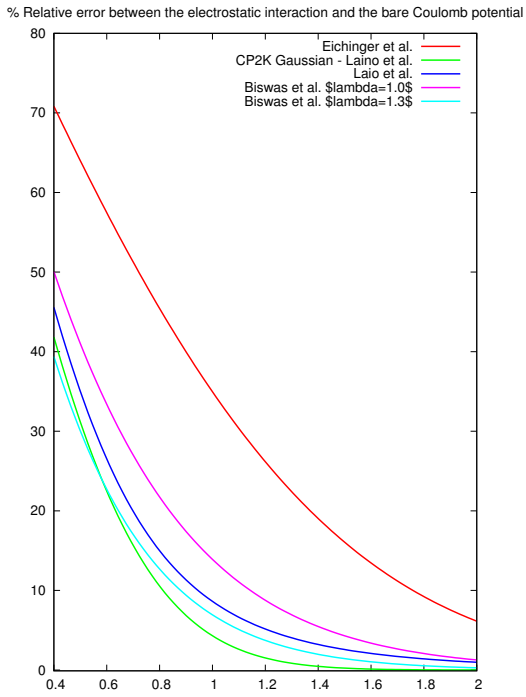

Figure 5.2: Relative % difference between different electrostatic interaction potential and the bare Coulomb interaction.

differ from the Coulomb potential arising from the point-charge description by about 9.5%, 1.3% and 1.9%, respectively (see Fig.(5.2)); all are smaller than the Coulomb potential of a point charge. It is worthwhile to emphasize that for $\lambda = 1.3$, the Coulomb potential approaches the point-charge potential faster and normalizes near 0.74 Å (interatomic separation in hydrogen molecule). The results of [80] show that a value of $\lambda = 1.3$ reduces the above difference of 1.9% (obtained with $\lambda = 1.0$) to 0.5% and the corresponding expansion of the point charge provides the best results [80]. Surprisingly, the empirical form of Laio *et al.*[2] describes the localized distribution of the MM point charge quite effectively and provides an understanding of the importance of accounting the smearing effect of the MM charge. As compared with the functional form of Laio *et al.*[2] and with the Biswas *et al.* potential [80] obtained with Slater orbital, the potential arising from a Gaussian distribution of the point charge [35] overestimates this effect by about 46%.

Since the modification in the Coulomb potential reflects a delocalization effect of the MM charge, both the QM electron density and the QM ionic cores should experience the same modified Coulomb potential. However, this is not strictly necessary as far as the full Hamiltonian treatment stays consistent in the definition of energy and derivatives. In fact in Laio *et al.*[2] they do not consider the smearing effect of the MM charge when computing the interaction with the ionic cores (see Sec. IV of Ref.[2]), thus replacing the modified Coulomb potential with a pure Coulomb interaction $\frac{1}{\mathbf{r}_\alpha - \mathbf{r}_a}$. Though the formalism presented in the next chapters (see Chap.(6) and

Chap.(7)) relies on a gaussian distribution for the point charge, both charge distribution densities (Gaussian and s-wave) are available in the QM/MM driver. Moreover, in the present implementation in CP2K I ensure that both the QM electrons and the ionic cores experience the same external potential.

Chapter 6

An efficient real space multi-grid QM/MM electrostatic coupling

In this chapter we will address the problem of optimizing the algorithm of the QM/MM electrostatic potential. In fact, while the cost of solving the Schrödinger equation in the QM part is the bottleneck of these calculations, evaluating the Coulomb interaction between the QM and the MM part can be surprisingly expensive: it can be just as time-consuming as solving the QM part. We present in this chapter a new real space multi-grid approach which handles Coulomb interactions very effectively. This algorithm has been implemented in the CP2K code [84]. This novel scheme cuts the cost of this part of the calculation by two orders of magnitude with respect to other schemes [2]. The method does not need fine tuning or adjustable parameters and it is quite accurate, leading to a dynamics with very good energy conservation.

6.1 Introduction

The study of chemical reactions in condensed phases is computationally demanding, owing not only to the size of the simulating system but also to the large degree of configurational sampling necessary to characterize a chemical reaction. This places severe demands on the efficiency of the implementation of any QM/MM scheme. Two main bottlenecks can be identified in such calculations: one concerns the evaluation of the QM energy and derivatives while the other is associated with the evaluation of the electrostatic interaction between the QM and the MM part. In this respect we can identify two classes of codes, those based on Gaussian-type orbitals (GTOs) to represent both the wave-function and the charge density [169, 170] and those using grids in real space to represent the charge density [171, 84, 172]. The latter encompasses both codes fully based on plane waves (PWs) and the more recent mixed approaches based on Gaussian plane waves (GPWs). It is on this second class of algorithms that this thesis is focused.

For localized basis sets (GTOs), the use of an efficient pre-screening technique is imperative in order to avoid the quadratic construction of the one-electron QM/MM Hamiltonian matrix. For non-local basis sets (PWs), if the interaction is evaluated analytically, the computational price is proportional to the number of grid points times the number of MM atoms. Surprisingly the evaluation of the QM/MM electrostatic interaction, for the latter scheme, requires between 20% and 100% of the time needed by the QM calculation, this in spite of the use of sophisticated hierarchical multipole (HMP) methods [173] or of clever implementations based on electrostatic cutoffs [2].

Furthermore these techniques require a fine tuning of parameters to yield optimal performance, and lead to a loss of accuracy that makes error control difficult.

In this chapter we describe a new implementation of the QM/MM coupling term that avoids the use of any hierarchical method or multipole technique. This novel scheme is based on the use of multi-grid techniques in conjunction with the representation of the Coulomb potential through a sum of functions with different cutoffs, derived from the new Gaussian expansion of the electrostatic potential (GEEP for short).

The overall speedup is of 1-2 orders of magnitude with respect to other PW-based implementations of the QM/MM coupling Hamiltonian [1, 2]. The lack of tuning parameters and electrostatic cutoffs makes this implementation a totally free parameter scheme, without any significant loss of accuracy. Consequently, very stable simulations can be obtained with optimal energy conservation properties.

6.2 Wave-function Optimization

Our implementation is based on the use of an additive [174, 166, 10] QM/MM scheme (See Chap.(2.3.1)). The total energy of the molecular system can be partitioned into three disjointed terms:

$$E_{TOT}(\mathbf{r}_\alpha, \mathbf{r}_a) = E^{QM}(\mathbf{r}_\alpha) + E^{MM}(\mathbf{r}_a) + E^{QM/MM}(\mathbf{r}_\alpha, \mathbf{r}_a) \tag{6.1}$$

where E^{QM} is the pure quantum energy, E^{MM} is the classical energy and $E^{QM/MM}$ represents the mutual interaction energy of the two subsystems. These energy terms depend parametrically on the coordinates of the quantum nuclei ($\mathbf{r}_\alpha$) and classical atoms ($\mathbf{r}_a$).

The quantum subsystem is described at the density functional theory (DFT) level, exploiting the QUICKSTEP [85] algorithm (See Chap.(3)).

The classical subsystem is described through the use of the MM driver called FIST, also included in the CP2K package. This driver allows the use of the most common force fields (see Chap.(4)) employed in molecular mechanics simulations [36, 37].

The interaction energy term $E^{QM/MM}$ contains all non-bonded contributions between the QM and the MM subsystem, and in a DFT framework we express it as:

$$E^{QM/MM}(\mathbf{r}_\alpha, \mathbf{r}_a) = \sum_{a \in MM} q_a \int \rho(\mathbf{r}, \mathbf{r}_\alpha) v_a(|\mathbf{r} - \mathbf{r}_a|) d\mathbf{r} + \sum_{a \in MM, \alpha \in QM} v_{VdW}(\mathbf{r}_\alpha, \mathbf{r}_a) \tag{6.2}$$

where $\mathbf{r}_a$ is the position of the MM atom a with charge q_a, $\rho(\mathbf{r}, \mathbf{r}_\alpha)$ is the total (electronic plus nuclear) charge density of the quantum system, and $v_{VdW}(\mathbf{r}_\alpha, \mathbf{r}_a)$ is the Van der Waals interaction between classical atom a and quantum atom α, and finally:

$$v_a(|\mathbf{r} - \mathbf{r}_a|) = \frac{\mathrm{Erf}(|\mathbf{r} - \mathbf{r}_a|/r_{c,a})}{|\mathbf{r} - \mathbf{r}_a|} \tag{6.3}$$

where $r_{c,a}$ is an atomic parameter, generally close to the covalent radius of the atom a. This function is the exact potential energy function originated by a Gaussian charge distribution $\rho(|\mathbf{r} - \mathbf{r}_a|) = \left(\frac{1}{\sqrt{\pi} * r_{c,a}}\right)^3 \exp(-(|\mathbf{r} - \mathbf{r}_a|/r_{c,a})^2)$. Moreover, the expression in Eq.(6.3) has the desired property of tending to 1/r at large distances and going smoothly to a constant for small r (see Chap.(5)).

Due to the Coulomb long-range behavior, the computational cost of the integral in Eq.(6.2) can be very large. When using a localized basis set like GTOs , the most natural way to handle this term is to modify the one-electron Hamiltonian by adding to it the contribution of the MM classical field:

$$H^{\mu\nu}_{QM/MM} = -\int \phi^*_\mu(\mathbf{r},\mathbf{r}_\alpha)\left[\sum_{a\in MM}\frac{q_a}{|\mathbf{r}_a-\mathbf{r}|}\right]\phi_\nu(\mathbf{r},\mathbf{r}_\alpha)d\mathbf{r} \tag{6.4}$$

ϕ_μ and ϕ_ν being Gaussian basis functions, depending parametrically on the QM nuclei positions $\mathbf{r}_\alpha$, and q_a the atomic charge of classical atom a with coordinates $\mathbf{r}_a$. In this case a suitable pre-screening procedure can be applied for the integral evaluation, in order to effectively compute only the non-zero terms and thus avoiding the quadratically scaling construction of the core Hamiltonian with respect to the number of elements of the basis set. When using a fully delocalized basis set like PWs, on the other hand, the QM/MM interaction term is evaluated by modifying the external potential and collocating on the grid nodes the contribution coming from the MM potential. Unfortunately the number of operations that a direct evaluation of Eq.(6.2) requires is of the order of $N_u N_{MM}$, where N_u is the number of grid points, usually of the order of 10^6 points, and N_{MM} is the number of classical atoms, usually of the order of 10^4 or more in systems of biochemical interest. It is evident that in a real system a brute force computation of the integral in Eq.(6.2) is impractical.

6.2.1 GEEP: Gaussian Expansion of the Electrostatic Potential

The key of our method is a decomposition of the electrostatic potential in terms of Gaussian functions with different cutoffs:

$$v_a(\mathbf{r},\mathbf{r}_a) = \frac{\mathrm{Erf}(|\mathbf{r}-\mathbf{r}_a|/r_{c,a})}{|\mathbf{r}-\mathbf{r}_a|} = \sum_{N_g} A_g \exp^{-(|\mathbf{r}-\mathbf{r}_a|/G_g)^2} + R_{low}(|\mathbf{r}-\mathbf{r}_a|) \tag{6.5}$$

The smoothed Coulomb potential is expressed as a sum of N_g Gaussian functions and of a residual function R_{low}. The A_g are the amplitudes of the Gaussian functions, G_g are their width. If the parameters A_g and G_g are properly chosen, the residual function R_{low} will be smooth, i.e. its Fourier transform will have a compact domain for very small g vectors, and will be approximately zero for $g >> G_{cut}$. The G_{cut} parameter is related to the spacing of the grid on which the R_{low} function will be mapped. We performed the fit of Eq.(6.5) by a least square approach in Fourier space, using the analytical expression of the g-representation of the modified electrostatic potential [175]:

$$\tilde{v}_a(\mathbf{g}) = \left[\frac{4\pi}{g^2}\right]\exp\left(-\frac{g^2 r^2_{c,a}}{4}\right) \tag{6.6}$$

In Fig.(6.1) we show the result of the fitting procedure in g-space with $r_{c,a} = 1.1$ Å, comparing the Fourier components of the modified Coulomb potential with the Fourier components of the residual function R_{low}. In this case the compact support of R_{low} is truncated at $G_{cut} \approx 1.0$ which should be compared with the value of $G_{cut} \approx 3.0$ needed to achieve the same accuracy when using $v_a(\mathbf{r},\mathbf{r}_a)$. This implies that the residual function can be mapped on a grid with a spacing one order of magnitude bigger than the one required to map the v_a function.

Figure 6.1: On the left: Gaussian expansion of the electrostatic potential (GEEP). The picture shows the components of the fit for the value $r_{c,a} = 1.1$ Å. On the right: Fourier transform of the potential in Eq.(6.3) (in red) and Fourier transform of the residual function R_{low} in Eq.(6.5) (in green). For this particular case ($r_{c,a} = 1.1$) we can define for the residual function a $G_{cut} \approx 1.0$.

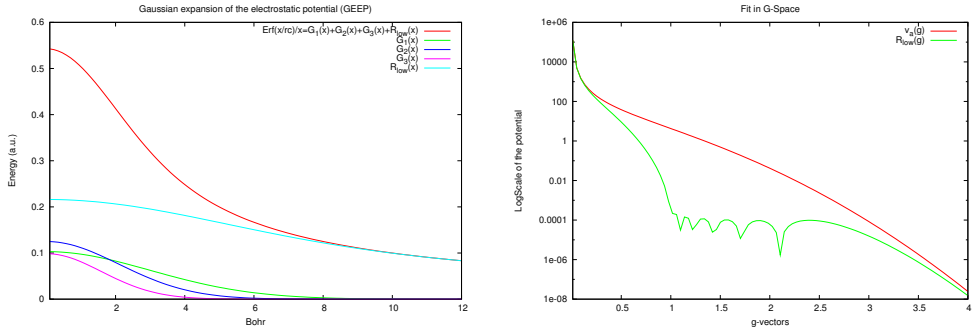

In Fig.(6.1) we show the same result of the fit in real space and in Table (6.1) we provide coefficients for selected values of $r_{c,a}$.

Table 6.1: Amplitudes and coefficients of the optimal Gaussians as derived by the fit

	Radius $r_{c,a} = 1.1$ Å		Radius $r_{c,a} = 0.44$ Å	
Number of Gaussians	A_g (a.u.)	G_g (bohr)	A_g (a.u.)	G_g (bohr)
1	0.103103	4.243060	0.230734	1.454390
2	0.125023	2.966300	0.270339	1.094850
3	0.098613	2.254250	0.075855	4.906710
4	-	-	0.190667	0.883485
5	-	-	0.173730	1.965640
6	-	-	0.127689	2.658160
7	-	-	0.095104	3.591640

The advantage of this decomposition scheme is that grids of different spacing can be used to represent the different contributions to $v_a(\mathbf{r}, \mathbf{r}_a)$. In fact, the evaluation of a function on a grid relies on the assumption that the grid spacing is optimally chosen on the basis of its Fourier transform spectrum. Writing a function as a sum of terms with compact support and with different cutoffs, the mapping of the function is achieved using different grid levels, in principle as many levels as contribution terms, each optimal to describe the corresponding function. In our case, sharp Gaussians require fine grids while coarser grids are necessary for the smoothest components. In addition the Gaussians can be truncated beyond a certain threshold value, which makes the collocation of the Gaussians on the grid a very efficient process (see App.(B)).

The problem of mapping a non-compact function on a fine grid is then converted into the mapping of N_g compact functions on grids with cutoffs lower or at least equal

to the fine grid, plus a non-compact very smooth function R_{low} mapped on the coarsest available grid. The sum of the contributions of all the grids, suitably interpolated, will be approximately equal to the function mapped analytically on the fine grid within errors due to the interpolation procedure.

6.2.2 GEEP library

A library with optimized parameters for the GEEP expansion is available into the CP2K code both for Gaussian and for s-wave (see App.(E)) charge distribution densities. In particular exploiting the scaling properties of both functional form it is possible to have a proper expansion for whatever value of the $r_{c,a}$ parameter.

6.2.3 Multi-grid Framework

Multi-grid methods are well established tools in the solution of partial differential equations [176, 177]. In the present implementation multi-grid techniques are employed to combine functions with different cutoffs, i.e. represented on different grid levels.

Let us start by considering two grids, a coarse grid $\mathcal{C}$ with N_c points and a fine grid $\mathcal{F}$ with N_f points, respectively at grid-level k-1 and k. The *interpolation* operator

$$I_{k-1}^{k} : \mathcal{C} \rightarrow \mathcal{F} \tag{6.7}$$

is by definition a transfer operator of a low cutoff function to a grid with an higher cutoff. The extension of the function to more points requires some regularity assumptions on its behavior. Two limiting cases can be identified: C^1 and C^∞, which can be handled with a simple linear interpolation scheme and with a $G-space$ interpolation, respectively. If the function is C^∞, as in the case of a Gaussian, it is normally better to use an interpolator that assumes a high regularity. This ceases to be true once a collocation threshold is defined for the mapping of the Gaussians. In fact, the function on the grid becomes less regular, and an interpolation of a lower order might perform better. Another reason to avoid G-space interpolation comes from the fact that periodic boundary conditions with respect to the QM grid cannot be applied to the QM/MM potential. This makes the normal $G-space$ interpolation unsuitable for our purpose. Thus we preferred to use an interpolation that works entirely in real space. For simplicity we use a set of commensurate grids, in which all the points of the coarse grid are points of the fine grid. Moreover, the number of points in each direction doubles going from the coarse to the fine grid level immediately above ($N_f = 8N_c$ in 3D). In the case of 1D space, the interpolation operator can be defined as:

$$I_{k-1}^{k}(i,j) = \sum_{n} T(i,n) S^{-1}(n,j) \tag{6.8}$$

where for the points away from the border $T(i,n) = N_3(n-i/2)$ and $S(i,j) = N_3(j-i)$; N_3 being the characteristic B-spline function of order 3 [178] (see App.(F)). The border was treated as a non-uniform B-Spline. Higher dimensional spaces can be treated using the direct product of the transformation along the single dimensions. The opposite operation, the *restriction* J_k^{k-1} is defined through the condition that the integral of the product of a function defined on the coarse grid with a function defined on a fine grid should give the same result both on the fine and on the coarse grid. Thus the restriction is simply the transpose of the interpolation

$$J_k^{k-1}(i,j) = \left[I_{k-1}^k(i,j)\right]^T = \sum_n S^{-1}(i,n)T(n,j) \tag{6.9}$$

Using N_{grid} grid levels and choosing the finer and coarser grid levels in order to treat correctly the sharpest and smoothest Gaussian components respectively, we can achieve good accuracy and performance.

6.3 QM/MM Energy

The QM/MM electrostatic energy within DFT can be expressed with the following equation:

$$E^{QM/MM}(\mathbf{r}_\alpha, \mathbf{r}_a) = \int d\mathbf{r}\rho(\mathbf{r}, \mathbf{r}_\alpha)V^{QM/MM}(\mathbf{r}, \mathbf{r}_a) \tag{6.10}$$

where $V^{QM/MM}$ is the electrostatic QM/MM potential evaluated on the finest grid, the same on which the final QM total density is evaluated. The overall description of the algorithm used to evaluate the QM/MM electrostatic potential on the finest grid can be outlined as follows:

- ⋆ Each MM atom is represented as a continuous Gaussian charge distribution. The electrostatic potential generating from this charge is fitted through a Gaussian expansion using functions with different cutoffs, Sec.(6.2.1).
- ⋆ Every Gaussian function is mapped on one of the available grid levels, chosen to be the first grid whose cutoff is equal to or bigger than the cutoff of that particular Gaussian function. Using this collocation criterion, every Gaussian will be represented on the same number of grid points irrespective of its width. In practice a submesh of size ≈ 25x25x25 is sufficient for an optimal Gaussian representation. Moreover, once a collocation threshold is defined, the Gaussian can be considered a compact domain function, i.e. it is zero beyond a certain distance, usually called Gaussian radius. Thus only MM atoms embedded into the QM box, or close to it, will contribute to the finest grid levels, as shown in Fig.(6.2).

  The result of this collocation procedure is a multi-grid representation of the QM/MM electrostatic potential $V_i^{QM/MM}(\mathbf{r}, \mathbf{r}_a)$, where i labels the grid level, represented by a sum of single atomic contributions $V_i^{QM/MM}(\mathbf{r}, \mathbf{r}_a) = \sum_{a\in MM} v_a^i(\mathbf{r}, \mathbf{r}_a)$, on that particular grid level. In a realistic system the collocation represents most of the computational time spent in the evaluation of the QM/MM electrostatic potential, that is around $60 - 80\%$.
- ⋆ Afterwards, the multi-grid expansion $V_i^{QM/MM}(\mathbf{r}, \mathbf{r}_a)$ is sequentially interpolated starting from the coarsest grid level up to the finest level. The QM/MM electrostatic potential on the finest grid level can then be expressed as:

$$V^{QM/MM}(\mathbf{r}, \mathbf{r}_a) = \sum_{i=coarse}^{fine} \prod_{k=i}^{fine-1} I_{k-1}^k V_i^{QM/MM}(\mathbf{r}, \mathbf{r}_a) \tag{6.11}$$

  where $V_i^{QM/MM}(\mathbf{r}, \mathbf{r}_a)$ is the electrostatic potential mapped on grid level i and I_{k-1}^k is the interpolation operator in real space. This operation does not depend

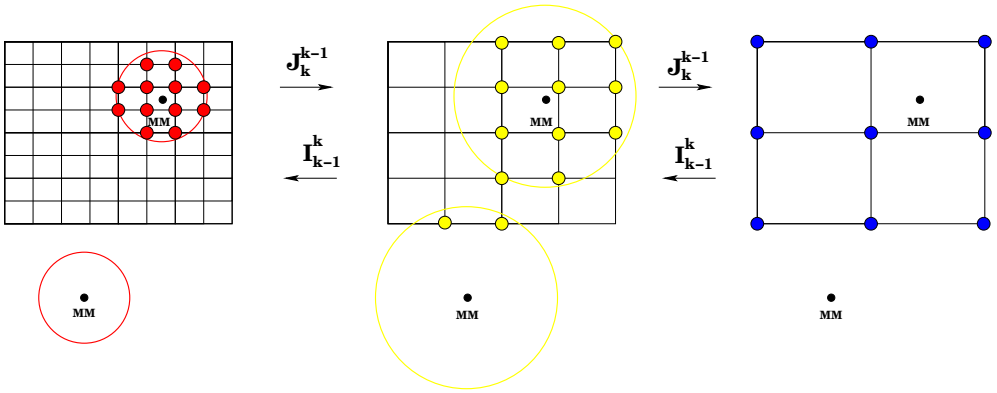

Figure 6.2: Schematic representation of the collocation procedure. Two MM atoms and three grid levels have been depicted. The circles (in the first and second grid levels) are the collocation region of the Gaussian centered on the two MM atoms. Atoms whose distance from the QM box is greater than the Gaussian collocation radius do not contribute to the potential on that grid level. However, all atoms contribute to the coarsest grid level through the long-range R_{low} part.

on the number of MM atoms but only on the number of grid points, i.e. on the cutoff used in the calculation and on the dimensions of the QM box. For realistic systems the computational cost is around $20-40\%$ of the overall cost of the evaluation of the QM/MM electrostatic potential.

Using the real space multi-grid technique together with the GEEP expansion, the prefactor in the evaluation of the QM/MM electrostatic potential has been lowered from $N_f * N_f * N_f$ to $N_c * N_c * N_c$, where N_f is the number of grid points on the finest grid and N_c is the number of grid points on the coarsest grid. The computational cost of the other operations for evaluating the electrostatic potential, such as the mapping of the Gaussians and the interpolations, becomes negligible in the limit of a large MM system, usually more than 600-800 MM atoms.

Using the fact that grids are commensurate ($N_f/N_c = 2^{3(N_{grid}-1)}$), and employing for every calculation 4 grid levels, the speed-up factor is around 512 (2^9); this means that the present implementation is 2 orders of magnitude faster than the direct analytical evaluation of the potential on the grid. The number of grid levels that can be used is limited by two technical factors. The first is that the coarsest grid needs to have at least as many points per dimension as the ones corresponding to the cutoff of the residual function R_{low} in order to perform the interpolation/restriction in an efficient manner. The second limitation is due to the constraint of using commensurate grid levels. The more grid levels are required in the calculation, the more the finest grid level cutoff will increase. This leads to an increment in memory requirements and to an unnecessary precision when handling the higher cutoff grids. Usually it is a combination of cutoff and grid levels that provides maximum efficiency. The two parameters can be chosen by checking that the coarsest grid level has no more than 5-10 grid points per dimension within the specified cutoff for the finest grid. Following the previous rule, the number of operations required for the direct evaluation of Eq.(6.2) is of the order of N*100*N_{MM}, where N is an integer between 1 and 10 and N_{MM} is

the number of classical atoms.

6.4 QM/MM Energy Forces

The forces on classical atoms due to the interaction Hamiltonian Eq.(6.10) are obtained by taking the derivative of Eq.(6.10) with respect to the classical atomic positions $\mathbf{r}_a$:

$$-\frac{\partial E^{QM/MM}}{\partial \mathbf{r}_a} = -\int \rho(\mathbf{r},\mathbf{r}_\alpha)\frac{\partial V^{QM/MM}(\mathbf{r},\mathbf{r}_a)}{\partial \mathbf{r}_a}d\mathbf{r} \tag{6.12}$$

The integral evaluation can be divided into terms deriving from the different grid levels:

$$-\frac{\partial E^{QM/MM}}{\partial \mathbf{r}_a} = -\sum_{i=coarse}^{fine}\int \rho(\mathbf{r},\mathbf{r}_\alpha)\frac{\partial V^{i,QM/MM}_{fine}(\mathbf{r},\mathbf{r}_a)}{\partial \mathbf{r}_a}d\mathbf{r} \tag{6.13}$$

where the $V^{i,QM/MM}_{fine}$ labels the potential term on the finest grid level coming from the corresponding grid level i. Using the multi-grid expression for terms $V^{i,QM/MM}_{fine} = \prod_{k=i}^{fine-1} I^k_{k-1} V^{QM/MM}_i$, the derivatives can be written as:

$$-\frac{\partial E^{QM/MM}}{\partial \mathbf{r}_a} = -\sum_{i=coarse}^{fine}\int \rho(\mathbf{r},\mathbf{r}_\alpha)\prod_{k=i}^{fine-1} I^k_{k-1}\frac{\partial V^{QM/MM}_i(\mathbf{r},\mathbf{r}_a)}{\partial \mathbf{r}_a}d\mathbf{r} \tag{6.14}$$

$$= -\sum_{i=coarse}^{fine}\int \left[\prod_{k=i+1}^{fine} J^{k-1}_k\right]\rho(\mathbf{r},\mathbf{r}_\alpha)\frac{\partial V^{QM/MM}_i(\mathbf{r},\mathbf{r}_a)}{\partial \mathbf{r}_a}d\mathbf{r} \tag{6.15}$$

In the previous equation the property that the interpolation operator is equal to the transpose of the restriction operator (and vice-versa) was used. The MM derivatives are then evaluated applying the restriction operator to the converged QM $\rho(\mathbf{r},\mathbf{r}_\alpha)$. This leads to a multi-grid expansion of the density and each integral is evaluated on the appropriate grid level. The overall derivative is the sum of the contributions of the different grid levels.

We now consider the forces on the QM atoms. If $n^\alpha_c(\mathbf{r})$ is the Gaussian density used to represent the core charge distribution of the α^{th} quantum ions and labeling with $P^{\mu\nu}$ the $\mu\nu$ element of the density matrix in the Gaussian basis set $\{\ \phi_\mu\ \}$, the forces on quantum ions (see also Sec.(3.3.2)) due to the QM/MM interaction potential are

$$-\frac{\partial E^{QM/MM}}{\partial \mathbf{r}_\alpha} = -\sum_{\mu\nu}(\frac{\partial P^{\mu\nu}}{\partial \mathbf{r}_\alpha})V^{QM/MM}_{\mu\nu} - \tag{6.16}$$

$$2\sum_{\mu\nu}P^{\mu\nu}\int(\frac{\partial \phi_\mu(\mathbf{r},\mathbf{r}_\alpha)}{\partial \mathbf{r}_\alpha})V^{QM/MM}(\mathbf{r},\mathbf{r}_a)\phi_\nu(\mathbf{r},\mathbf{r}_\alpha)d\mathbf{r} - \tag{6.17}$$

$$\int(\frac{\partial n^\alpha_c(\mathbf{r},\mathbf{r}_\alpha)}{\partial \mathbf{r}_\alpha})V^{QM/MM}(\mathbf{r},\mathbf{r}_a)d\mathbf{r} \tag{6.18}$$

where $V^{QM/MM}_{\mu\nu} = \int \phi_\mu(\mathbf{r},\mathbf{r}_\alpha)V^{QM/MM}(\mathbf{r},\mathbf{r}_\alpha)\phi_\nu(\mathbf{r},\mathbf{r}_\alpha)d\mathbf{r}$ is the QM/MM Hamiltonian interaction term in the Gaussian basis set $\{\ \phi_\mu\ \}$. The first term is the so-called Pulay term [179] and is present because the basis set depends explicitly on the atomic

position [85]. It vanishes if Gaussians form a complete basis set. The evaluation of the gradients on QM atoms is relatively inexpensive compared to a full quantum calculation. All considerations raised in Sec.(6.3), concerning the scaling of the present scheme in the evaluation of the QM/MM potential, remain valid in the evaluation of the forces on classical atoms.

The calculation of the forces within the present implementation has been compared with the calculation of the forces using the method described in [2], which is an implementation of QMMM in the CPMD code [171]. Comparison with the CPMD-QMMM code is complicated by the fact that in [2] a multipolar expansion is used for the long-range part of the QM/MM electrostatic coupling. For this reason we compare only forces on atoms of the first MM solvation shell, which are treated exactly also in CPMD-QMMM code. We consider a system of 215 classical SPC [180] water molecules and 1 QM water molecule. Although the system size is relatively small, the number of molecules present is comparable to the number of molecules normally treated exactly in CPMD-QMMM. In Fig.(6.4) we show the relative error between the previous and the present implementations. The highest relative errors (less than 1.0 %) correspond to forces which have small modules ($\leq 10^{-3} a.u.$). The average relative error is $\approx 0.01\%$ with a speed-up in the energy and derivative evaluation of a factor of 40 with respect to CPMD.

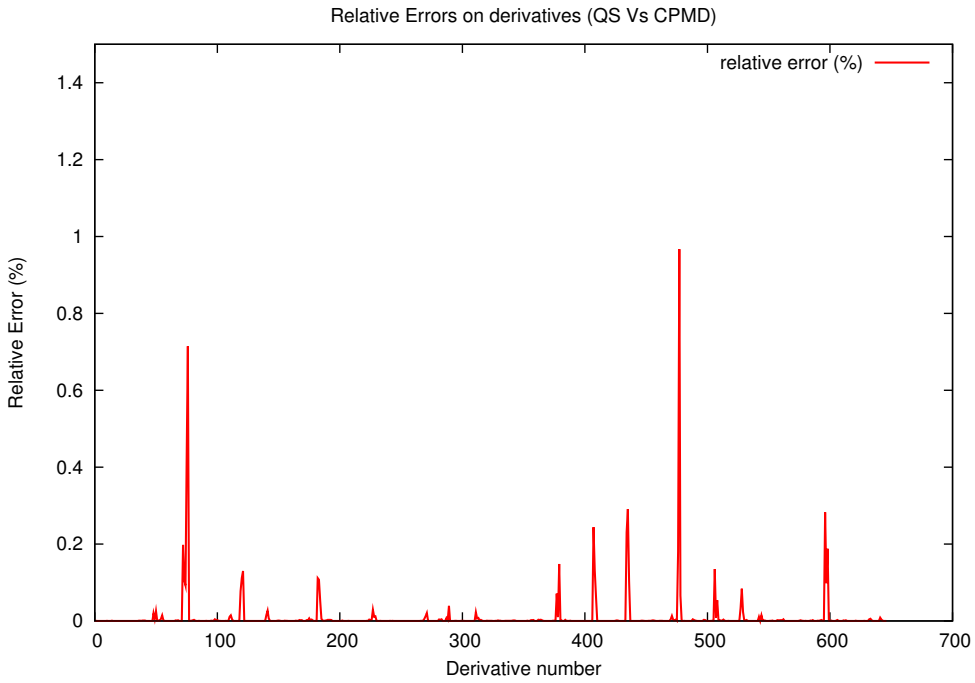

Figure 6.3: Relative errors on derivatives evaluated with the different functional form of Eq.(6.3) implemented in CPMD code and the new scheme implemented in CP2K. The average relative error is 0.01 %.

An important figure of merit for QM/MM codes that are aimed at molecular dynamics (MD) simulation is their ability to conserve the energy (see Sec.(2.7)). In order to address this issue we studied a system composed of 3 water molecules, 2 MM and 1 QM, equilibrated at 400K. We simulate this system for 1 picosecond. The results are shown in Fig.(6.3). For comparison the energy of the pure classical and the quantum run are shown in the same picture. No drift is observed during 1 picosecond of simulation. We also show the potential energy during the simulation, whose oscillation is ≈ 3 orders of magnitude bigger than the total energy oscillation.

Figure 6.4: On the left: energy conservation of a system composed of 3 water molecules equilibrated at 400K during 1 ps of simulation. The red line shows the total energy for the QM/MM run, the green line represents a pure classical run and the blue line shows a pure quantum run. The total energies have been shifted for better visualization. No drift is observed and all energy conservation is consistent. On the right: potential energy during the same run. Its variation is 3 orders of magnitude larger than the total energy variation.

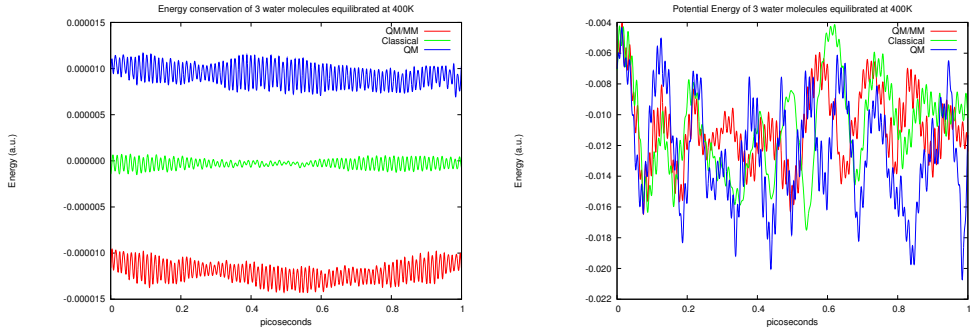

6.5 Results and Discussion

Consistently with checks done in previous work [2, 173], we test the accuracy of our implementation by computing the pair correlation function of a QM system embedded in a classical solvent. As found elsewhere [2], the smoothing radius plays an important role in determining the bond properties of the system, and the choice of this parameter can have dramatic effects on pair correlation functions. The use of a different functional form (cf. Eq.(6.3) with Eq.(3) of [2]) forced us to re-parameterize the $r_{c,a}$.

For the classical water molecules, the cutoff radii $r_{c,a}$ were chosen in order to reproduce the coordination number and the main peaks of the classical SPC water pair correlation function. A system of 2560 water molecules (2559 classical SPC water and 1 quantum water) in a cubic box, subject to periodic boundary conditions, was investigated. The system was previously equilibrated at $\rho = 1g/cm^3$, T=298K. One SPC water molecule was then replaced by a QM water molecule. GTH pseudo-potentials [118] were used to describe the core charge distribution and B-LYP exchange-correlation density functional [181, 182] was employed in all the calculations, in conjunction with

a plane-wave cutoff of $E_{cut} = 280$ Hartee. Several runs, with different values of the radius parameter $r_{c,a}$, were performed. The optimized radii are 0.44 Å for hydrogen and 1.20 Å for oxygen and allow the full classical SPC pair correlation function to be reproduced, as shown in Fig.(6.5). Due to the different functional form of Eq.(6.3), the optimal values found with our implementation are slightly different from the ones of ref. [2].

Figure 6.5: H-O and O-O pair correlation functions or QM water. QM/MM values are compared with the full classical SPC calculation. The QM/MM calculations are performed with $r_{c,a}$ equal to 1.2 Å for oxygen and 0.44 Å for hydrogen. The quantum box and the classical box employed in the simulation have a cube box size of 10.0 Å and 42.0 Å respectively. The roughness of the QM/MM curve is due to the much shorter simulation time. The bin size for the evaluation of the pair correlation function is of 0.2 Å.

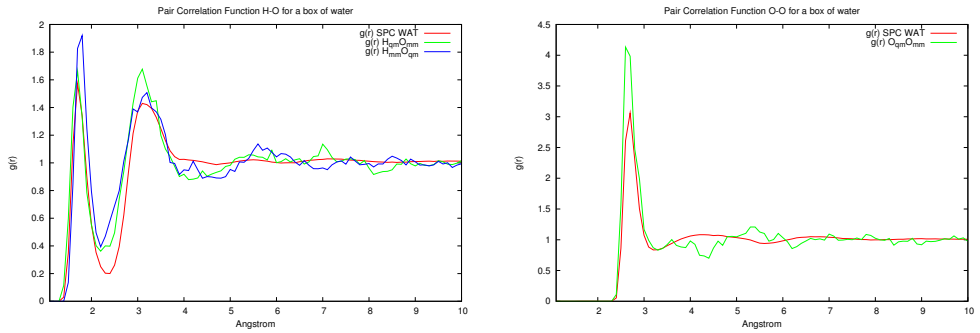

In order to test the transferability of the $r_{c,a}$ parameters determined for water, we also evaluated the pair correlation function of a QM di-peptide (GLY-ALA) zwitterion solvated in 3352 SPC water. We aimed at reproducing the pair correlation function obtained with the AMBER force field [37]. The pair correlation functions obtained with the present QM/MM implementation are indeed extremely close to the full classical results (see Fig.(6.6)).

6.6 Conclusions

In this chapter we presented an algorithm for evaluating the QM/MM coupling term with a fast linear scaling implementation. The main result is the dropping of the prefactor in the linear scaling, with a gain in the number of floating point operations proportional to $2^{3(N_{grid}-1)}$, where N_{grid} is the number of grid levels used in the multigrid framework. The evaluation of the electrostatic potential on a grid is proportional to the number of MM atoms times the number of grid points. In real systems the linear scaling evaluation of the potential is therefore characterized by a prefactor $\approx 10^6$. In this scheme the prefactor is instead $\approx 10^3$. The number of floating point operations is reduced several orders of magnitude and the computational time is 10-100 times smaller.

Figure 6.6: H_{pept}-O_{wat} and O_{pept}-H_{wat} pair correlation functions for the ALA-GLY di-peptide in SPC water. QM/MM values are compared with the full classical SPC calculation. The QM/MM calculations are performed with $r_{c,a}$ equal to 1.2 Å for oxygen and 0.44 Å for hydrogen. The quantum box and the classical box employed in the simulation have a cube box size of 15.0 Å and 50.0 Å respectively. A plane-wave cutoff of 280 Hartree was used during all the simulations, in conjunction with the GTH pseudo-potential and the BLYP exchange-correlation density functional. The roughness of the QM/MM curve is due to the much shorter simulation time. The bin size for the evaluation of the pair correlation function is of 0.2 Å.

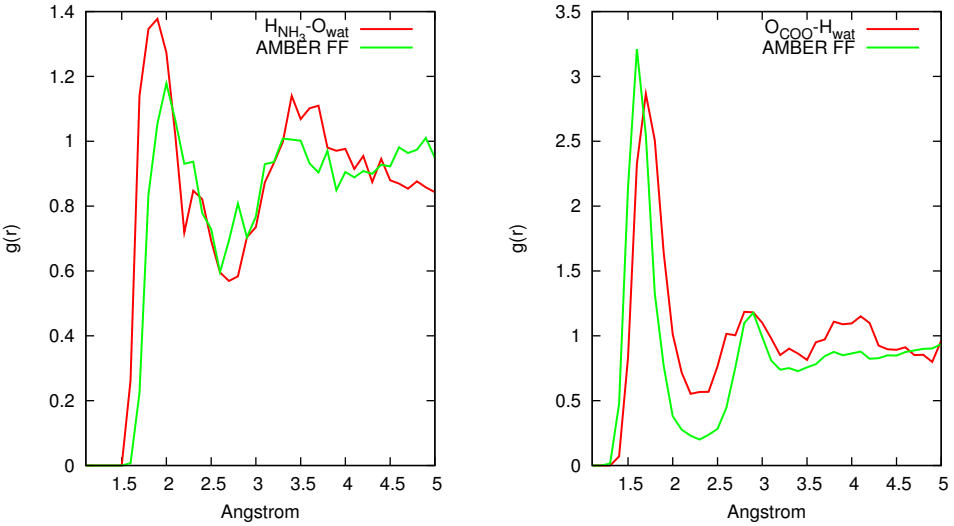

The algorithm is presently implemented in the package CP2K, released under GPL license and freely available on the internet [84]. The scheme was validated by checking the energy conservation and for a realistic system numerical accuracy was verified by comparing the forces with the analytical method, with a mean relative error of 0.01%. In addition, we computed the pair correlation function of a QM water molecule in classical water and of a QM zwitterionic di-peptide in classical water. The modified Coulomb interaction and the multi-grid approach reproduce correctly the structural properties of a QM water molecule solvated in classical water and the parameters obtained therein can be used effectively to describe the properties of an organic molecule containing both negatively and positively charged moieties, as in the case of the zwitterion.

The performance analysis confirms the present algorithm as the state of the art for the evaluation of QM/MM interaction coupling within a GPW scheme. Moreover, at variance with the majority of present-day QM/MM methods, our scheme does not rely on electrostatic cutoffs and so avoids all related problems. Consequently, the present method offers a fast, easy-to-use code for QM/MM calculations of large biological and inorganic systems.

Chapter 7

Periodic boundary conditions in QM/MM simulations

In this chapter we provide an extension to periodic boundary conditions of the method presented in Chap.(6) in order to treat properly the long-range electrostatic interactions in hybrid QM/MM simulations. The scheme has been implemented in the context of a QM calculation based on density functional theory (DFT). Results from QM/MM calculations with periodic boundary conditions (PBC) show that the use of PBC is essential when studying highly ordered crystal structures. The present method allows periodic boundary conditions to be used in molecular simulations of biological and material science systems.

7.1 Introduction

Understanding and predicting the properties of condensed systems requires, among other things, the reliable treatment of the long-range Coulomb interactions [183]. Many schemes have been proposed and a consensus has emerged regarding the use of periodic boundary conditions (PBC) to treat properly the interactions between the periodic replicas. In fact, it is usually believed that PBC have to be used together with an exact treatment of the long-range interactions between the periodically repeated images in order to obtain reliable MD simulations [184, 185, 186, 187, 188, 189].

Numerous methods have been developed to avoid the truncation of the electrostatic interactions beyond a given cutoff, and have been applied in the context of classical simulations [190, 191, 192, 193, 194, 195]. These methods are all based on different techniques to compute the lattice sum involved in the evaluation of the long-range electrostatic interactions within PBC.

The treatment of long-range forces in conjunction with PBC is much less well established for hybrid quantum mechanics/molecular mechanics (QM/MM) simulations. So far, most of the QM/MM implementations have relied on a spherical truncation scheme, in which the solute(QM)-solvent(MM) electrostatic interactions are neglected beyond a certain cutoff distance R_c. There are only a few exceptions. A very popular and inexpensive approach is the reaction field method, which couples the spherical truncation scheme with a polarizable continuum medium that extends beyond a cutoff distance R_c [196, 197, 198, 199, 200, 201] . Ewald's lattice summation technique were also investigated to treat the long-range QM/MM electrostatic interactions. Within a semi-empirical framework, the first implementation is due to Gao and Alhambra [202]. In their scheme only the long-range QM/MM interactions are evaluated, while

the QM/QM ones are omitted. For the particular set of applications tested by these authors, namely solvation phenomena, the solute-solvent (QM/MM) interactions were considered as the determining ones. Recent implementations of Ewald techniques extended to the full QM/MM long-range interactions [203, 204] show indeed that even for solvation cases long-range QM/QM electrostatic interactions play a significant role. Within a self-consistent DFT scheme, to the best of our knowledge there is only one QM/MM scheme that allows PBC [205] to be used. This approach is conceptually similar to the one we present here and it relies on the use of splines in reciprocal space (k-space), optimally designed for use within plane wave (PW) codes. Our approach is on the other hand, based on real space techniques, and is designed to be used with Gaussian basis codes, as is CP2K [84].

In Chap.(6) we proposed a new computational scheme based on the Gaussian expansion of the electrostatic potential (GEEP) [81]. This technique can be used efficiently to map functions on a grid and we applied it to the development of a new QM/MM electrostatic coupling for isolated systems which exhibits linear scaling.

The scheme presented in this chapter is implemented into the CP2K package [84], and extends the approach of Chap.(6) to applications where the use of PBC is required. It relies on the most efficient methods for calculating long-range electrostatic interactions of point charges within PBC and scales linearly with respect to the number of MM atoms. Moreover the evaluation of the MM electrostatic potential using PBC is independent of the number of QM atoms, depending only on the dimension of the coarsest grid used in the multi-grid approach.

An accuracy test was first performed on an analytically solvable model in order to provide a clear and unambiguous validation of the new approach. As a more realistic test case we apply the new method to the study of SiO_2 and its charged oxygen vacancy defect and on a zwitterionic di-peptide (GLY-ALA) in water. The tests show clearly that to achieve a correct description of the QM/MM system there are only two possibilities: the first is based on the optimization of the shape and charges of the MM crystal, in order to reproduce correctly the long-range stabilizing effects within a truncation scheme [206] and the other is to treat long-range interactions with a proper PBC scheme. Although results are similar for both approaches the use of QM/MM-PBC schemes avoids the preparation steps related to the fine tuning of the MM sub-system. For the solvated zwitterionic di-peptide we find, as expected, that the use of QM/MM-PBC can be avoided due to the high dielectric shield and to the lack of long-range stabilizing effects.

7.2 Methodology

Assuming the overall charge neutrality condition, the electrostatic interaction energy of a QM/MM simulation within PBC can be easily evaluated:

$$E^{TOT} = \frac{1}{2}\int_{\mathbb{R}^3}\int_{\mathbb{R}^3} dr dr' \frac{\rho(r)\rho(r')}{|r-r'|} \tag{7.1}$$

$\rho = \rho^{QM} + \rho^{MM}$ being the total charge density of the system (see Fig.(7.1-a)). Volumes integrals cover the full space $\mathbb{R}^3$ and will be omitted in the following to make notation lighter.

Figure 7.1: These frames show the decomposition of the total QM/MM energy. In each frame two of the many periodic replica have been shown. Frame Fig.(7.1-a) shows the total system. Frame Fig.(7.1-b) shows the energy of the MM sub-system embedded in the neutralizing background charge (deriving from the division of the QM and MM sub-systems). Frame Fig.(7.1-c) shows the energy of the QM sub-system with the neutralizing background charge of the QM cell and that relating to the MM cell. The last frame Fig.(7.1-d) depicts the QM/MM pure electrostatic mutual interaction term.

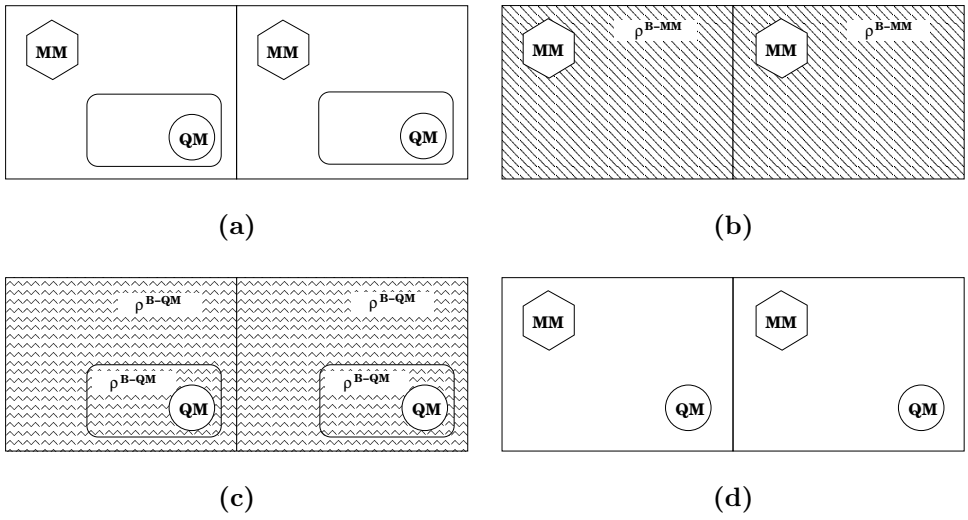

Once the total density is split into a QM and a MM part both sub-systems could in principle possess an overall net charge different from zero. Therefore the use of a neutralizing background charge (ρ^B) is necessary to avoid divergence in treating electrostatic within PBC. The total energy (see Fig.(7.1-a)) term can be split into three separate terms:

$$E^{MM} = \frac{1}{2}\int\int dr dr' \frac{(\rho^{MM}(r)+\rho^{B,MM})(\rho^{MM}(r')+\rho^{B,MM})}{|r-r'|} \tag{7.2}$$

$$E^{QM} = \frac{1}{2}\int\int dr dr' \frac{(\rho^{QM}(r)+\rho^{B,QM})(\rho^{QM}(r')+\rho^{B,QM})}{|r-r'|} \tag{7.3}$$

$$E^{QM/MM} = \int\int dr dr' \frac{(\rho^{QM}(r)+\rho^{B,QM})(\rho^{MM}(r')+\rho^{B,MM})}{|r-r'|} \tag{7.4}$$

The physical nature of these terms is illustrated pictorially in Fig.(7.1). Assuming the total charge of the system is zero (although this assumption can be relaxed with no modifications to the formalism) the mixed terms involving the neutralizing background charge of the $E^{QM/MM}$ cancel the interaction terms of the QM and MM density with their own background charges. The expression for the three terms is:

$$E^{MM} = \frac{1}{2}\int\int dr dr' \frac{(\rho^{MM}(r))(\rho^{MM}(r'))}{|r-r'|} \tag{7.5}$$

$$E^{QM} = \frac{1}{2}\int\int drdr' \frac{(\rho^{QM}(r))(\rho^{QM}(r'))}{|r-r'|} \tag{7.6}$$

$$E^{QM/MM} = \int\int drdr' \frac{(\rho^{QM}(r))(\rho^{MM}(r'))}{|r-r'|} \tag{7.7}$$

The first term (Eq.(7.5) and Fig.(7.1-b)) is evaluated using standard techniques such as particle-particle or particle-mesh schemes [192, 194]. The second term (Eq.(7.6) and Fig.(7.1-c)) is the Hartree energy of the QM sub-system. Since the total energy of the QM sub-system is usually evaluated exploiting a smaller cell, care needs to be taken to include the correct electrostatic interactions of the periodic QM replicas, i.e. restore the correct periodicity (MM cell). The last term (Eq.(7.7) and Fig.(7.1-d)) is the evaluation of the periodic MM electrostatic potential, partitioned into a real space contribution and a periodic correction. The real space term contains the interaction due to the short-range part of the electrostatic potential of the MM charges with the total quantum charge distribution (electrons plus nuclei). Only MM atoms close to the QM region will contribute to this term. The periodic term contains instead the long-range effects of the MM sub-system.

In the next section, the standard Ewald method is briefly reviewed for a N-point charge particle system interacting in an orthorhombic box of edge L_x, L_y, L_z. We then introduce the Ewald lattice summation with the GEEP scheme [81]. Finally we discuss the algorithm to decouple/recouple multiple QM images. In the following Latin letters a, b will be used to index the MM atoms, while Greek letters α, β will be used for QM atoms.

7.2.1 Ewald lattice summation for electrostatic interactions

Given an N-point charge particle system, the electrostatic potential $\Phi_{tot}(\mathbf{r})$ at position $\mathbf{r}$ is evaluated using the Ewald lattice sum technique [190]. In this approach, $\Phi_{tot}(\mathbf{r})$ is split into the sum of two potentials, using a Gaussian screening charge of width κ:

$$\Phi_{tot}(\mathbf{r}) = \Phi_{rec}(\mathbf{r}) + \Phi_{real}(\mathbf{r}) \tag{7.8}$$

The reciprocal space potential term $\Phi_{rec}(\mathbf{r})$ is determined using the Fourier series:

$$\Phi_{rec}(\mathbf{r}) = \frac{4\pi}{V}\sum_{\mathbf{k}\neq 0}\frac{e^{-\frac{k^2}{4\kappa}}}{k^2}\sum_{a}^{MM} q_a e^{-\imath\mathbf{k}\cdot|\mathbf{r}-\mathbf{r}_a|} \tag{7.9}$$

where $\mathbf{k} = [2\pi n_x/L_x^2, 2\pi n_y/L_y^2, 2\pi n_z/L_z^2]$ and V is the volume (V=L_x·L_y·L_z) of the primary unit cell. The real space part of the Ewald potential is given by:

$$\Phi_{real}(\mathbf{r}) = \sum_{a}^{MM}\sum_{|\mathbf{L}|\leq L_{cut}} q_a \frac{\mathrm{Erfc}(\kappa|\mathbf{r}-\mathbf{r}_a+\mathbf{L}|)}{|\mathbf{r}-\mathbf{r}_a+\mathbf{L}|} \tag{7.10}$$

where $\mathbf{L} = [n_x L_x, n_y L_y, n_z L_z]$ counts the periodic images and n_x, n_y and n_z are integers. As the Erfc has a real space short-range property, only the $|\mathbf{L}| \leq L_{cut}$ periodic images will contribute to the real space term of the electrostatic potential.

7.2.2 QM/MM periodic potential

The QM/MM periodic potential (see Eq.(7.7) and Fig.(7.1-d)) on a generic point i of the finest grid level can be computed using the real space lattice sum:

$$V^{fine}(\mathbf{r}_a)_i = \sum_{a}^{MM} \sum_{\mathbf{L}}^{\infty}{}' q_a v_a(\mathbf{r}_i, \mathbf{r}_a + \mathbf{L}) \tag{7.11}$$

where $\mathbf{r}_i$ is the coordinate of the point i of the finest grid level and $\mathbf{r}_a$ indexes the functional dependence from the set of MM atomic coordinates and v is given by Eq.(6.3). The summation over $\mathbf{L}$ involves all integer translations of the real space lattice vectors $\mathbf{L} = [n_x L_x, n_y L_y, n_z L_z]$ for integers n_k and the prime symbol indicates that when $\mathbf{L} = 0$ the term $|\mathbf{r}_i - \mathbf{r}_a| = 0$ is neglected. The summation in Eq.(7.11) has the same convergence properties as the standard Ewald summation schemes [190].

The total QM/MM electrostatic energy can be split into two rapidly convergent terms [207, 190], one over real space and the other over reciprocal space lattice vectors:

$$E^{QM/MM}(\mathbf{r}_\alpha, \mathbf{r}_a) = E^{QM/MM}_{real}(\mathbf{r}_\alpha, \mathbf{r}_a) + E^{QM/MM}_{recip}(\mathbf{r}_\alpha, \mathbf{r}_a) \tag{7.12}$$

where:

$$E^{QM/MM}_{real}(\mathbf{r}_\alpha, \mathbf{r}_a) = \int d\mathbf{r}\rho(\mathbf{r}, \mathbf{r}_\alpha) V^{QM/MM}_{real}(\mathbf{r}, \mathbf{r}_a) \tag{7.13}$$

and

$$E^{QM/MM}_{recip}(\mathbf{r}_\alpha, \mathbf{r}_a) = \int d\mathbf{r}\rho(\mathbf{r}, \mathbf{r}_\alpha) V^{QM/MM}_{recip}(\mathbf{r}, \mathbf{r}_a) \tag{7.14}$$

The definition of the two terms is strictly connected to the type of functional form used to describe the Coulomb interactions. In our case, since we decided to treat the MM classical charges through a Gaussian charge distribution, the electrostatic potential function has the analytical form:

$$v_a(\mathbf{r}, \mathbf{r}_a) = \frac{\mathrm{Erf}(|\mathbf{r} - \mathbf{r}_a|/r_{c,a})}{|\mathbf{r} - \mathbf{r}_a|} \tag{7.15}$$

easily represented as a sum of two terms [81]:

$$v_a(\mathbf{r}, \mathbf{r}_a) = \frac{\mathrm{Erf}(|\mathbf{r} - \mathbf{r}_a|/r_{c,a})}{|\mathbf{r} - \mathbf{r}_a|} = \sum_{N_g} A_g \exp(-\frac{|\mathbf{r} - \mathbf{r}_a|^2}{G_g^2}) + R_{low}(|\mathbf{r} - \mathbf{r}_a|) \tag{7.16}$$

The best choice is to use the mathematical properties of the two functional forms (short-range term and long-range term) to define the division into real and reciprocal space contributions:

$$\begin{aligned} v_a(\mathbf{r}, \mathbf{r}_a) = \frac{\mathrm{Erf}(|\mathbf{r} - \mathbf{r}_a|/r_{c,a})}{|\mathbf{r} - \mathbf{r}_a|} &= \sum_{N_g} A_g \exp(-\frac{|\mathbf{r} - \mathbf{r}_a|^2}{G_g^2}) + R_{low}(|\mathbf{r} - \mathbf{r}_a|) \\ &= v_a^{rs}(\mathbf{r}, \mathbf{r}_a) + v_a^{recip}(\mathbf{r}, \mathbf{r}_a) \end{aligned} \tag{7.17}$$

All short-range interactions will be evaluated in the real space while all long-range interactions will be taken into account in the reciprocal space formalism. The real space term $V^{QM/MM}_{real}(\mathbf{r}, \mathbf{r}_a)$ is defined as:

$$V_{real}^{QM/MM}(\mathbf{r},\mathbf{r}_a) = \sum_{|\mathbf{L}|\leq L_{cut}} \sum_a q_a v_a^{rs}(\mathbf{r},\mathbf{r}_a+\mathbf{L})$$
$$= \sum_{|\mathbf{L}|\leq L_{cut}} \sum_a q_a \left[\sum_{N_g} A_g \exp(-\frac{|\mathbf{r}-\mathbf{r}_a+\mathbf{L}|^2}{G_g^2}) \right] \tag{7.18}$$

where a labels the MM atoms. The radii of the Gaussians are such that only a few periodic images ($|\mathbf{L}| \leq L_{cut}$, ideally only one) are needed to achieve convergence of the real space term, while others give zero contribution. As in [81], each Gaussian of Eq.(7.18) is mapped on the appropriate grid level. The same approach outlined here for Gaussian charge distribution holds for the s-wave charge expansion.

The effect of the periodic replicas of the MM sub-system is only in the long-range term, and it comes entirely from the residual function $R_{low}(\mathbf{r},\mathbf{r}_a)$ of Eq.(7.17):

$$V_{recip}^{QM/MM}(\mathbf{r},\mathbf{r}_a) = \sum_{\mathbf{L}}^{\infty}{}' \sum_a q_a v_a^{recip} = \sum_{\mathbf{L}}^{\infty}{}' \sum_a q_a R_{low}(|\mathbf{r}-\mathbf{r}_a+\mathbf{L}|) \tag{7.19}$$

Performing the same manipulation used in Ewald summation [190] (see App.(D)) the previous equation can be computed more efficiently in the reciprocal space:

$$V_{recip}^{QM/MM}(\mathbf{r}_i,\mathbf{r}_a) = L^{-3} \sum_{\mathbf{k}}^{k_{cut}}{}' \sum_a \tilde{R}_{low}(\mathbf{k}) q_a \cos\left[2\pi\mathbf{k}\cdot(\mathbf{r}_i-\mathbf{r}_a)\right] \tag{7.20}$$

The term $\tilde{R}_{low}(\mathbf{k})$, representing the Fourier transform of the smooth electrostatic potential, can be evaluated analytically:

$$\tilde{R}_{low}(\mathbf{k}) = \left[\frac{4\pi}{|\mathbf{k}|^2}\right] \exp\left(-\frac{|\mathbf{k}|^2 r_{c,a}^2}{4}\right) - \sum_{N_g} A_g (\pi)^{\frac{3}{2}} G_g^3 \exp(-\frac{G_g^2|\mathbf{k}|^2}{4}) \tag{7.21}$$

The potential in Eq.(7.20) can be mapped on the coarsest grid. In fact, the long-range contribution is physically very smooth and a good representation can be achieved with large grid spacings. Furthermore, since the R_{low} function is a low cutoff function, $\tilde{R}_{low}(\mathbf{k})$ is zero for all k-vectors larger than a well defined k_{cut}. The k_{cut} parameter depends strongly on the number of Gaussian functions used in the GEEP scheme (as described in Sec.(6.2.1)).

Once the electrostatic potential of a single MM charge within periodic boundary conditions is derived, the evaluation of the electrostatic potential due to the MM sub-system is easily computed employing the same multi-grid operators (interpolation and restriction) described in Sec.(6.2.3) and in App.(F).

7.2.3 Periodic coupling with QM images

In the present section we complete the description of the electrostatic coupling, discussing the interaction between the periodic images of the QM replicas (see Fig.(7.1-c)). The Quickstep [85, 208] algorithm uses a mixed plane wave / Gaussian basis set to solve the DFT equations for the quantum sub-system. The plane waves are used to compute efficiently the Hartree potential. Therefore, unless the quantum box and

the MM box have the same dimensions, the QM images, interacting by PBC implicit in the evaluation of the Hartree potential, have the wrong periodicity.

In order to avoid this error, the QM problem is usually solved using standard decoupling techniques [209, 210]. This approximation is legitimate when the evaluation of the QM/MM potential is performed using spherical truncation schemes for Coulomb interactions.

Since we want to describe the long-range QM/MM interaction with periodic boundary conditions, we may not neglect the QM/QM periodic interactions, which play a significant role if the QM sub-system has a net charge different from zero or a significant dipole moment. Therefore we exploit a technique recently proposed by Blöchl [210], for decoupling the periodic images and restoring the correct periodicity also for the QM part. A full and comprehensive description of the methods to evaluate energy corrections and derivatives is given in reference [210]. Here we summarize Blöchl's decoupling scheme. Given a QM total density charge $\rho(\mathbf{r}, \mathbf{r}_\alpha)$, the electrostatic energy of this isolated density is:

$$E = \frac{1}{2} \int_V d\mathbf{r} \int d\mathbf{r}' \frac{\rho(\mathbf{r}, \mathbf{r}_\alpha)\rho(\mathbf{r}', \mathbf{r}_\alpha)}{|\mathbf{r} - \mathbf{r}'|} \tag{7.22}$$

Let us introduce a new model charge density $\hat{\rho}(\mathbf{r}, \mathbf{r}_\alpha)$, which is localized within the same volume V as $\rho(\mathbf{r}, \mathbf{r}_\alpha)$ and which reproduces the multipole moments of the correct charge distribution. The representation adopted in [210] is given by the sum:

$$\hat{\rho}(\mathbf{r}, \mathbf{r}_\alpha) = \sum_\alpha q_\alpha g_\alpha(\mathbf{r}, \mathbf{r}_\alpha) \tag{7.23}$$

of atom-centered spherical Gaussians, which are normalized such that they posses a charge of one:

$$g_i(\mathbf{r}, \mathbf{r}_\alpha) = \frac{1}{(\sqrt{\pi} r_{c,\alpha})^3} \exp(-\frac{|\mathbf{r} - \mathbf{r}_\alpha|^2}{r_{c,\alpha}^2}) \tag{7.24}$$

where $\mathbf{r}_\alpha$ denotes a particular atomic site. Every atomic site may be the center of various Gaussians with different decay lengths $r_{c,\alpha}$. By construction, the multipole moments of the model charge density agree with those of the original charge distribution. Since the electrostatic interaction of separated charge distribution (the array of periodic QM charge densities) depends only on its multipole moments, the model charge density is used to modify the Hartree potential and to cancel the electrostatic interactions between the periodic images. In App.(C), we briefly summarize with a matrix formalism the charge fit scheme as derived in [210]. In the same way as the Blöchl scheme cancels the electrostatic interactions between periodic images, it is possible to use it to include the electrostatic interactions between periodic images with the periodicity of the MM box.

7.2.4 QM/MM forces

The derivatives on MM atoms can be easily evaluated taking the derivative of both terms in real space and in reciprocal space, and summing the contribution of the different grid levels. The derivatives of the real space term are the same as the one

presented in Sec.(6.4). The derivatives of the reciprocal space term need to be evaluated by deriving the MM nuclei potential energy contribution and integrating this derivative with the quantum charge distribution:

$$\frac{\partial E_{recip}^{QM/MM}(\mathbf{r}_\alpha, \mathbf{r}_a)}{\partial \mathbf{r}_a} = \int d\mathbf{r}\rho(\mathbf{r}, \mathbf{r}_\alpha)\frac{\partial V_{recip}^{QM/MM}(\mathbf{r}, \mathbf{r}_a, \mathbf{r}_\alpha)}{\partial \mathbf{r}_a} = \tag{7.25}$$

$$\Delta\omega \sum_{\mathbf{r}_i} \rho(\mathbf{r}_i, \mathbf{r}_\alpha) L^{-3} \sum_{\mathbf{k}}^{k_{cut}} {}' \sum_{a}^{MM} \tilde{R}_{low}(\mathbf{k}) q_a \frac{\partial \cos\left[2\pi\mathbf{k}\cdot(\mathbf{r}_i - \mathbf{r}_a)\right]}{\partial \mathbf{r}_a} \tag{7.26}$$

where $\Delta\omega$ is the volume element of the coarsest grid level. This contribution is summed with the terms in real space to obtain the total derivatives on MM atoms. The derivatives on QM atoms are computed in the same way as we described in Sec.(6.4), the only difference being that the QM derivatives are modified by the coupling/decoupling terms. These corrections have been derived and extensively discussed in [210].

7.3 Tests and Applications

Four systems were selected to test the new method. The first one, an infinite array of Gaussian alternating opposite charges, can be solved analytically and therefore provides a clear and unambiguous test of the accuracy of our new approach.

The second system is a periodic model of α-quartz (α-SiO_2) where a bulk fragment, described at the DFT level, is embedded in the environment of classical atoms described with MM force fields. The third system analyzes a charged oxygen vacancy defect in α-quartz, in the same periodic model. These two systems do not possess an analytical solution but both have been extensively studied experimentally [211, 212, 213, 214, 215, 216, 217, 218] and theoretically [219, 220, 221, 222, 223, 224, 225, 226, 227].

The last system is a zwitterionic di-peptide (GLY-ALA) in water. It was chosen since it represents an extreme test where the use of PBC is expected to have minor effects on the electronic structure properties.

7.3.1 Analytical test

In order to validate this new algorithm, we consider the electrostatic interaction of an array of Gaussian charge distributions:

$$\rho(\mathbf{r}_\alpha) = (\kappa/\pi)^{3/2} \exp(-\kappa^2 |\mathbf{r}_\alpha|^2) \tag{7.27}$$

κ being the width of the Gaussian charge density.

The charges (32 positively charged (+1) and 32 negatively charged (-1)) are arranged on a cubic array of points forming a NaCl lattice. Neighboring charges have opposite sign. The potential generated by such a set of charges can be calculated exactly by noting that the electrostatic potential of a single charge density (Eq.(7.27)) at an arbitrary distance $\mathbf{r}$ can be determined analytically, $V_{ext}(\mathbf{r}) = \mathrm{Erf}(\kappa\mathbf{r})/\mathbf{r}$. We now construct a test QM/MM model, selecting two neighboring charges (see Fig.(7.2)) and calculating the Hartree potential in a smaller orthorhombic cell centered around the two chosen charges. This calculation would have been a necessary step had we

Figure 7.2: Orthorhombic cell of face centered cubic lattice of Gaussian charges. The two big spheres represent the QM atoms. Lattice parameter 17.2 Å. The Gaussian charges have a width of $0.5\sqrt{2}$ Å

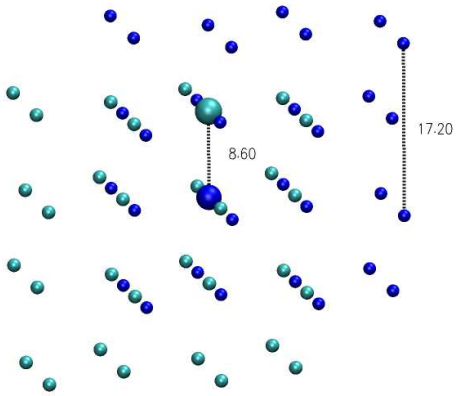

treated the two selected centers quantum mechanically instead of with a fixed nuclear charge distribution. The calculation was performed using a plane wave cutoff of 25 Ry and 3 Gaussians were used for each selected atom to build the model density used to decouple/recouple the periodic images.

Table 7.1: The interaction of a Gaussian charge distribution in a 3-dimensional lattice as shown in Fig.(7.2) as a function of the number of Gaussians used in GEEP and as a function of the QM cell. * The QM/MM non-periodic calculation was performed with 64000 MM atoms arranged in a cube cell of 344.0 Å.

QM Cell (x,y,z) (Å)	Num. Gauss.	k_{cut} (bohr^{-1})	E_{tot} (Hartree)	ΔE (mHartree)
34.4 34.4 34.4	Analytical Calculation		3.441010	
34.4 34.4 34.4	6	0.5	3.440520	0.49
34.4 34.4 34.4	6	0.7	3.441176	-0.17
34.4 34.4 34.4	6	1.0	3.441119	-0.11
34.4 34.4 34.4	6	2.0	3.441070	-0.06
34.4 34.4 34.4	6	0.5	3.440520	0.49
34.4 34.4 34.4	9	0.5	3.440687	0.33
34.4 34.4 34.4	12	0.5	3.440885	0.12
34.4 34.4 34.4	15	0.5	3.440895	0.11
34.4 34.4 34.4	15	0.5	3.440895	0.11
27.0 27.0 27.0	15	0.5	3.440978	0.03
34.4 27.0 27.0	15	0.5	3.440951	0.06
22.0 22.0 12.0	15	0.5	3.440865	0.14
12.0 12.0 12.0	15	0.5	3.441356	-0.35
34.4 34.4 34.4	QM/MM non-periodic*		3.443106	2.10

In Table (7.1) we show how this pseudo QM/MM calculation depends on parameters like the QM cell dimension (affecting the coupling/decoupling between QM periodic

images), the k_{cut} parameter of Eq.(7.20) and the number of Gaussians used in the GEEP scheme. In particular we note that the number of Gaussians is strictly correlated to the k_{cut} value. In fact, the more Gaussians that are used in the GEEP scheme, the more the R_{low} will be a low cutoff function. This permits a smaller k_{cut} parameter to be used in order to reach the same accuracy (see Table (7.1)).

The choice of the dimension of the QM box is almost irrelevant for the accuracy of the results (see Table (7.1)). In fact even using a box of 12.0 Å, which is the smallest possible box size usable with this QM sub-system, we find accurate results. We remark that other decoupling techniques [209, 205] require boxes twice the size of the minimum box, leading to a substantial computational overhead.

Moreover we computed the pseudo QM/MM interaction energy for the non-periodic pseudo QM/MM calculation, using an MM environment of 64000 atoms (MM cell side of 344.0 Å). The result shows that for ordered structures surface effects are very important and the only way to include correctly the electrostatic interactions is by using PBC. Overall this test indicates that the new proposed scheme is both valid and efficient. In terms of computational time no additional overhead was noted when performing pseudo QM/MM calculation with or without PBC.

7.3.2 SiO_2

We now consider a realistic problem, a crystal of α-SiO_2 (α-quartz) in an orthorhombic cell, subject to periodic boundary conditions. Several QM/MM schemes have been proposed in the literature for silica-based systems [228, 229, 230, 231, 232, 233, 234, 206], differing in the description of the quantum-classical interface and of the classical region. All of them treat the QM/MM long-range interaction with a truncation scheme, properly optimizing the charges of the H-atoms terminating the MM cluster or its shape in order to recover the correct long-range effects.

The MM crystal we used for this test is made up of 15552 atoms (5184 SiO_2 units) in an orthorhombic cell of 49.94, 57.66 and 63.49 Å. The system was optimized using the empirical pair potential of van Beest [41] which is known to provide a reliable description of bulk α-SiO_2 [235]. A fragment of 160 atoms was described at the QM level Fig.(7.3), describing the oxygen boundary atoms with a core charge increased by 0.4 in order to maintain the neutrality of the overall system. This boundary scheme will be described in details in Sec.(8.2). DFT calculations with Gödecker-Tetter-Hutter (GTH) [118] pseudo-potentials [118] using local density approximation to describe the exchange-correlation functional were performed on the QM site using a cutoff of 200 Ry. We optimized the wave-function with and without the use of periodic boundary conditions. The results show that the use of periodicity is essential to treat highly ordered crystal structures. Without periodic boundary conditions we find the Kohn-Sham gap to be 0.12 eV which is much lower than the experimental band gap of about 9 eV [236, 237] and than the computed Kohn-Sham gap of 5.8 eV [220]. Also the population analysis gives an indication that the lack of PBC leads to an incorrect description of the system. In fact by population analysis [210] we find that many oxygen atoms have a positive charge while some silicon atoms have a negative charge. If we use periodic boundary conditions, on the other hand, we find results that agree with those previously published. In particular, using PBC, we find for the Kohn-Sham band gap a value of 6.23 eV using the same computational parameters as in the case of non-PBC. The population analysis shows the proper charge distribution with charges

close to +2.0 and -1.0 for silicon and oxygen respectively.

After removing the atom depicted in Fig.(7.3) from the same crystal structure, we studied the charged oxygen vacancy defect in SiO_2 with the same computational setup used for stoichiometric SiO_2.

Figure 7.3: The picture shows the QM cluster. Silicon atoms in yellow, oxygen in red, boundary oxygen atoms (treated increasing the core charge by 0.4) in purple and in blue the oxygen atom (OX) removed to create the oxygen vacancy defect.

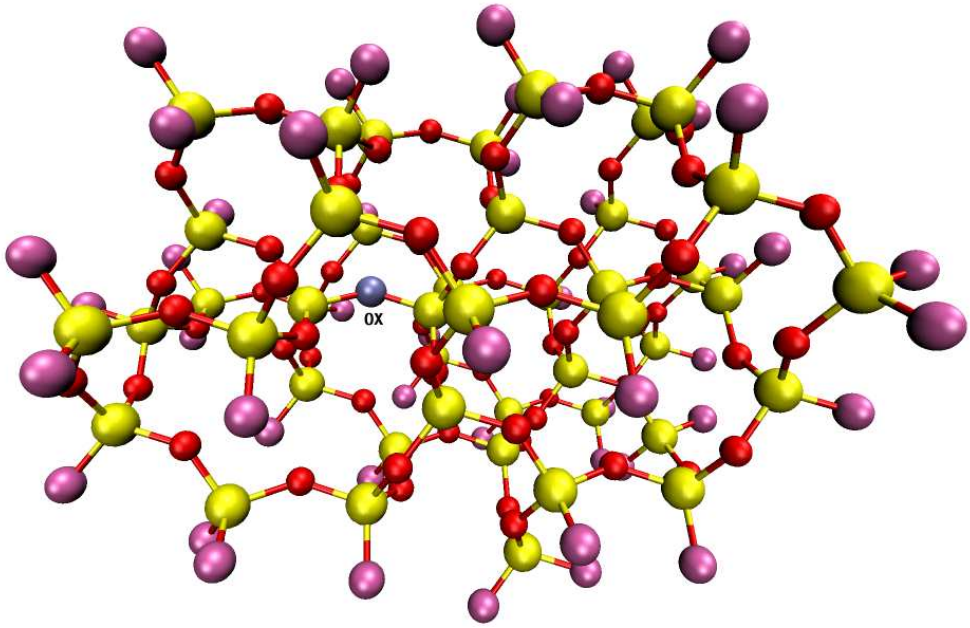

As for quartz the lack of PBC leads to an incorrect description for both the electronic structure and the population analysis. The use of the present scheme gives a Kohn-Sham band gap of 3.18 eV, as against the theoretical result [220] of 3.30 eV. The value obtained without PBC is 0.0089 eV. Unlike the other QM/MM schemes used for silica we do not use any additional charge to terminate the MM cluster and no particular attention was paid to the choice of its shape. The computational cost for the evaluation of the QM/MM-PBC electrostatic potential on this system accounts for 5% of the total cpu time of a single MD step. In particular 1 MD step (energy and forces), on Cray-XT3 using 32 processors, requires 7 minutes. 23 seconds out of 7 minutes are used to evaluate the QM/MM electrostatic potential. Without using the long-range PBC option the computational time used for the construction of the QM/MM electrostatic potential is roughly 12 seconds. Thus, the use of PBC does not represent a significant overhead in the overall computation scheme, making feasible the study of crystal structures within a QM/MM-PBC framework.

7.4 GLY-ALA

The results obtained for SiO_2 both with and without PBC could in principle be attributed to the peculiar electronic structure of this material (with a partial ionic/covalent structure). Therefore we further tested both QM/MM schemes, with and without PBC, on a zwitterionic di-peptide (GLY-ALA) in water, where the long-range stabilizing effects due to the Madelung potential are not present. We expect small effects from using PBC with this particular system.

Using the same description for the QM system as the one described in Sec.(6.5), we find that PBC do not affect the value of the Kohn-Sham gap or the charge population analysis with respect to the common implementations where a truncation scheme was used. This is due to the large dielectric constant of water and to the lack of long-range stabilizing effects such as the Madelung potential in an ionic crystal.

7.5 Conclusions

In this chapter we proposed a new scheme designed to include the effects of periodic boundary conditions into hybrid QM/MM descriptions of chemical/biological systems. The present scheme uses the Gaussian expansion of the electrostatic potential (GEEP) Sec.(6.2.1) and is implemented in the CP2K package [84]. Through the use of a modified Ewald lattice summation it is possible to include the effects of the periodic boundary conditions in the evaluation of the MM electrostatic potential. The scheme preserves the linear-scaling property of the GEEP technique and is computationally efficient. The method has no additional overhead with respect to the evaluation of the QM/MM electrostatic potential with a truncation scheme using a spherical cutoff. The new scheme is validated with an analytical model and with three real test cases: the α-quartz crystal and its charged oxygen vacancy defect and a zwitterionic di-peptide (GLY-ALA) in water. It is clear from these tests that the use of periodic boundary conditions together with a proper treatment of the long-range interactions is required for ordered systems, unless a careful truncation scheme optimizing the shape and dipole of the MM environment is used. Therefore, it is now possible to perform routinely *ab initio* molecular dynamics and electronic structure calculations in crystal systems. The scheme has been developed describing the electrons with DFT but the extension to other quantum chemical schemes (Hartree-Fock and post Hartree-Fock methods) is straightforward.

Part IV

Applications

Chapter 8

A Quickstep-based QM/MM approach for silica

QM/MM approaches are currently used to describe several properties of silica-based systems, which are local in nature and require a quantum description of only a small number of atoms around the site of interest, e.g. local chemical reactivity or spectroscopic properties of point defects. In this chapter we show step by step the validation of a QM/MM scheme for silica using the QM/MM framework described in Chap.(6), within the QUICKSTEP approach for the description of the quantum region. This scheme has been validated by computing the structural and dynamical properties of an oxygen vacancy in α-quartz, a prototypical defect in silica. We will show that good convergence in the Si-Si bond length and formation energy is achieved by using a quantum cluster of only eight atoms in size. We check the suitability of the method for molecular dynamics and evaluate the Si-Si bond frequency from the velocity-velocity correlation function.

8.1 Introduction

Silica is pervasive in present technologies, its applications ranging from optical fibers to metal-oxide-semiconductor devices and even to car tires. *Ab initio* studies have provided important insight on the properties of bulk phases, defects and surfaces of silica [238, 239, 240, 241]. The usual approach in the *ab initio* modeling of condensed matter systems makes use of supercells with periodic boundary conditions containing at most few hundreds of atoms. However, if one is interested in the study of point defects as an impurity atom or a vacancy, the use of a full quantum periodic model implies an extremely high concentration of defects with a consequently strong defect-defect interaction due to the limited supercell size. On the other hand, the use of a full quantum cluster model, popular in the chemistry community, suffers from other limitations, since also in this case the size of the system can not exceed, typically, one hundred atoms. Long range electrostatic interactions are not kept into account and local relaxation associated, e.g. with defect formation, is partially hindered by the boundary atoms that have to be held fixed in order to prevent a global rearrangement of the cluster. However the properties to be addressed are often local in nature, such as the structure and spectroscopic properties of point defects or the chemical reactivity of specific sites. In these cases, a quantum mechanical description is necessary only for a small number of atoms around the site of interest, the rest of the system

affects the local properties only via long range electrostatic interactions and geometrical constraints. For this class of problems the QM/MM approach offers a satisfactory compromise between accuracy and computational efficiency [174]. By embedding a quantum mechanics calculation in a classical molecular mechanics model of the environment, the hybrid QM/MM schemes attempt to incorporate environmental effects at an atomistic level, including such influences as mechanical constraints, electrostatic perturbations and dielectric screening.

Several QM/MM schemes have been proposed in literature for silica-based systems [228, 229, 230, 231, 232, 242, 243, 233, 234], differing in the description of the quantum-classical interface and of the classical region. In this chapter we present a QM/MM scheme for silica suitable for implementation in the general QM/MM framework described in this thesis.

Our specialization of the general QM/MM scheme to silica has been validated by computing the structural and dynamical properties of an oxygen vacancy in α-quartz, a prototypical defect in silica. For this benchmark case, we consider the effect on the accuracy of the description of several factors: i) the total size of the system (MM+QM); ii) the size of the QM subsystem; iii) the manner in which the valence at the boundary of the QM system is saturated; iv) the basis set. In this manner we provide an optimized setup for performing molecular dynamics QM/MM simulations in silicon dioxide. The quality of the description is demonstrated by performing a long molecular dynamics at finite temperature on the oxygen vacancy described with a minimal QM/MM model. We have found that convergence in the properties of the defect is already achieved with a very small quantum subsystem composed of eight atoms only. The combination of the QM/MM approach with the use of a localized basis set for the quantum cluster calculations makes long molecular dynamics simulations affordable at a low computational cost, e.g. 14 hours/ps on a single Opteron processor (2.2 GHz) for a system made of 8 QM atoms and 1764 MM atoms.

8.2 Method of calculations

The validity of a QM/MM scheme relies on few ingredients: the way in which bonded interactions between atoms in the classical and quantum region are described; the way in which electrostatic interaction between the two subsystem is treated; the quality of the classical force field. Finally, if the QM/MM scheme is aimed at performing molecular dynamics, a variational formulation of the total energy with respect to the atomic positions is also required.

For what concerns the classical force field, the most sophisticated QM/MM scheme presently available in literature is probably that proposed by Sulimov *et al.* in Ref. [229] where they use a classical region which includes up to several hundred polarizable atoms within a shell model , surrounded by a first region with non-polarizable point charges ions and by an outer region treated as a polarizable continuum. Here, we use a the van Beest, Kramer, van Santen (BKS) potential (see Eq.(4.9)). Even this simplified description of the classical subsystem does not affect significantly the accuracy of the description as we will show in Sec.(8.3) for the test case we considered. The condition of neutrality of the system imposes that $q_O = -\frac{1}{2}q_{Si}$. The charge of silicon ion is +2.4 e. The parameters for the short range interaction A,b,C are given in Ref.[41]. This potential has been successfully applied to the study of the phase

diagram of crystalline silica [244] and also provides a useful model of the amorphous phase [235].

Performing a QM/MM calculation on silica requires the description of a "pseudobond" between an MM Si and a QM O, or, vice versa, between an MM O and a QM Si. If, for example, the QM system is a six member ring, each Si atom will have two dangling bonds, whose valence has to be saturated in some way. Several strategies have been explored in the literature, for silica or similar systems, involving e.g. the introduction of extra "dummy" hydrogen atoms [245, 246, 247], or the ad hoc parameterization of a pseudo potential for the boundary atoms [63, 62, 60, 248, 249]. This latter approach has been adopted, for instance,in the QM/MM scheme for silica of Ref.[229]. We here propose a manner for capping the QM region that does not require the introduction of extra atoms, and makes use of the ordinary pseudo potential also for the boundary atoms. We choose the QM region in such a manner that the boundary QM atoms are always oxygen atoms. The pseudo potential of these atoms (that from now we indicate with O*) is the ordinary one. To saturate the valence of the boundary oxygen atoms we add one electron for each O*, which would ideally come from the neighboring MM Si. In order to enforce global charge neutrality, we change the ionic charge of the boundary oxygen pseudo potential from 6 to 6.4. Hence, the total charge of the QM system is $(0.4-1)\,n_{O^*} = -0.6 n_{O^*}$ which is equal to the total charge of the classical atoms that have been replaced by the QM atoms. In fact, in a system in which all the silicon atoms are four-fold coordinated while all the O-atoms are two-fold coordinated the number of boundary oxygens is given by $n_{O^*} = 4n_{Si} - 2n_O$, where n_{Si}, n_O are the number of QM Si and QM O respectively. Therefore, since the charge of classical Si and O are 2.4 and -1.2 respectively, the total classical charge of the QM subsystem is indeed $2.4n_{Si} - 1.2n_O = -0.6\,(+4n_{Si} - 2n_O) = -0.6n_{O^*}$, equal to the QM charge.

The total energy of the system depends variationally on the coordinates of the quantum ($\mathbf{r}_i^{QM}$) and classical ($\mathbf{r}_i^{MM}$) atoms and its functional form has been described in Chap.(6).

We perform DFT calculation in the local density approximation (LDA), by using Gaussian based pseudo potentials [118] with a DZVP atomic basis set and expanding the electron density in plane-waves with an energy cutoff of 240 Ry.

The interaction energy term, $E_{QM/MM}$ is expressed as:

$$E_{QM/MM}(\mathbf{r}^{QM},\mathbf{r}^{MM}) = \sum_{i\in MM} q_i \int d\mathbf{r} \frac{\mathrm{erf}(\frac{|\mathbf{r}-\mathbf{r}_i^{MM}|}{r_{c,i}})\rho_{QM}(\mathbf{r})}{|\mathbf{r}-\mathbf{r}_i^{MM}|} + \sum_{\substack{i\in MM\\ j\in QM}} V_{ij}(\mathbf{r}_i^{MM},\mathbf{r}_j^{QM}) \tag{8.1}$$

where $\rho_{QM}(\mathbf{r})$ is the total (electronic plus nuclear) charge density of the quantum system. Eq.(8.1) corresponds to Eq.(6.2), but the Van der Waals interactions have been replaced with a more general potential ($V_{ij}(\mathbf{r}_i^{MM},\mathbf{r}_j^{QM})$).

All the classical steric and electrostatic interactions between QM atoms are set to zero. Instead, a classical short range potential of the form (Eq.(4.9)) is introduced between O^* and the first classical silicon atoms. The parameters of the interaction are obtained by performing a series of full QM calculations on a H_3Si-O-Si-O-Si-H_3 cluster by varying the distance between the central Si and one of the two oxygen atoms while keeping other angles and distances fixed (see Fig.(8.1)). This distance dependence has

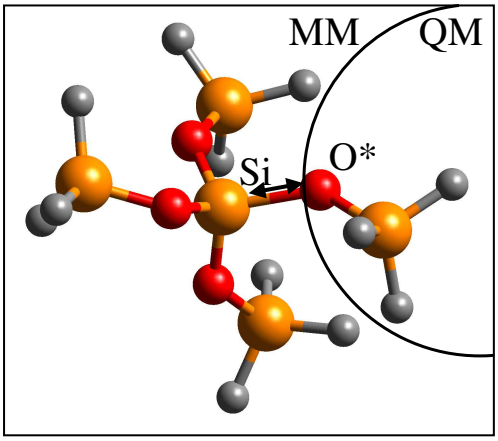

Figure 8.1: Structure of the small cluster used for the fitting of the short range potential between the boundary $O^*$and the first classical silicon. The arrows indicate the Si-O bond elongated. Si, O and H atoms are depicted in yellow, red, and grey, respectively.

then been fitted with the functional form (Eq.(4.9)). The parameters obtained with this procedure are A=603935406. K, b=5.6077 $Å^{-1}$, C=2244282. K/$Å^6$. These values are only slightly different from those of the van Beest, Kramer, van Santen potential.

In order to test the quality of our QM/MM model, we consider a big cluster of α-quartz made by an integer number of SiO_2 units saturated with hydrogens. The system is divided in two regions, one treated within the ab-initio framework (QM region), the second treated by a classical force field (MM region). In real applications, the QM subregion should ideally be as small as possible for reasons of computational efficiency. With this goal in mind, we benchmark our QM/MM model by considering the structural properties of a 6-member ring embedded in MM SiO_2 and the formation energy of the neutral oxygen vacancy with QM subsystems of various size.

8.3 Validation of the QM/MM approach

8.3.1 Geometry of the 6-member ring in α-quartz.

We first consider a rather small SiO_2 cluster composed of 164 atoms saturated with H atoms. This system is chosen because it can be optimized at the full QM level. The QM region is a ring made by six member ring approximately at the center of this cluster (see Fig.(8.2)). In order to reduce possible long range electrostatic effects we optimized the charges of the classical H-atoms terminating the cluster in order to reproduce the full QM dipole moment. The position of the H-atoms and of the Si and O atoms connected to them are held fixed in the geometry optimization using both the QM/MM or MM Hamiltonian.

The difference between the QM/MM and the full QM geometry is used as a measure of the quality of the capping and of the QM/MM Hamiltonian.

By using the capping scheme described in Sec.(8.2), we perform a geometry optimization of the system using the QM/MM Hamiltonian (Eq.(8.1)). The results are shown in Fig.(8.3), in which the full QM, MM and QM/MM structures are superimposed. The differences between these structures are small, especially for what concerns the QM subsystem. The value of the root mean square deviation (RMSD) between

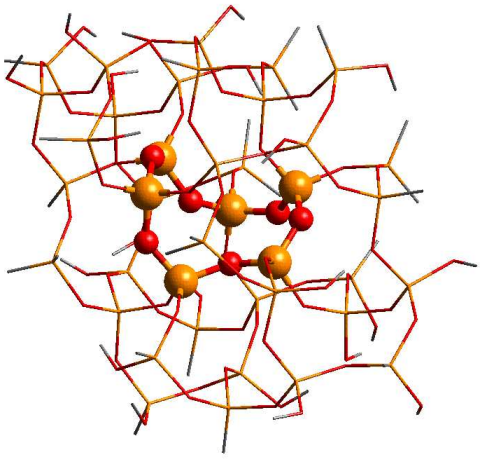

Figure 8.2: Structure of the cluster with a QM six-membered ring (depicted with spheres). The color code is the same as in Fig.(8.1).

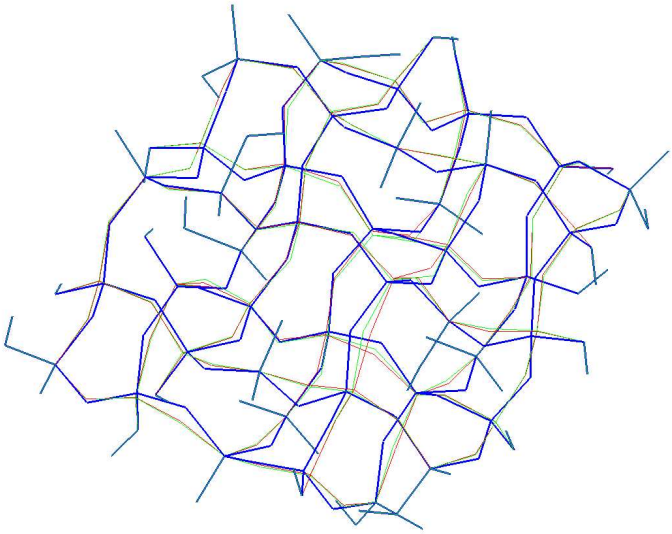

Figure 8.3: Superposition of the geometries obtained from a full quantum (blue line), a full classical (red line) and a QM/MM optimization (green line).

the QM/MM and full QM geometries is computed for the QM subsystem, the full cluster and the boundary atoms. The results are reported in Table (8.1).

For a comparison, we also considered capping schemes in which the valence of the QM system is saturated by dummy hydrogen atoms. If the last QM atom is an oxygen, the H is placed in the direction of the first MM Si. Hence, the QM subsystem will be terminated by -OH moieties (Model "OH"). If the last QM atom is a Si, the H is placed in the direction of the first MM oxygen (Model "H"). The RMSD for

RMSD	RING [Å]	INTERFACE [Å]	FULL [Å]
MM	0.248	0.254	0.199
QM/MM O*	0.183	0.221	0.196
QM/MM O-H	0.275	0.403	0.254
QM/MM Si-H	0.191	0.276	0.206

Table 8.1: RMSD of the MM structure and the QM/MM O*, O-H, Si-H terminated with respect to the QM structure in three different case: in case RMSD_{RING} we compare only the 6SiO atoms of the ring; in case $\text{RMSD}_{INTERFACE}$ we compare the positions of all the QM atoms and the MM boundary atoms (for MM case we chose the same atoms of O* and O-H cases); in case RMSD_{FULL} we compare the positions of all the atoms.

these two models are also reported in Table (8.1). The ratio of the SiO/SiH bond lengths for "H" capping or the ratio OH/SiO for "OH" capping have been fixed at the values determined in a preliminary full quantum optimization. The model "OH" shows a large RMSD for both the ring and interface regions. This is due to a large difference in the SiOH angle (115^o) of the silanol with respect to the SiOSi angle (145^o) in α-quartz, as already pointed out by by Sauer *et al* in Ref. [228]. However the "OH" capping might perform better for small silica clusters with smaller SiOSi angles [242, 243]. The model "SiH" performs better than the "OH" model, but still show large deviation in the interface region. However, since we have not attempted to reparameterize the short range potential at the interface as we did for the O* capping, we must say that there is still room for improvement for the "H" capping.

8.3.2 Formation energy of an oxygen vacancy in α-quartz.

We now consider the formation energy and the structure of the neutral oxygen vacancy defect in α-quartz. We use the experimental structural parameters: a=4.913 Å, c/a=1.100 [250, 211]. Removal of an oxygen atom produces a relaxation of the lattice with a formation of a Si-Si covalent bond, whose length is much shorter than the equilibrium Si-Si distance in a perfect lattice (3.08 Å). Theoretical studies report that the equilibrium distance of the Si-Si bond is in the range 2.3-2.6 Å[229, 251, 222, 252, 253, 227]. The predicted value is strongly affected by the size of quantum system in cluster and periodic calculations. Also for the formation energy, the values reported in literature depend significantly on the model (full QM cluster, full QM periodic or QM/MM) and on the basis set. Boureau and Carniato [254] found that the formation energy of the neutral oxygen vacancy must be larger than 7.3 eV from purely thermodynamic arguments. Density-functional-theory calculations in periodic models give 6.97 eV [251], 7.85 eV[222], 9.6 eV[252] at the LDA level and 8.64 eV at the GGA level[252]. Hartree-Fock calculations on an isolated cluster give 6.7 eV and 5.5 eV with and without the *d* functions in the basis set and 8.5 eV including correlation energy at the MP2 level [253, 227]. Sulimov *et al.* [229], using a QM/MM approach with the QM region treated at the unrestricted Hartee-Fock level (UHF), have obtained a formation energy of 6.08 eV with the 6-31G* basis set used, which corresponds to ours.

They have also found that the formation of a Si-Si bond induces a strong anisotropic relaxation of the lattice that extends up to 13 Å from the defect. They also find a Si-Si distance of 2.32-2.40 Å depending from the basis set used (2.37 Å with a basis

set equivalent to ours).

We compute the formation energy using the QM/MM Hamiltonian described in Sec.(8.2), considering the effect of several factors that could influence the accuracy of the calculation.

We first consider the effect of the size of QM subsystem, computing the formation energy for the three QM subsystems shown in Fig.(8.4). The smaller system (9 atoms)

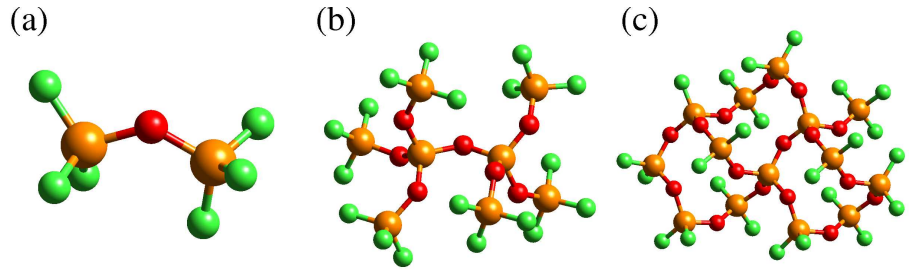

Figure 8.4: Structure of three different QM clusters used for the study of the oxygen vacancy. (a) $Si_2OO_6^*$, (b) $Si_8O_7O_{18}^*$, (c) $Si_{14}O_{16}O_{24}^*$. Si, O and O* are depicted in yellow, red, and green, respectively.

is the $O\left(SiO_3^*\right)_2$ moiety. The oxygen atoms in the SiO_3^* groups are boundary atoms, while the central O is removed to generate the vacancy. The average and large QM subsystems are composed of all the SiO_2 units within three and five bond separation from the oxygen that is removed, i.e. 33 or 54 atoms, respectively. For all the three cases, the QM subsystem is embedded in a classical cluster composed of 508 SiO_2 units. The Si and the O atoms at the boundary of the classical cluster are saturated by hydrogen ions of charges -0.6 and +0.6, respectively.

The vacancy formation energy is given by

$$\Delta E^{form} = E(O) + E(vacancy) - E(quartz). \tag{8.2}$$

The energy of the isolated oxygen $E\left(O\right)$ is obtained as $E\left(O\right) = \frac{1}{2}\left(E\left(O_2\right) + E^{diss}\left(O_2\right)\right)$ where $E\left(O_2\right)$ is the ab-initio total energy of the O_2 molecule in the triplet state and $E^{diss}\left(O_2\right) = 5.16$ eV is the experimental dissociation energy of O_2[255]. The correction due to the basis set superposition error (BSSE) is about 0.1 eV. The results are shown in Table (8.2). We estimated the BSSE with the counterpoise correction [256] separately for the three energy terms in Eq.(8.2) as follows: i) the correction to perfect quartz is the difference in total energy due to the addition to the basis set of a ghost oxygen atom which forms a O_2 molecule with the oxygen removed in the vacancy formation; ii) E(O) is calculated with a full basis set of i); iii) the correction to the E(vacancy) is obtained by using the full basis set of i) in the unrelaxed vacancy configuration.

We have also checked the dependence of the geometry and formation energy on the basis set by performing additional calculations on the smaller cluster ($Si_2OO_6^*$) with the TZVP and TZV2P basis sets. The results are reported in Table (8.3) and show that the DZVP basis set is accurate enough for structural properties, but formation

	dist Si-Si [Å]	ΔE [eV]	ΔE^{CP} [eV]
QM+MM regions:	1764 atoms		
(A) $Si_2OO_6^*$	2.35	7.34	-0.11
(B) $Si_8O_7O_{18}^*$	2.36	7.31	-0.12
(C) $Si_{14}O_{16}O_{24}^*$	2.40	7.36	-0.13
QM+MM regions:	773 atoms		
(B) $Si_8O_7O_{18}^*$	2.35	7.36	-0.12

Table 8.2: Si-Si bond length, vacancy formation energy (ΔE) and the counterpoise correction ΔE^{CP} (included in ΔE) for different size of the QM and MM regions. The DZVP basis set has been used.

	dist. Si-Si [Å]	ΔE [eV]	ΔE^{CP} [eV]
DZVP	2.35	7.34	-0.11
TZVP	2.34	7.44	-0.08
TZV2P	2.34	7.91	-0.07

Table 8.3: Si-Si bond length, vacancy formation energy (ΔE) and the counterpoise correction ΔE^{CP} (included in ΔE) for different basis sets.

energies change sizably with the basis set as already found in Hartree-Fock calculation with smaller basis sets in Ref [229].

As a final remark, we note that for a crystalline system the Madelung field in the quantum region would strongly depend on the value of the classical charges in the MM region. Different MM models with different charges might provide similar bulk properties, e.g. bulk structure of the glass, along with different local Madelung fields. Therefore, particular care must be paid in using QM/MM when the properties of charged defects are addressed, e.g. the heterolytic breaking of a siloxane bond. The QM/MM scheme we propose is expected to correctly describe the elastic response of the of the system surrounding the quantum region. Its applicability to study of any other local properties of the quantum region which would depend on the details of the Madelung field must be carefully checked. In this respect, the BKS potentials we have used is probably better than others available in literature also in describing the local Madelung field since the classical charges are fitted on ab-initio data. In our benchmark application the vacancy is a neutral defect and the problems outlined above are probably less severe. To check further this point, we have computed the formation energy of the unrelaxed oxygen vacancy in model B (Cfr. Table (8.2)) by changing the charge of classical silicon from 2.4 (BKS) to several values in the range 1.6-3.6. The charges of the hydrogen atoms capping the MM cluster and of the boundary quantum oxygen atoms have been scaled accordingly. It turns out that the change in the formation energy of the unrelaxed oxygen vacancy is always smaller than 20 meV.

8.3.3 Molecular dynamics

In order to check the validity of our setup we have performed molecular dynamics simulations of the QM/MM system of size 8/1764 starting from the structure of the defect ($Si_2O_6^*$) optimized with the DZVP basis set. We have first equilibrated the

system at high temperature (1000 K) by velocity rescaling for 0.3 ps. Observables are measured by averaging over a run 10 ps long. The time step used in the velocity Verlet algorithm is 0.5 fs. In Fig.(8.5)a, we report the fluctuation in the potential energy and the total energy, constant of motion, of our microcanonical simulation. The fluctuation in the constant of motion is two order of magnitude smaller than the thermal fluctuations in the potential energy which prove the robustness of our scheme. The Si-Si bond is stable and undergoes stretching deformation with a characteristic frequency that we have identified by Fourier transforming the autocorrelation function $< \dot{\mathbf{R}}(t)\dot{\mathbf{R}}(0) >$ where $\dot{\mathbf{R}}(t)$ is the instantaneous Si-Si bond vector. The correlation function is computed up to 2.5 ps by averaging over three independent sections of a run 10 ps long. The results are well converged up to 0.3 ps. For longer times, a longer simulation run would be needed. The autocorrelation function is therefore windowed with a Fermi-Dirac function which smoothly brings $< \dot{\mathbf{R}}(t)\dot{\mathbf{R}}(0) >$ to zero above 0.25 ps. The resulting power spectrum is shown in Fig.(8.5)b. The peak at $\sim$20.5 THz corresponds to the main stretching mode of The Si-Si bond. Its position in frequency (20.5 THz) compares well with that of the Si-Si stretching mode of the disilane molecule $H_5C_2OSi\text{-}SiOC_2H_5$ we have identified at 21.3 THz from a molecular dynamics simulation 2.2 ps long at 300 K or at 22.4 THz from the diagonalization of the dynamical matrix computed within linear response theory [257] with the code CPMD [171, 258]. The peak at 20.5 THz is also in good agreement with a prominent structure in the vibrational spectra of the Si-Si bond which emerges from the difference in the vibrational density of states, computed fully ab-initio (LDA) in Ref.[259], for two periodic models (36 atoms large) of α-quartz with and without the oxygen vacancy (see Fig.1 of Ref.[259]). The computational load for the molecular dynamics simulation on a single Opteron processor (2.2 GHz) is 28 hours/ps for the small quantum cluster ($Si_2O_6^*$) and 72 hours/ps for the larger cluster ($Si_8O_6O_{24}^*$) both with a classical cluster of 1764 atoms.

8.4 Conclusion

We have presented a QM/MM scheme for silica which is implemented in the general QM/MM framework, presented in this thesis. The capping of the QM region consist of boundary oxygen atoms with a modified charge to enforce total charge neutrality. The quantum cluster in QUICKSTEP is treated at the DFT level by expanding Kohn-Sham orbitals in GTOs and the charge density on an auxiliary plane waves basis set. The combination of the QM/MM method with a localized basis set scheme for the description of the quantum region, allows local structures in silica to be described accurately with small quantum clusters and at a low computational cost. This scheme makes long molecular dynamics simulations, needed for instance to simulate local chemical reactivity, easily affordable. The method has been tested calculating structural and dynamical properties of an oxygen vacancy in α-quartz. We have found that good convergence in the Si-Si bond length and formation energy is achieved by using a quantum cluster as small as eight atoms in size.

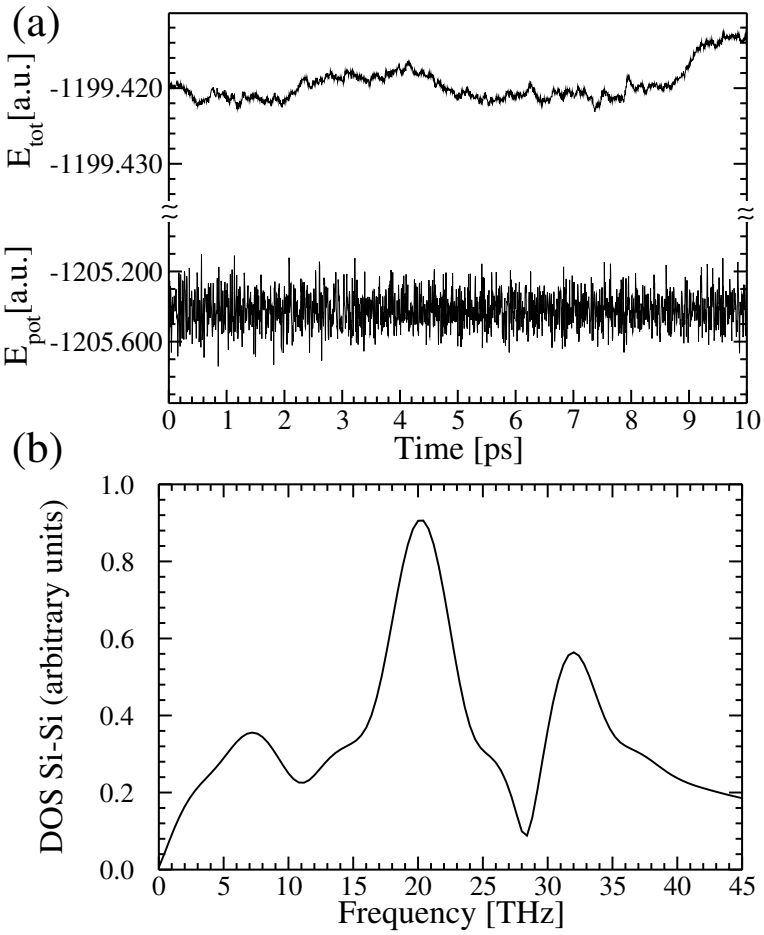

Figure 8.5: Potential energy (E_{pot}) and total energy (E_{tot}) as a function of time in the molecular dynamics simulation. b) The power spectrum of the velocity-velocity autocorrelation function for the Si-Si bond length only (see text).

Chapter 9

Migration of positively charged defects in α-quartz

In this chapter we apply the QM/MM method presented in Chap.(7) and validated in Chap.(8) to model the migration of charged oxygen defects in α-quartz. We simulate the transition mechanism and compute the potential energy surface for the puckering of the symmetric charged oxygen vacancy and the formation of the E_1' center. By overcoming low energy barriers this puckering mechanism can be reiterated allowing the drift of the positive charge localized on an over-coordinated oxygen atom. This process enhances the stability of the E_1' center and can be regarded as an important channel of structural reorganization of oxygen deficient silica in the presence of strong polarizing electric fields.

9.1 Introduction

As we have seen in Sec.(8.1), silicon dioxide is a material of prime importance in microelectronics and fiber optics. Many of the peculiar properties that make silica such an interesting and versatile material are determined by the presence of defects and impurities. Defects strongly affect the performances of silica as a dielectric in transistors, being responsible for current leakage, but they are also held responsible for some phenomena that are positively exploited in optical fibers, such as photosensitivity, which stands behind the writing of photoinduced Bragg gratings [260] and the generation of second-order non-linear response [261] achieved by poling. The underlying microscopic mechanisms of both these phenomena are still mainly unknown, but they are related to structural rearrangements of the SiO_2 network in correspondence of defects. Among the defects that have a remarkable effect on photosensitivity and poling in silica, it was recently pointed out the role of oxygen deficient centers [262]. Neutral oxygen vacancies in silicon dioxide consist of a covalent bond between two silicon atoms. Upon ionization, the Si-Si bond is weakened and the remaining unpaired electron is delocalized between the two silicon atoms [$SiSi^+$]. This configuration is commonly associated with the ESR signal of the E_δ' which is observed in amorphous silica [263, 224]. On the other hand no experimental evidence of this defect has been found in α-quartz so far, which suggests that it is not thermodynamically stable in the crystalline environment as argued in Ref. [264]. In fact, the positively charged oxygen vacancy (OV^+) can undergo an asymmetric relaxation that localizes the unpaired electron on a three-fold coordinated silicon atom and the hole on the other one. The positively charged silicon atom reverts back and forms an elongated electrostatic

bond with a bridging oxygen of the surrounding network, turning into a puckered configuration. This configuration ([Si(3)+O(3)$^+$]) consists of a silicon dangling bond and an over-coordinated oxygen atom and is unanimously related to the ESR signal of the E'_1 center [212, 213, 214, 215, 216, 217, 218]. The correspondent structure in amorphous silica is dubbed E'_γ center.

Given that it is one of the most abundant point defects in silica and its importance in the degradation of the performances of the gate oxide in transistors, the charged oxygen vacancy has been the subject of a large number of calculations [264, 223, 220, 221, 222, 223, 224, 265, 266, 267, 225, 226, 227]. In particular recent studies [220, 264] showed that the positive vacancy is stable only for Fermi levels that lie nearly 3.3 eV above the valence top band of α-quartz. Hence the positive oxygen vacancy in the configuration [Si(3)+O(3)$^+$] can be efficiently created by irradiation followed by a thermal relaxation or with hole injection techniques. Computationally a partial disagreement is found in literature as for the relative energies of the two defect configurations. Blöchl [220] shows that the [SiSi$^+$] and the [Si(3)+O(3)$^+$] defects are nearly isoenergetic, with the [Si(3)+O(3)$^+$] more stable by 0.04 eV, while Boero *et al.*[223] predicted [Si(3)+O(3)$^+$] to be more stable by 0.3 eV. This partial disagreement has been justified with the use of different exchange-correlation functionals in the DFT calculations, in particular Boero et al.[223] used a local density approximation (LDA) [268] as opposed to Blöchl using a gradient-corrected functionals [124]. The Barrier of the conversion E'_δ - E'_1 has been calculated [220] to be 0.38 eV, in agreement with Boero et al.[223]. Other quantum chemical studies [224] predict [Si(3)+O(3)$^+$] to be more stable by 0.64 eV with a barrier between the two defects of 0.38 eV. Unfortunately the structures of these cluster calculations differ sizably from the DFT based calculations [223, 220] possibly due to the use of Hartree-Fock for computing optimized geometries. As this defect is known to generate an important strain field in the silica matrix [230, 229, 269] we argue that the way the boundary conditions are treated can be another very important source of discrepancies in the calculation of the energetics.

From the barrier of 0.38 eV for the transition between [SiSi$^+$] and [Si(3)+O(3)$^+$], one would expect to see both configurations in about equal concentrations, whereas in isochronal annealing studies, performed on amorphous silica, the E'_γ center apparently anneals at much higher temperature than E'_δ [263]. Thus there is still an open issue related to the apparent higher stability of the E'_γ center compared to the E'_δ. Blöchl [220] suggested that the concentration measured in isochronal annealing experiments does not only reflect thermal stability, but also a possible charge transfer process that makes the defect ESR invisible. The arguments used to validate this speculation are mainly based on relative stability of the electronic levels between the oxygen charge and neutral vacancy defects. In fact, the charging level of E'_δ lies 1.38 eV below the silicon mid-gap, where it can capture electrons from other filled defect states or the contacts while the charging level of E'_γ lies 0.68 eV above it.

Starting from an ionized OV, and relying on the validation of the QM/MM method presented in this thesis (see Chap.(7) and Chap.(6)), we compute the migration path and the potential energy barrier for the puckering and formation of an E'_1 (known as E'_γ in amorphous silica) center and a three-fold coordinated oxygen atom. The QM/MM approach employed here allows for an accurate description of the defect-induced strain field in the crystal, which provides a better estimate of the energetics

of the defects configurations with respect to previous published results[223, 220].

Here we propose an alternative mechanism, based on the migration of the three-fold coordinated oxygen atom through the quartz pattern, that concurs to stabilizing the E_1' over the E_δ'. On the basis of our computational evidences, we propose that once the E_1' center is formed, it can easily access a large number of states, we will call $E_1^\star$, ESR similar to the E_1', characterized by a migration of the three-fold oxygen defect through the crystal. Moreover we propose for the first time a process of structural rearrangement in silica associated to a directional charge migration, which does not involve the existence of ionic impurities. Since this process is accompanied by the drift of the positive hole, we suggest that the puckering mechanism can be substantially enhanced by the application of an external electric field, resulting in a migration of the positive charge assisted by the migration of the three-fold coordinated oxygen atom. These concepts can be extended to amorphous system except for directionality which is peculiar of the quartz crystal. Although the study of the amorphous system would be technologically more relevant, it would have required a statistical analysis, which is unaffordable to present day computer resources. We have therefore chosen to study defect transformations in α-quartz which saves us from sampling over a large amount of different sites.

9.2 Methods

We have performed QM/MM geometry optimizations, molecular dynamics and optimization of reaction path to describe quantitatively the energetics along the coordinate linking the E_δ', E_1' and $E_1^\star$. The calculations presented are based on results presented in Chap.(7) and Chap.(6). A DFT [86, 87] level of theory with local spin density (LSD) approximation to treat the open shell system is used for the description of the quantum region. The exchange-correlation functional employed in the overall calculation is PBE [270, 124] and a cutoff of 250 Ry is used for the expansion of the QM electronic density. The classical force field used to describe the MM system subsystem is the van Beest, Kramer, van Santen (BKS) potential [41] already extensively tested for QM/MM simulations of α-quartz (see Chap.(8)). All calculations have been performed with the CP2K package. The wave function optimization is performed by the QUICKSTEP algorithm [85] using a dual basis set (BS): a Gaussian BS to construct the Hamiltonian core matrix and a plane wave BS to evaluate the exchange-correlation and Hartree potential.

The MM quartz crystal made of 5184 SiO_2 units (15552 atoms) in an orthorombic cell with lattice constants of 49.94, 57.66 and 63.49 Å is optimized using the BKS pair potential[41] which provides a reliable description of bulk α-quartz. After removal of an oxygen atom, a portion of 159 atoms was chosen in order to surround the OV defect and to suitably describe the motion of the defect through the crystal Fig.(9.1). The oxygen boundary atoms is described with a core charge increased by 0.4 e in order to maintain the neutrality of the overall system. The link between the QM and the MM region is the performed through the use of modified pseudo potential as already described and extensively tested in Sec.(8.2).

The QM/MM potential is efficiently computed exploiting the Gaussian expansion of the electrostatic potential (GEEP) scheme (see Sec.(6.2.1)). The long range electrostatic term in the QM/MM coupling scheme is essential to treat properly the quantum properties of the QM subsystem in ordered structures like α-quartz. The inclusion of

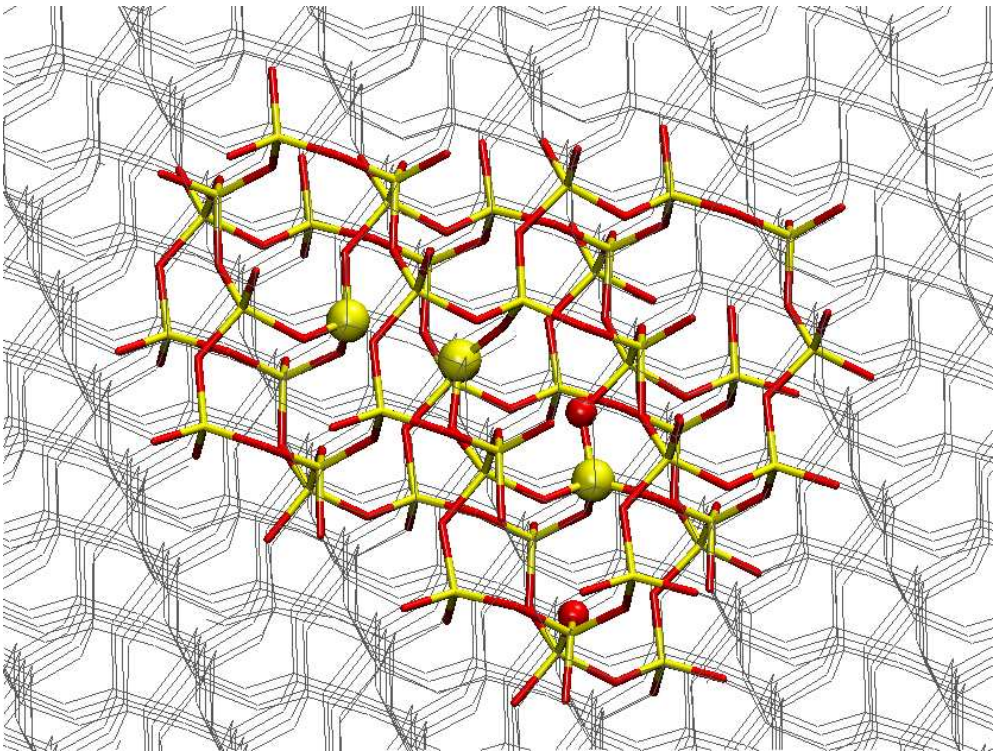

Figure 9.1: Structure of the QM fragment embedded in the MM crystal. Atoms involved into the migration of the charged OV are depicted with bigger dots

the periodic boundary conditions in the evaluation of the SCF perturbing MM external potential is achieved introducing a reciprocal space term of the MM electrostatic potential through a modified Ewald scheme (see Chap.(7)). Moreover the QM subsystem is coupled itself to its periodic replicas as explained in Sec.(7.2.3). QM/MM geometry optimizations have been performed on the three local minima identified with the defects E'_δ, E'_1 and $E^\star_1$ Fig.(9.2). Once defined the structure of the three local minima, we have performed a full mapping of the energetics of the reaction path going from E'_δ to $E^\star_1$ passing through E'_1. The reaction path has been computed with a nudged elastic band calculation [271, 272, 273] using the module implemented into the CP2K code. The optimization of the band has been performed by a coupled steepest descent/DIIS procedure with a tolerance of 0.001 a.u. on gradients.

9.3 Results and discussion

9.3.1 Equilibrium Geometries

Performing geometry optimization of a neutral OV, created by removing an oxygen atom from a QM fragment of the fully optimized MM crystal,a covalent bond is formed between the two silicon atoms with a length of 2.34 Å. When an electron is removed from the system this covalent bond is weakened and the distance between the two silicon atoms increases to 2.85 Å. We have verified that this structural conformation

Fig.(9.3-a), identified with the (E'_δ) center, is stable in a MD run of 5.0 ps long at room temperature (398K).

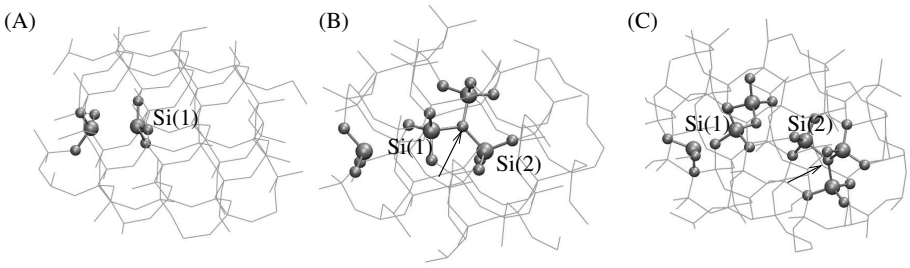

Figure 9.2: Locally stable structures of the positively charged oxygen vacancy: the symmetric charged OV (E'_δ)(panel A), the puckered configuration (E'_1) with the positive charged localized on the three-fold coordinated oxygen (B) and the configuration obtained after the migration of the three-fold coordinated oxygen ($E^\star_1$)(C). Large spheres represent silicon atoms while smaller ones are oxygen atoms. The arrows indicate the three-fold coordinated oxygens in panels (B) and (C).

Another locally stable structure is obtained by puckering one of the silicon atoms[223, 220] Fig.(9.3-a) and Fig.(9.3-b). In qualitative agreement with Ref.[223, 220], we find that this configuration, identified as the E'_1 center, is more stable than the initial [$SiSi^+$] conformation, being the relative total energy difference 0.18 eV. The quantitative disagreement in this stabilization energy with respect to previously published data (0.04 eV [220] and 0.30 eV in [223]) may be due to different reasons. As in [220] we performed all calculations using a gradient-corrected exchange-functional, while Boero et al. [223] were using plain LDA. Another source of difference may be represented by the open shell DFT treatment, however in previous works it was shown that geometries and energies of the E'_γ center in amorphous silica do not change switching from LDA to LSD [274]. The largest source of discrepancy between our work and the previous ones is certainly that the QM/MM scheme allows large systems to be simulated, thus providing a more realistic treatment of the defect induced strain field, which can extend for up to five coordination shells in the case of oxygen deficiency centers [230, 229]. In addition, the system size used in [223] and [220] is also too small to avoid a strong interaction between the charged periodic replica, while in our case the QM charged system interacts with a periodicity that is the one of the full MM crystal ($\approx$ 60 Å against $\approx$ 10 Å) and the periodic interaction is screened by the presence of the MM charge distribution. Interestingly, while performing geometry optimization of the puckered configuration we found two isoenergetic local minima (see Fig.(9.3-b) and Fig.(9.3-c)), differing slightly in the coordination distances of the three-fold oxygen atom. In particular the distance of this oxygen from the puckered Silicon can change of 0.1 Å from one minima to the other. In this latter configuration two of the three distances Si-O around the three-folded oxygen atom are almost equivalent, while the third is constantly 0.1 Å smaller.

Figure 9.3: These frames show the relevant bond distances for the several optimized geometry structures at QM/MM level. For clarity reason only atoms involved in the migration of the OV defects are shown. Frame Fig.(9.3-a) shows the E'_δ, obtained relaxing the OV after charging the defect. Frame Fig.(9.3-b) and Fig.(9.3-c) show two local isoenergetic minima of the E'_1 defect. the two structures differ of few picometers in the bond distances around the three-fold oxygen atoms. The last frame Fig.(9.3-d) shows the migrated defect, called in this work $E^\star_1$.

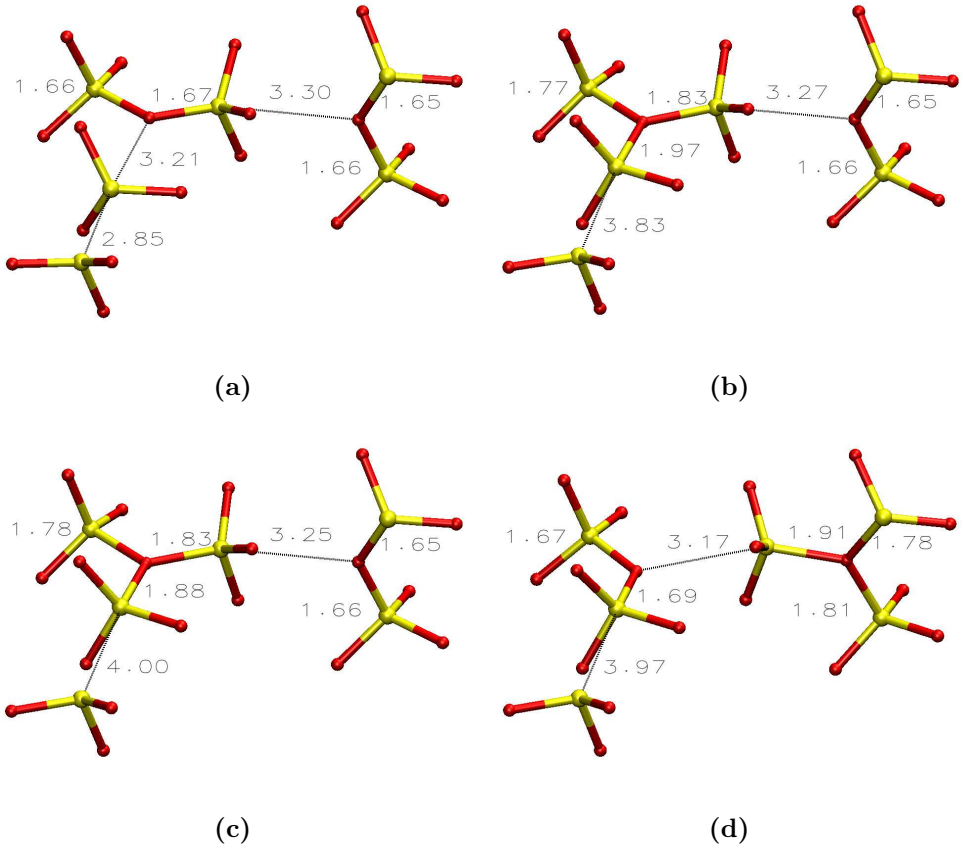

The equivalence between these two bonds suggest that the puckering mechanism can be iterated. By breaking a pre-existing Si-O bond around the over-coordinated oxygen the dangling bond of the silicon atom reverts back and binds to another bridging oxygen which becomes 3-fold coordinated Fig.(9.3-d), what we call in this thesis $E^\star_1$. This transformation is accompanied by the migration of the positive charge that moves farther apart from the paramagnetic silicon center as it gets localized on the newly formed 3-fold coordinated oxygen atom.

Also for this structure, here labeled $E^\star_1$, we highlight the presence of two longest bonds around the new three-fold oxygen atom involving the recently puckered Silicon and the Silicon atom having the right geometrical characteristic to perform a new

puckering motion. The $E_1^\star$ Fig.(9.3-d) is less stable than the original E_1' by 0.41 eV, but as the process can be iterated until another point defect is found, there is a large number of such configurations available, which are indistinguishable from the pristine E_1' defect [1]. This makes the ensemble of these metastable states relevant to the kinetics and thermodynamics of defects in α-quartz and possibly in amorphous silica, in spite of the higher formation energy. For example if we have a concentration of E′ centers of $10^{15}/cm^3$, there are $\sim 10^6$ available migration sites, with a relative chance of being populated with respect to the E_δ' equal to $P(E_1^\star)/P(E_\delta') = e^{-\Delta E/kT}$ each. Given the energetics reported above, at room temperature this ratio is 10^{-3}, which multiplied by the number of available $E_1^\star$ sites, gives a relative population of the $E_1^\star$ 10^3 times larger than the E_δ' and similar to the E_1' . Increasing the temperature or reducing the defect concentration moves this balance even more on the side of the $E_1^\star$. The migration path is predetermined to be helical on the basis of quartz chirality, since only 2 out of the 3 silicon atoms coordinating the oxygen atom have a neighboring oxygen atom at ≈ 3.0 Å on which the puckering leads to a metastable structure.

9.3.2 Migration path energy profile

Using the above mentioned optimized structures we have performed a nudged elastic band (NEB) [271, 272, 273] optimization of the transition path to describe the energetics of the migration of the defect from E_δ' to $E_1^\star$ through E_1'. The calculation has been performed using the NEB module as implemented in CP2K , interpolating 16 more images between the 4 optimized geometries, in order to have all images roughly at the same distance. A spring constant of 0.03 a.u. was used to describe the spring force between replicas together with the IT-NEB [273] algorithm to avoid the formation of kinks. A coupled steepest descent/DIIS optimization has been used to optimize the band. The 20 replicas used to describe the full migration path were computed using 64 processors per replica (1280 processors in total) and the optimization procedure required 188 optimization steps to achieve the convergence criteria on gradients (0.001 a.u.). The full band optimization required 200K cpu hours to be completed.

The optimized energy profile is shown in Fig.(9.4) and it clearly shows that defects E_δ' and E_1' are separated by a barrier of 0.14 eV, value smaller than the one reported by [223, 220] of 0.38 eV. Same considerations done for the optimized energies holds for the quantitative disagreement between this work and the previous ones [223, 220] regarding transition state energies. Moreover defects E_1' and $E_1^\star$ are separated by a barrier of 0.59 eV, that can be relatively easily overcome even at room temperature. The barriers between $E_1^\star$ states are expected to be even lower, so that the puckering mechanism can continue along the crystal pattern.

[1] We argue that the $E_1^\star$ structure cannot be distinguished from the E_1' by ESR, as the influence a positive charge at more than 4-5 Å on the spin localization on the three fold coordinated silicon atom is negligible.

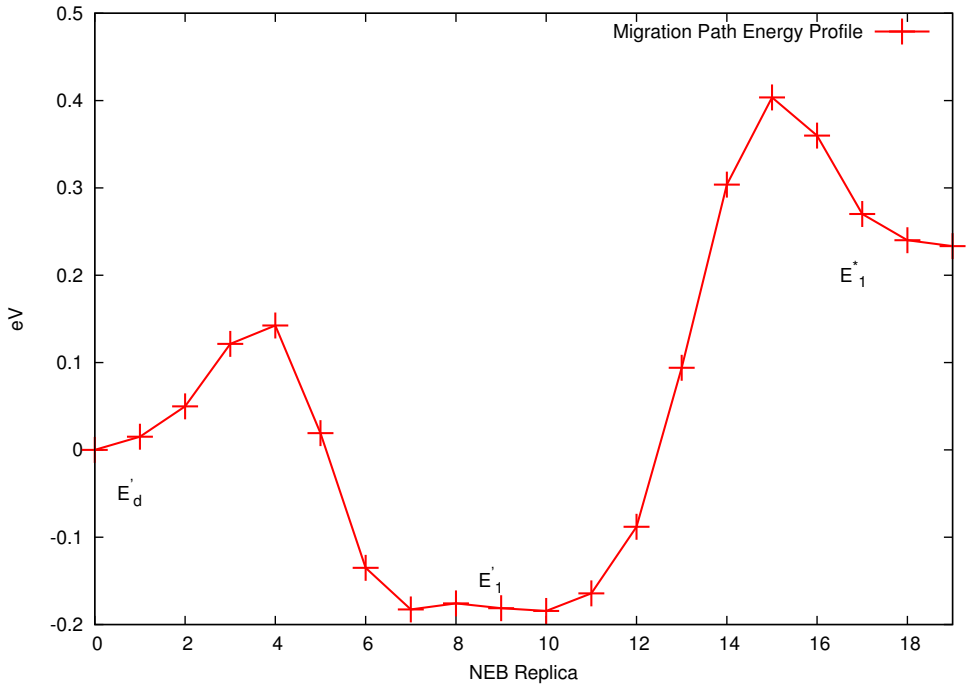

Figure 9.4: Optimized energy path from E'_δ to $E^\star_1$ through E'_1.

9.3.3 Charge analysis and energy levels

The charged oxygen deficient centers studied all over this chapter are open-shell systems. In order to validate the results obtained we checked that the self-interaction error [268, 275] in this system was not a vitiating source of error. Indeed the analysis of the spin-density shows that it is very localized around the under-coordinate silicon atom. This confined spin-density reflects in a negligible error due to the interaction of the electron with itself.

It's interesting to note that the migration of the three-fold coordinated oxygen is tightly couple to the migration of the positive charge. The population analysis is a by-product of the coupling/decoupling scheme. In fact the charged used to restore the proper periodicity for the QM system [210] (see also App.(C)) reproduce correctly the amount of charge present on each atom [210]. A Löwdin population analysis was performed for comparison and results for both methodologies were quite in good agreement. In the defect E'_δ the positive charge is delocalized between the two silicon atoms. After the first puckering the positive charge is mainly localized over the three-fold oxygen atom (+0.49 e) with a small delocalization over the Silicon atoms surrounding the oxygen (+0.17 e), while the unpaired electron is located on the under-coordinated silicon atom. The same behavior is observed for the defect $E^\star_1$, the positive charge being totally localized around the three folded oxygen atom, with a main localization over the oxygen itself (+0.64 e). An interesting aspect is also provided by the energy level of the unpaired electron.

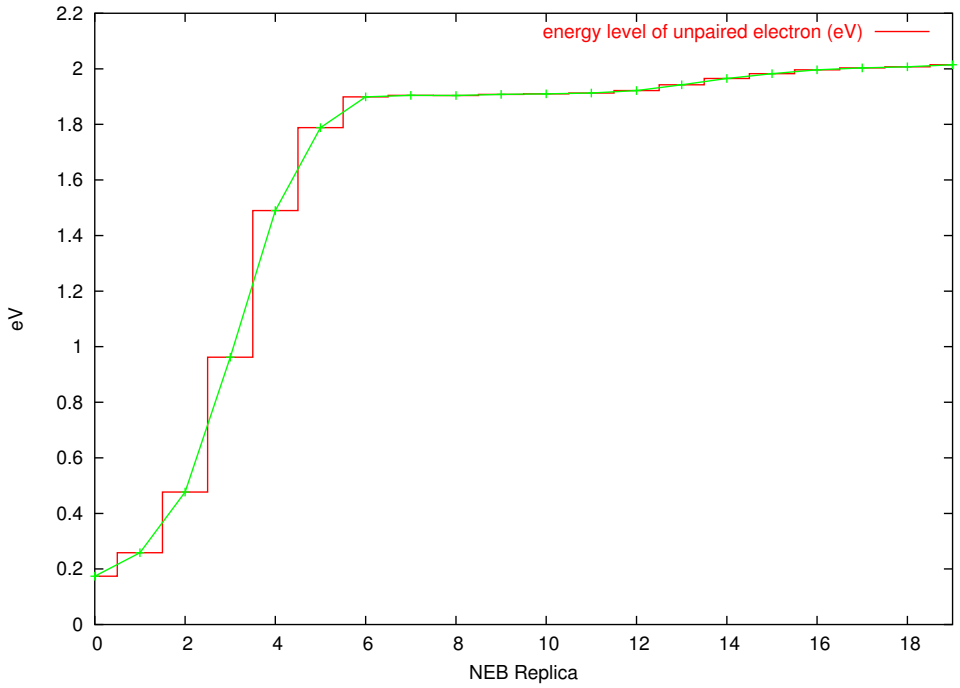

Figure 9.5: This picture shows the energy levels of the unpaired electron along the optimized path from E'_δ to $E^\star_1$ through E'_1.

In Fig.(9.6) we have shown the density of states (DOS) for the three configurations, providing different DOS for α and β spin. The DOS was obtained averaging the states levels during 5 ps of MD simulation at 398K (all configurations were stable during a microcanonical MD at 398K for the simulated time of 5 ps). It is unmistakable from this picture that the energy level of the defect rises going from E'_δ to E'_1 and then $E^\star_1$ (see Fig.(9.6-a), Fig.(9.6-c) and Fig.(9.6-e)). Going into details, in Fig.(9.5) we show the energy level of the defect along the optimized migration path, the zero being the energy level of an electron in the top valence band. As we can see the energy level increases along the migration $E'_\delta \rightarrow E^\star_1$. The energy level of E'_1 is higher of 1.95 eV with respect to E'_δ and roughly equivalent (0.1 eV smaller) than $E^\star_1$. Both qualitative and quantitative picture of the energy levels totally agree with previously reported calculations [220].

9.4 Conclusions

In this chapter we studies the migration path of oxygen charged defects in α-quartz. On the basis of transition state energies and equilibrium stability we conjecture that the well known process going from defect E'_δ to E'_1 can take place in an iterative way along the crystal path leading to a charge migration far from the OV site, providing an alternative explanation to available controversial experimental data [263]. In

fact, the low potential energy barriers computed for both processes (<0.6eV) suggest that the positive charge can easily migrate during the thermal annealing and several equivalent states can be populated providing the same E_1' ESR signal. After annealing only configurations where the paramagnetic center and the 3-fold coordinated oxygen are close to one another can easily recombine to the energetically more favored E_δ' structure, while if the positive charge migrates farther apart recombination will be unlikely to happen. Therefore our result provides a convincing explanation for the apparent higher stability of the E_1' center. In the presence of an external electric field, as in the case of poling, this mechanism would be enhanced, providing a viable path to a permanent structural modification associated to the drift of positive charges.

Figure 9.6: These frames show the density of states, divided between spin α and β, of the three configurations: E'_δ, E'_1 and $E^\star_1$. In particular the comparison between frames Fig.(9.6-a), Fig.(9.6-c) and Fig.(9.6-e), shows that the energy level of the defect increases in energy going from E'_δ to E'_1 and $E^\star_1$. The Energy level of the defect is not identifiable for E'_δ (see Fig.(9.6-a) and Fig.(9.6-b)) while for E'_1 and $E^\star_1$ it can easily identified at 0.09-0.1 Hartree from the top valence band (see Fig.(9.6-c) and Fig.(9.6-e)). For completeness also the density of states of the spin β have been provided.

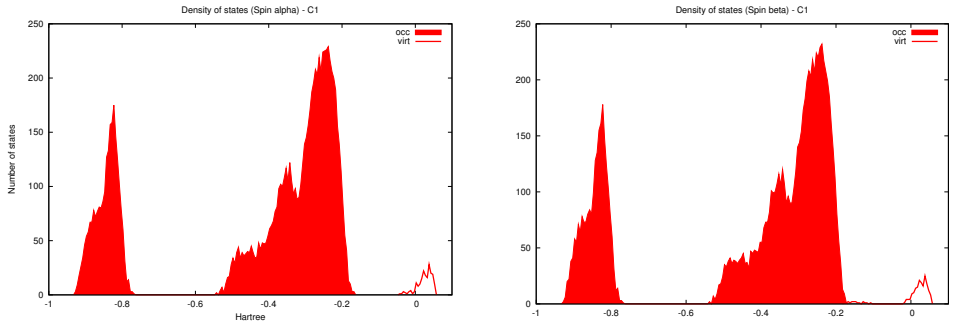

(a)

(b)

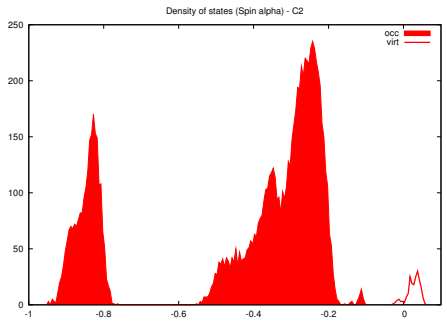

(c)

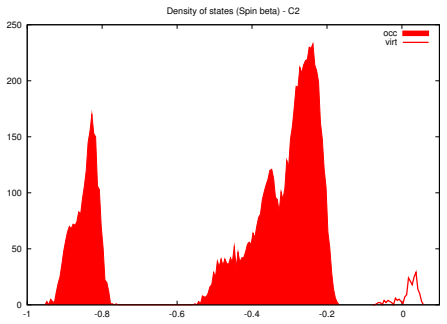

(d)

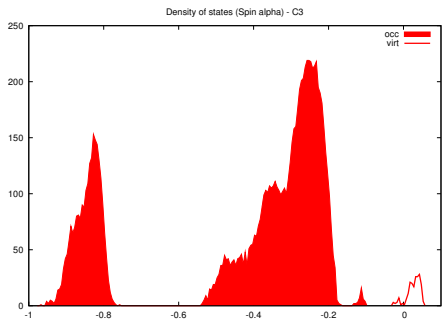

(e)

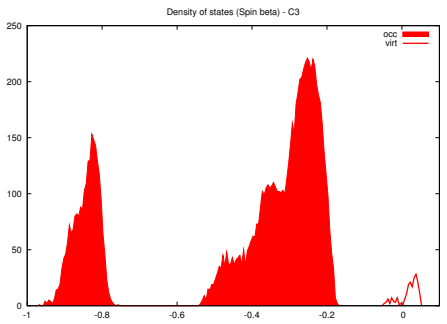

(f)

Chapter 10

Conclusions

The QM/MM studies performed in the last 30 years demonstrated the importance of the protein environment for a correct theoretical description of an enzymatic reaction. At the same time they permitted to increase the length scale of the simulation to examine long-range strain around a defect or crack in a solid or a crystal.

Combining QM and MM methods by applying them to separate subsystems with a boundary in physical space is nowadays very natural, and it is safe to say that it is now a permanent part of the theoretical toolbox. However, there is still ample space for developing more accurate, robust, cost-effective and easy-to-use implementations.

In this thesis we presented an algorithm named GEEP (Gaussian Expansion of the Electrostatic Potential, see Sec.(6.2.1)) used to evaluate the QM/MM electrostatic coupling term with a fast linear scaling implementation. The main result is the dropping of the prefactor in the linear scaling, with a gain in the number of floating point operations proportional to $2^{3(N_{grid}-1)}$, where N_{grid} is the number of grid levels used in the multi-grid framework. The cost of the evaluation of the electrostatic potential on a grid is proportional to the number of MM atoms times the number of grid points. In real systems the linear scaling evaluation of the potential is therefore characterised by a prefactor $\approx 10^6$. In this scheme the prefactor is instead rarely larger than $\approx 10^3$. The number of floating point operations is reduced by several orders of magnitude and the computational time is 10-100 times smaller.

Furthermore, we extended the GEEP algorithm in order to describe fully periodic potentials (see Chap.(7)), leading to a proper treatment of the QM/MM electrostatic coupling in condensed matter systems (crystals). This extension is designed in order to include the effects of periodic boundary conditions into hybrid QM/MM descriptions without the use of spherical truncation schemes in treating the electrostatics. The periodic boundary conditions scheme preserves the linear-scaling property of the GEEP technique and is computationally efficient, leading to no additional overhead with respect to the evaluation of the QM/MM electrostatic potential with a truncation scheme using a spherical cutoff. Preliminary tests showed that the use of periodic boundary conditions together with a proper treatment of the long-range interactions is required for ordered systems, unless a careful truncation scheme with a preliminary optimisation of the shape and dipole of the MM environment is used.

All the presented algorithms have been implemented into the freely available CP2K package [84].

Finally a validation of a QM/MM approach for silica-based system has been presented (see Chap.(8)). We tested the QM/MM approach on small SiO_2 clusters in

order to probe the quantum description, the classical potential and the QM/MM interaction between the two subsystems. Relying on this validation scheme we investigated the migration of E_1' defects in SiO_2 (see Chap.(9)), providing a new interpretation to ambiguous experimental data. Between the charged oxygen vacancy defects two of them were object of our studies E_δ' and E_1', experimentally known to be connected through a very small barrier ($\approx 0.2eV$), easily overcome at room temperature. Hence one would expect to see both configurations in approximately equal concentrations, whereas in isochronal annealing studies the E_1' center apparently anneals at much higher temperature than E_δ'. One proposed explanation to this dilemma takes into account the easiest possibility of the E_δ' center to be discharged and consequently to disappear due to their conversion into neutral oxygen vacancy.

In this thesis we propose a different interpretation. Performing QM/MM simulations we show that at room temperature a feasible dynamical channel exist for the depletion of E_δ' defects, consisting in a migration of the E_1' center. The computed barriers for this migration process are $\approx 0.60eV$ consistently with the physical phenomena observed at room temperature.

Approximately 200.000 cpu hours have been dedicated to the computation of the potential energy profile of the migration path. Beside this, a lot of human efforts has been invested in optimising algorithm and improving them, relying constantly on the idea of free software: sharing knowledge with people that either modify or use what you make available to the scientific community. Ideally, the results obtained in this thesis will be interesting, engaging, and who knows maybe life changing for few!

Part V

Appendices

Appendix A

Gaussian Distributions

A.1 Gaussian product rule

Gaussian product rule is probably the most important tool in computational chemistry and physics. It can be expressed in the following way:

$$\exp^{-a(x-x_a)^2} \cdot \exp^{-b(x-x_b)^2} = \exp^{-\frac{ab}{a+b}(x_a-x_b)^2} \cdot \exp^{-(a+b)[x-\frac{ax_a+bx_b}{a+b}]^2} \tag{A.1}$$

A.2 Coulomb Interaction Integrals

Computational chemistry and computational physics applied to molecules have a common big challenge: a fast computation of coulomb integrals (both in a plane wave formalism and in a localized basis framework, all integrals (1- and 2- electrons integrals) can be reduced to a coulomb interaction integral).

Coulomb integrals cannot be expressed in a close analytical form. Usually, error function or a Boys function is used to represent them. The Coulomb integrals represent the interaction between two charge distributions ρ_p:

$$V_{pq} = \int\int d^3r d^3r' \ \frac{\rho_p(\vec{\mathbf{r}})\rho_q(\vec{\mathbf{r}}')}{|\vec{\mathbf{r}} - \vec{\mathbf{r}}'|} \tag{A.2}$$

We are interested in the computation of the Coulomb terms with a Gaussian type charge distribution

$$\rho_p = \frac{Z_p}{(R_p^c)^3}\pi^{-\frac{3}{2}} \exp\left[-\left(\frac{|\vec{\mathbf{r}} - \vec{\mathbf{R}}_p|}{R_p^c}\right)^2\right] \tag{A.3}$$

Once you know how to compute V_{pq} you can construct nuclear-nuclear repulsion integrals, nuclear-electron attraction integrals (by setting one charge distribution to a point charge and the other one to a certain Z value, taking care of the shielding effect of the inner core electrons, whenever pseudo-potentials are used). We use the following representation of the r_{12}^{-1} operator:

$$\frac{1}{r_1 - r_2} = \frac{1}{\sqrt{\pi}} \int_{-\infty}^{+\infty} \exp^{-[\vec{\mathbf{r}}_1 - \vec{\mathbf{r}}_2]^2 t^2} \, dt \tag{A.4}$$

This is used to compute the potential at point $\vec{\mathbf{r}}_c$ generated by charge distribution $\rho_p(\vec{\mathbf{r}})$

$$V_p(\vec{\mathbf{r}}_c) = \int d^3r \; \frac{\rho_p(\vec{\mathbf{r}})}{|\vec{\mathbf{r}} - \vec{\mathbf{r}}_c|} \tag{A.5}$$

Using the Gaussian product rule and setting for shortness

$$C_p = -Z_p \left(\frac{\beta_p}{\pi}\right)^{\frac{3}{2}}, \tag{A.6}$$

$$\beta_p = \frac{1}{(R_p^c)^2} \tag{A.7}$$

it is easy to show that

$$\begin{aligned} V_p(\vec{\mathbf{R}}) &= \int d\vec{\mathbf{r}} \int_{-\infty}^{+\infty} dt \left\{ \frac{C_p}{\sqrt{\pi}} \exp^{\left(-(\beta_p+t^2)(r-R_0)^2 - \frac{\beta_p t^2}{\beta_p+t^2}(\vec{\mathbf{R}}-\vec{\mathbf{r}}_p)^2\right)} \right\} \\ &= \frac{C_p}{\sqrt{\pi}} \int_{-\infty}^{+\infty} \left(\frac{\pi}{\beta_p + t^2}\right)^{\frac{3}{2}} \exp^{\left(-\beta_p(\vec{\mathbf{R}}-\vec{\mathbf{r}})^2 \frac{t^2}{\beta_p+t^2}\right)} dt \\ &= \frac{2C_p}{\sqrt{\pi}} \int_{0}^{+\infty} \left(\frac{\pi}{\beta_p + t^2}\right)^{\frac{3}{2}} \exp^{\left(-\beta_p(\vec{\mathbf{R}}-\vec{\mathbf{r}})^2 \frac{t^2}{\beta_p+t^2}\right)} dt \end{aligned} \tag{A.8}$$

where $\vec{\mathbf{R}}_0 = \frac{\beta_p \vec{\mathbf{r}}_p + t^2 \vec{\mathbf{R}}}{\beta_p + t^2}$. This remaining integral can be solved by applying the substitution

$$u^2 = \frac{t^2}{\beta_p + t^2}, \qquad dt = \frac{\beta_p}{(1-u^2)^{\frac{3}{2}}} du \tag{A.9}$$

The integration limits change in $t = 0 \rightarrow u = 0$, $t = \infty \rightarrow u = 1$. With these modifications we get

$$\begin{aligned} V_p \vec{\mathbf{R}} &= \frac{2C_p\pi}{\beta_p} \int_0^1 \exp^{-\beta_p(\vec{\mathbf{R}}-\vec{\mathbf{r}}_p)^2 u^2} \, du \\ &= \frac{2C_p\pi}{\beta_p} F_0(\beta_p(\vec{\mathbf{R}} - \vec{\mathbf{r}}_p)^2) \end{aligned} \tag{A.10}$$

where F_0 is the Boys function of the first order [276] [277].
The last equation can be expressed with the help of the error function:

$$F_0(x) = \sqrt{\frac{\pi}{4x}} \mathrm{Erf}(\sqrt{x}) \tag{A.11}$$

$$\mathrm{Erf}(x) = \int_0^x \exp^{-t^2} dt \tag{A.12}$$

Once we have the potential $V_p(\vec{\mathbf{r}})$, we can compute the actual interaction matrix element V_{pq} from the integral

$$V_{pq} = \int V_p(\vec{\mathbf{r}})\rho_q(\vec{\mathbf{r}})d\vec{\mathbf{r}}$$
$$= 2Z_pZ_q\sqrt{\frac{\beta_p}{\pi}}\left(\frac{\beta_p}{\pi}\right)^{\frac{3}{2}}\int d\vec{\mathbf{r}}\int_0^1 dt\exp^{-\beta_p(\vec{\mathbf{r}}-\vec{\mathbf{r}}_p)^2t^2}\exp^{-\beta_q(\vec{\mathbf{r}}-\vec{\mathbf{r}}_q)^2} \tag{A.13}$$

Using the GPR to get a form appropriate for integration over all space:

$$V_{pq} = 2Z_pZ_q\sqrt{\beta_p\pi}\left(\frac{\beta_p}{\pi}\right)^{\frac{3}{2}}\int d\vec{\mathbf{r}}\int_0^1 dt\exp^{-\frac{\beta_q\beta_pt^2}{\beta_q+\beta_pt^2}(\vec{\mathbf{r}}_p-\vec{\mathbf{r}}_q)^2}\exp^{-(\beta_pt^2+\beta_q)(\vec{\mathbf{r}}-\vec{\mathbf{R}}_0)^2} \tag{A.14}$$

Integration over space gives

$$V_{pq} = Z_pZ_q\frac{2\beta_p^{\frac{1}{2}}\beta_q^{\frac{3}{2}}}{\pi^2}\int_0^1 dt\exp^{-\frac{\beta_q\beta_pt^2}{\beta_q+\beta_pt^2}(\vec{\mathbf{r}}_p-\vec{\mathbf{r}}_q)^2}\left(\frac{\pi}{\beta_q+\beta_pt^2}\right)^{\frac{3}{2}} \tag{A.15}$$

Trying the following substitution, similar to the one used previously but with a small hint to shorten the transformation

$$u^2 = t^2\frac{\beta_q+\beta_q}{\beta_q+\beta_qt^2}, \qquad dt = \frac{(\beta_q+\beta_q)\beta_q}{[\beta_q+\beta_p(1-u^2)]^{\frac{3}{2}}}du \tag{A.16}$$

One obtains after applying this substitution, the interaction energy of two charge clouds distribution, as a function of the relative mean point distribution $\vec{\mathbf{r}}_q$ and $\vec{\mathbf{r}}_p$

$$V_{pq} = Z_pZ_q\frac{2}{\sqrt{\pi}}\sqrt{\beta_{pq}}\exp^{-\beta_{pq}(\vec{\mathbf{r}}_p-\vec{\mathbf{r}}_q)^2}, \qquad \beta_{pq} = \frac{\beta_p\beta_q}{\beta_p+\beta_q} = \frac{1}{(R_q^c)^2+(R_p^c)^2} \tag{A.17}$$

A slightly simpler form is obtained where error function is used

$$V_{pq} = Z_pZ_q\frac{1}{|\vec{\mathbf{r}}_p-\vec{\mathbf{r}}_q|}\mathrm{Erf}\left(\sqrt{\beta_{pq}}|\vec{\mathbf{r}}_p-\vec{\mathbf{r}}_q|\right) \tag{A.18}$$

Observe that

$$\lim_{r_{pq}\to 0}V_{pq} = 2Z_pZ_q\sqrt{\frac{\beta_{pq}}{\pi}} \tag{A.19}$$

Appendix B

Efficient mapping of product Gaussian on the real space grid

The transformation of the atomic orbital based density matrix to an electron density on a real space grid, and the complementary operation, i.e. the computation of matrix elements given a potential on a real space grid are important operations in the GPW method. This step needs to be performed at every SCF cycle, and might contribute significantly to the overall execution time of the algorithm. However, a Gaussian basis set allows for techniques that reduce the cost of this operation significantly if regular orthogonal grids are employed. The described algorithm has a computational cost for computing integrals involving Cartesian Gaussian that scales effectively linearly in the l quantum number.

A first step in the algorithm is the transformation of the atomic orbital basis into primitive Cartesian Gaussian

$$g_{\eta l^x l^y l^z}(r) = x^{l^x} \exp(-\eta x^2) y^{l^y} \exp(-\eta y^2) z^{l^z} \exp(-\eta z^2). \tag{B.1}$$

The product of two primitive Gaussian $g_{\eta_a l_a^x l_a^y l_a^z}(r-A)$ and $g_{\eta_b l_b^x l_b^y l_b^z}(r-B)$ is a Cartesian factor multiplied by a single Gaussian with center

$$P = \frac{\eta_a A + \eta_b B}{\eta_a + \eta_b}, \tag{B.2}$$

exponent $\eta_p = \eta_a + \eta_b$, and prefactor

$$\exp(-\frac{\eta_a \eta_b}{\eta_a + \eta_b} |A - B|^2). \tag{B.3}$$

Based on this exponent, the total l quantum number, and the prefactor, the radius R of a sphere around P is computed where the Gaussian product is non-negligible to within some threshold, typically $10^{-10} - 10^{-14}$. Only grid points within this sphere are used in the integration and mapping.

The product can be factorized in three parts that each depend only on a single variable x, y or z. Each part can be precomputed on a 1d grid, the full value of the Gaussian product on any point of the 3d grid is a product of 3 precomputed numbers. In particular, the inner loop on the grid (e.g. x component) will just be a single multiplication of a constant (depending on y and z) with number stored in a 1d array (independent of y and z). Furthermore, all products that have the same

center, independent of the l quantum number, can be computed simultaneously by expanding for each term the factors $(x-A)^{l_a^x}(x-B)^{l_b^x}$ and summing the prefactors of identical terms. The inner loop contains in that case just $l_a^x + l_b^x + 1$ terms, each one can be precomputed as described above. Therefore $O(l_a^3 l_b^3)$ terms are computed in approximately $O(l_a + l_b)$ time, contributing greatly to the efficiency of the algorithm. In particular, basis sets involving high angular momentum are relatively inexpensive, even if derivatives for e.g. the kinetic energy density or the forces are required.

As described previously [208], multi grids, i.e. grids with different mesh sizes, are employed to compute matrix elements and densities.

In the multi grid method, the exponent η_p of the Gaussian product is used to select a grid so that the number of grid points per $\sigma_p^2 = 1/2\eta_p$ is approximately independent of η_p. The accuracy of the multi grid method is fixed specifying a single number (number of grid points per σ_p) which is conveniently expressed as the plane wave cutoff of the grid used for Gaussian with $\eta_p = 1$. We employ 30 Ry as a default relative cutoff as this is both efficient and accurate. Furthermore, it is not necessary to have multi grids for each exponent, and in our experience it is sufficient to have N grids with

$$E_{\mathrm{cut}}^i = \frac{E_{\mathrm{cut}}^1}{\alpha^{(i-1)}} \qquad \text{i=1..N} \tag{B.4}$$

where $\alpha = 3.0$. The necessary N and E_{cut}^1 depend on the smallest and largest exponents of the Gaussian basis set used, but are typically four and 280 Ry respectively.

Appendix C

Construction of the model charge density

The model density $\hat{\rho}(\mathbf{r}, \mathbf{r}_\alpha)$, introduce in Sec.(7.2.3),can be derived by minimizing the multi-pole moments and the net charge of the system:

$$\Delta Q_L = \left| \int d\mathbf{r} \mathbf{r}^l Y_L(\mathbf{r})(\rho(\mathbf{r}, \mathbf{r}_\alpha) - \hat{\rho}(\mathbf{r}, \mathbf{r}_\alpha)) \right| \tag{C.1}$$

$$\Delta W = \left| \int d\mathbf{r} \mathbf{r}^2 (\rho(\mathbf{r}, \mathbf{r}_\alpha) - \hat{\rho}(\mathbf{r}, \mathbf{r}_\alpha)) \right| \tag{C.2}$$

The parameters of the model density are obtained from a fit to the original charge density, which is biased by a weight function. In the reciprocal space, both requirements Eq.(C.1) and Eq.(C.2) can be translated into expressions that are sensitive only to the intermediate neighborhood of the origin. Thus the fit uses a weighting function of the form:

$$w(\mathbf{k}) = 4\pi \frac{(|\mathbf{k}|^2 - |\mathbf{k}_{cut}|^2)^2}{|\mathbf{k}|^2 |\mathbf{k}_{cut}|^2} \tag{C.3}$$

for $|\mathbf{k}| < |\mathbf{k}_{cut}|$ and zero elsewhere. The weight function enhances the importance of the low k-vectors while ignoring the high k-vectors of the density.

Using the method of Lagrange multipliers, the parameters of the model density q_α are obtained from the extremal condition of

$$\mathcal{L}(q_\alpha, \lambda) = \frac{V}{2} \sum_{\mathbf{k} \neq 0} w(\mathbf{k}) \left| \rho(\mathbf{k}) - \sum_\alpha q_\alpha g_\alpha(\mathbf{k}) \right|^2 - \lambda V \left[\rho(\mathbf{k} = 0) - \sum_\alpha q_\alpha g_\alpha(\mathbf{k} = 0) \right] \tag{C.4}$$

In matrix form the equation can be written in

$$\mathbf{Aq} + \lambda \mathbf{C} = \mathbf{BCq} = N \tag{C.5}$$

where the matrix element of $\mathbf{A}$, $\mathbf{C}$ and $\mathbf{B}$ are given by:

$$A_{i,j} = V \sum_{\mathbf{k} \neq 0} w(\mathbf{k}) [g_i^\dagger(\mathbf{k}) g_j(\mathbf{k})] \tag{C.6}$$

$$C_i = V g_i(\mathbf{k} = 0) = 1 \tag{C.7}$$

$$B_i = V \sum_{\mathbf{k} \neq 0} w(\mathbf{k}) Re[\rho^\dagger(\mathbf{k}) g_i(\mathbf{k})] \tag{C.8}$$

and $\mathbf{q}$ is the array of parameters of the model charge density. The solution to this linear equation system is given by:

$$\mathbf{q} = \mathbf{A}^{-1}\left[\mathbf{B} - \mathbf{C}\frac{\mathbf{C}\mathbf{A}^{-1}\mathbf{B} - N}{\mathbf{C}\mathbf{A}^{-1}\mathbf{C}}\right] \tag{C.9}$$

Appendix D

Derivation of the long-range QM/MM potential

The effect of the periodic copies of the MM sub-system is only in the long-range term, and it comes entirely from the residual function $R_{low}(\mathbf{r}, \mathbf{r}_a)$ of Eq.(7.17):

$$V_{recip}^{QM/MM}(\mathbf{r}, \mathbf{r}_a) = \sum_{\mathbf{L}}^{\infty}{}' \sum_a v_a^{recip} = \sum_{\mathbf{L}}^{\infty}{}' \sum_a R_{low}(|\mathbf{r} - \mathbf{r}_a + \mathbf{L}|) \tag{D.1}$$

This summation has the same convergence properties as the Ewald series, and can be efficiently computed in the reciprocal space. To derive the expression of this modified Ewald sum, let us assume we know the analytical expression of the density $\sigma(\mathbf{r}, \mathbf{r}_a)$ originating from the atomic potential R_{low}. The potential at point $\mathbf{r}_i$ due to the charge distribution $\sigma(\mathbf{r}, \mathbf{r}_a)$ is:

$$V_{recip}^{QM/MM}(\mathbf{r}_i, \mathbf{r}_a) = \int d\mathbf{r} \frac{\sigma(\mathbf{r} + \mathbf{r}_i, \mathbf{r}_a)}{\mathbf{r}} = L^{-3} \int d\mathbf{r} \sum_{\mathbf{k}}^{k_{cut}}{}' \frac{\tilde{\sigma}(\mathbf{k}) \exp[-\imath 2\pi \mathbf{k}(\mathbf{r} + \mathbf{r}_i - \mathbf{r}_a)]}{\mathbf{r}} \tag{D.2}$$

The use of the identity [278]

$$\int d\mathbf{r} \frac{\exp[-\imath 2\pi \mathbf{k}(\mathbf{r} + \mathbf{r}_i - \mathbf{r}_a)]}{\mathbf{r}} = \int_0^{\infty} r dr \int_0^{2\pi} d\phi \int_0^{\pi} \sin\theta d\theta \exp[-\imath 2\pi |\mathbf{k}||\mathbf{r} + \mathbf{r}_i - \mathbf{r}_a| \cos\theta] \tag{D.3}$$

$$= \frac{4\pi}{k^2} \cos[2\pi \mathbf{k} \cdot (\mathbf{r}_i - \mathbf{r}_a)] \tag{D.4}$$

in Eq.(D.2) leads to

$$V_{recip}^{QM/MM}(\mathbf{r}_i, \mathbf{r}_a) = 4\pi L^{-3} \sum_{\mathbf{k}}^{k_{cut}}{}' \frac{\tilde{\sigma}(\mathbf{k})}{k^2} \cos[2\pi \mathbf{k} \cdot (\mathbf{r}_i - \mathbf{r}_a)] \tag{D.5}$$

Using the Maxwell equation $\nabla^2 V = 4\pi\rho$ and its representation in Fourier space, the term in Eq.(D.5)

$$4\pi \frac{\tilde{\sigma}(\mathbf{k})}{k^2} = \tilde{R}_{low}(\mathbf{k}) \tag{D.6}$$

is the Fourier transform of the potential originated by the density of charge $\sigma(\mathbf{r}, \mathbf{r}_a)$. Then the previous equation can be written

$$V_{recip}^{QM/MM}(\mathbf{r}_i, \mathbf{r}_a) = L^{-3} \sum_{\mathbf{k}}^{k_{cut}} {}' \sum_{a} \tilde{R}_{low}(\mathbf{k}) q_a \cos\left[2\pi\mathbf{k} \cdot (\mathbf{r}_i - \mathbf{r}_a)\right] \qquad \text{(D.7)}$$

Appendix E

Derivation of Coulomb potential for delocalized point-like charges

To perform the integration in Eq.(5.7), we consider the integral:

$$I(\mathbf{r}) = \int d^3r' \frac{|\phi(\mathbf{r}' - \mathbf{r}_a)|^2}{|\mathbf{r}' - \mathbf{r}|} \tag{E.1}$$

Using Eq.(5.6) for ϕ and taking the Fourier transformations for $\exp^{-2\xi|\mathbf{r}'-\mathbf{r}_a|}$ and $\frac{1}{|\mathbf{r}'-\mathbf{r}_a|}$, we obtain

$$I = \frac{q_a\xi^3}{\pi} \int d^3r' \left(\frac{2\xi}{\pi^2} \int d^3p \frac{\exp^{\imath\mathbf{p}\cdot(\mathbf{r}'-\mathbf{r}_a)}}{(p^2+4\xi^2)^2} \right) \cdot \left(\frac{1}{2\pi^2} \int d^3q \frac{\exp^{\imath\mathbf{q}\cdot(\mathbf{r}'-\mathbf{r})}}{q^2} \right) \tag{E.2}$$

Rearranging and performing the integration over d^3r', we get

$$I = \frac{q_a\xi^3}{\pi} \frac{2\xi}{\pi^2} \frac{1}{2\pi^2} (2\pi)^3 \int d^3p \int d^3q \delta(\mathbf{p}-\mathbf{q}) * \frac{\exp^{-\imath\mathbf{p}\cdot\mathbf{r}_a}}{(p^2+4\xi^2)^2} \frac{\exp^{\imath\mathbf{q}\cdot\mathbf{r}}}{q^2} \tag{E.3}$$

Performing the integration over d^3q using δ-function integration one obtains

$$I = \frac{q_a\xi^3}{\pi} \frac{8\xi}{\pi} \int d^3p \frac{\exp^{\imath\mathbf{p}\cdot(\mathbf{r}-\mathbf{r}_a)}}{p^2 * (p^2+4\xi^2)^2} \tag{E.4}$$

Decomposing $\frac{1}{p^2*(p^2+4\xi^2)^2}$ we rewrite the above integral as

$$I = \frac{q_a\xi^3}{\pi} \frac{8\xi}{\pi} \int d^3p \left[\frac{1}{\zeta^4 p^2} - \frac{1}{\zeta^4 * (p^2+\zeta^2)} - \frac{1}{\zeta^2 * (p^2+\zeta^2)^2} \right] \cdot \exp^{\imath\mathbf{p}\cdot(\mathbf{r}-\mathbf{r}_a)} \tag{E.5}$$

where $\zeta = 2\xi$. Taking the inverse Fourier transforms for all the three integrals and simplifying for the constants, we finally obtain

$$I = q_a \left[\frac{1}{|\mathbf{r}-\mathbf{r}_a|} - \frac{\exp^{-2\xi|\mathbf{r}-\mathbf{r}_a|}}{|\mathbf{r}-\mathbf{r}_a|} - \xi \exp^{-2\xi|\mathbf{r}-\mathbf{r}_a|} \right] \tag{E.6}$$

Appendix F

Splines

F.0.1 Multi grid

Multi grid methods instead of just a fine grid $\mathcal{G}_f$ use other coarser grids. These grid levels are ordered from the most coarse $\mathcal{G}_c = \mathcal{G}_1$ to the finest $\mathcal{G}_f$ ($1 = c \leq f$). In 3D all the coarser grids do not cost much in term of memory (typically 0.14-0.4 times the memory of the fine grid). Adding these extra grids is useful because each one can represent a given wavelength in an optimal way (i.e. with a minimal number of points), and perform operations on this wavelength efficiently. Typically operations on each grid level are local and work on patches of neighboring points, and after a series of them one collects the result on the fine grid.

Multi grids methods can be used to solve linear equations on a grid, for example partial differential equations, but they aren't yet used for this purpose in CP2K . We use multi grids to transfer the density from the Gaussian basis set to the grid trying to use a constant number of points per Gaussian, as described in [208], and in QM/MM to transfer the MM potential on the grid.

Multi grid is interesting only if there is an efficient way to transfer the operations done on one grid level to the others. For $i < j$ the transfer functions

$$P_j^i : \quad \mathcal{G}_i \to \mathcal{G}_j \tag{F.1}$$

$$R_i^j : \quad \mathcal{G}_j \to \mathcal{G}_i \tag{F.2}$$

are called prolongation and restriction respectively.

If one wants that the integration of a function h defined on a finer grid $\mathcal{G}_j$ with a function g defined on a coarser grid $\mathcal{G}_i$ give the same result both transferring g to the fine grid and summing there or (more efficiently) transferring h to the coarse grid and then summing there one has

$$\langle P_j^i g, h \rangle = \langle g, R_i^j h \rangle \tag{F.3}$$

i.e. the projection is the dual of the restriction.

The prolongation can be seen as an interpolation: given the values on a coarse grid try to find the values on a finer grid. In general one can also imagine a continuous function that underlies the prolongation operation. A very good method for grids with periodic boundary condition is the G-space interpolation. With a fast Fourier transform (FFT) one can find the G-space representation $\hat{n}_{ijk}$ of the points on the grid. Then a continuous representation of them would be

$$n(\boldsymbol{r}) = \sum_{ijk} \hat{n}_{ijk} exp(\boldsymbol{G}(i,j,k) \cdot \boldsymbol{r}), \tag{F.4}$$

where $\boldsymbol{G}(i,j,k) = 2\pi h^{-1}[i,j,k]$, h^{-1} is the inverse of the cell vectors matrix, and i,j,k are evenly distributed between the positive and negative values. The G-space interpolation can be performed directly in the G-space, without going in the direct space. Indeed the $\boldsymbol{G}(i,j,k)$ of the coarser grid are a subset of the ones of the finer grid, and the mapping is trivial, taking care that for an even number of grid points you assign half the value to $N/2$ and half to $-N/2$.

The continuous function underlying the G-space interpolation is C^∞ (i.e. smooth, infinitely often differentiable), and is the best interpolation scheme (with respect to L^2 norm) for points that come from a periodic C^∞ function. Unfortunately if the points come from a function which is not smooth or for a non periodic function this is no longer true.

In CP2K non smoothness is present because at the core there is a jump in the derivative (cusp condition), and the exchange-correlation functionals, especially the gradient corrected ones, exacerbate the problem. This, as explained in the section 3.2.4 is due also to the pseudo potential we use in CP2K . Also introducing a cutoff for the Gaussian loses their smoothness. It was in this setting that we initially introduced the spline approach. This turned out to be more useful that we thought and an extension of it was used to cope with the non periodicity (with respect to the QM cell) of the potential in a QM/MM setting.

F.0.2 Periodic uniform splines

A uniform cardinal B-Spline of order 3 in 3d is a function $\boldsymbol{R}^3 \to \boldsymbol{R}$

$$f(x,y,z) = \sum_{ijk} c_{ijk} N^3(x-i) N^3(y-j) N^3(z-k), \tag{F.5}$$

that is controlled by the coefficients c_{ijk}.

N^3 is a piecewise polynomial function in C^2 with compact support that can be seen as the convolution of the characteristic function of $[-1/2, 1/2]$ ($\chi_{[-1/2,1/2]}$) with itself three times.

$$N^3(t) = \begin{cases} \frac{1}{6}(t+2)^3 & -2 \le t < -1 \\ -\frac{1}{2}t^3 - t^2 + \frac{2}{3} & -1 \le t < 0 \\ \frac{1}{2}t^3 - t^2 + \frac{2}{3} & 0 \le t < 1 \\ -\frac{1}{6}(t-2)^3 & 1 \le t < 2 \\ 0 & \text{otherwise} \end{cases} \tag{F.6}$$

F.0.3 Periodic prolongation/restriction

With this the prolongation operation can be defined as follow:

1. find the coefficients c_{ijk} that interpolate the values v_{ijk} on the coarse grid
2. evaluate the spline Eq.(F.5) on the fine grid to obtain the final values w_{ijk}

We define the function

$$S^i : \mathcal{G}_i \to \mathcal{G}_i \qquad (S^i)_{klm,nop} = N^3(||k-n||) N^3(||l-o||) N^3(||m-p||) \tag{F.7}$$

where $||x||$ is introduced because of periodic boundary conditions, and means the smallest distance, for example for the dimension x

$$||x|| = ((x + N_x/2) \mod N_x) - N_x/2, \tag{F.8}$$

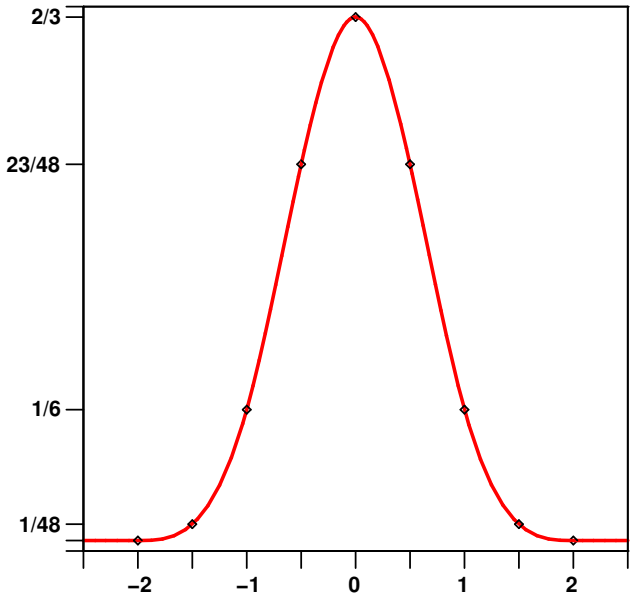

Figure F.1: The N^3 function

where N_x is the number of grid points in the dimension of x. S^i maps the coefficients c_{ijk} to the values v_{ijk}. This matrix is very sparse because the N^3 is different from 0 only for the nearest neighbor, i.e. for an integer value i

$$N^3(i) = \begin{cases} \frac{1}{6} & \text{if } i = -1 \\ \frac{2}{3} & \text{if } i = 0 \\ \frac{1}{6} & \text{if } i = 1 \\ 0 & \text{otherwise} \end{cases} \tag{F.9}$$

The application $S^i c$ can be seen as the convolution of the grid with the 3x3x3 stencil (indexed from -1 to 1) with values

$$S_4 = \frac{2}{3}^{3-|i|-|j|-|k|} \frac{1}{6}^{|i|+|j|+|k|} \tag{F.10}$$

which has values

$$[[\frac{8}{27}, \frac{2}{27}, \frac{1}{54}, \frac{1}{216}]] \tag{F.11}$$

for center, face centers,edges, and vertices of the 3x3x3 cube. This is the same S_4 operation used in the XC section (3.2.4) and can be implemented very efficiently.

Then the first step of the prolongation is

$$c = (S^i)^{-1} v \tag{F.12}$$

which we calculate iteratively with a conjugated gradient solver, using

$$[[2 - \frac{8}{27}, -\frac{2}{27}, -\frac{1}{54}, -\frac{1}{216}]] \tag{F.13}$$

as approximate inverse for the first guess, and

$$[[4.096, -1.28, 0.4, -0.125]] \tag{F.14}$$

as pre-conditioner. The pre-conditioner is generated by the 1d-values $[-1.6/4, 1.6, -1.6/4]$ in each direction. It was found by minimizing the condition number of S^i multiplied by operators generated from 1d-values, and then (slightly) further optimized in the program. With this in 10-15 iterations, independently of the size of the grid, a convergence to less than 10^{-10} for both argument and residual can be achieved.

To evaluate the spline on the fine grid we use commensurate grids for efficiency reasons, which means that each grid has exactly the double of the number of points in every direction than the previous grid level. In this case it is useful to introduce the (rectangular) matrix.

$$(T^i_{i+1})_{klm,nop} = N^3(\frac{k}{2} - n)N^3(\frac{l}{2} - o)N^3(\frac{m}{2} - p) \tag{F.15}$$

which is very sparse as for half integer the only nonzero values are

$$N^3(\frac{i}{2})_{i=-4..4} = [0, \frac{1}{48}, \frac{1}{6}, \frac{23}{48}, \frac{2}{3}, \frac{23}{48}, \frac{1}{6}, \frac{1}{48}, 0] \tag{F.16}$$

Thus we have

$$P^i_{i+1} = T^i_{i+1}(S^i)^{-1}, \tag{F.17}$$

and

$$R^{i+1}_i = (P^i_{i+1})^T = (S^i)^{-1}(T^i_{i+1})^T. \tag{F.18}$$

The interpolation between the other grid levels can be defined as the product of the cascade prolongation/restrictions from grid i to grid j

$$P^i_j = \prod_{k=j-1}^{i} P^k_{k+1} = P^{j-1}_j ... P^{i+1}_{i+2} P^i_{i+1}, \tag{F.19}$$

and

$$R^j_i = \prod_{k=i}^{j-1} R^{k+1}_k = R^{i+1}_i R^{i+2}_{i+1} ... R^j_{j-1}. \tag{F.20}$$

This approach works very well with periodic boundary conditions. The coefficients of the spline can be seen as the G-space coefficients of a Fourier transform. Like them they depend in a unique and global way from the values on the grid (direct space): any coefficient depends on the values of all the grid, but with the splines the weight of far away points decreases faster than with G-space interpolation, splines are more localized.

The coefficients define a continuous function that on the grid has exactly the values of the direct space, but that is defined everywhere, not just on the grid, and thus they can be used to interpolate the values, or transfer the function between grid levels. The continuous function defined by the cubic splines is C^2 (twice continuously differentiable). This is not optimal to interpolate smooth functions, but if the function to interpolate is not so regular (due for example to cutoff effects, or numerical instabilities) then the spline interpolation becomes better. In fact local discontinuities, being the spline more localized, spread around less as can be seen looking at the interpolation of a delta like function on a grid, which as was discussed in section 3.2.4 is similar to the situation that arises in the core of the atom with gradient corrected functions.

F.0.4 Non-periodic uniform splines

If one wants to go beyond the periodic boundary conditions the function N^3 cannot be used for the coefficients close to the border. Indeed using the N^3 function would force the function to go at 0 and with derivative 0 two units after the border, and what is worse (one can argue that what happens beyond the border is not relevant and is an artifact) a simple linear function cannot be interpolated exactly. This gives rise to border effects that cannot be neglected. This problem is important for QM/MM where the potential generated by the MM atoms is not periodic with respect to the QM cell. As already stated the solution is to modify the form of the N^3 functions for the coefficients close to the border.

To find out how to modify the functions we will look at a generalization of the uniform cardinal splines. To simplify the discussion we will first look at a non-uniform B-Spline of order 3 in just 1 dimension. This is a parametric 1d line in a 2d dimensional space, i.e. a $\boldsymbol{R} \to \boldsymbol{R}^2$ function

$$g(u) = \sum_i P_i N^3(u - i), \tag{F.21}$$

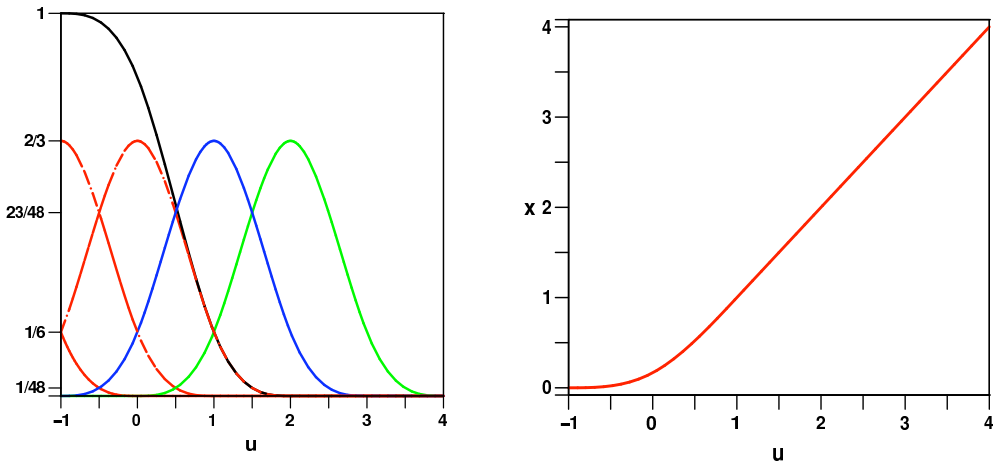

Figure F.2: The left panel shows the weights of the splines for $i = -2..2$. The dotted red splines (with $i = -2..0$) have the same coefficient, so they have been summed up into the continuous black line. The right panel shows the value of x as function of u

where P_i is an array (indexed by the integer i) of 2-dimensional vectors.

This looks complicated, but if one sets

$$P_i = [i, v_i] \tag{F.22}$$

then if we call the first component of g, x and the second h

$$[x(u), h(u)] := g(u), \tag{F.23}$$

we see that the mapping $x(u)$ is the identity and

$$h(u) = h(x) = \sum_i v_i N(x - i) \tag{F.24}$$

and so h is just a uniform cardinal spline.

Assuming that the lower boundary is at 0, we want to look at

$$P_i = [\max(0, i), v_{\max(0,i)}]. \tag{F.25}$$

As we can see for $u \geq 1$ $u = x$, but for smaller values the correspondence breaks and the function gets really parametric. x begins to change more and more slowly, and finally freezes at 0 when u reaches -1. Now the correct way to redefine the $N^3(x - i)$ to functions $M_i(x)$ for i close to the border (i.e. to 0) is

$$\begin{aligned} M_0(x(u)) &= N^3(u + 2) + N^3(u + 1) + N^3(u) \\ M_1(x(u)) &= N^3(u - 1) \\ M_2(x(u)) &= N^3(u - 2) \end{aligned} \tag{F.26}$$

and for $i > 2$ $M_i(x) = N^3(x - i)$.

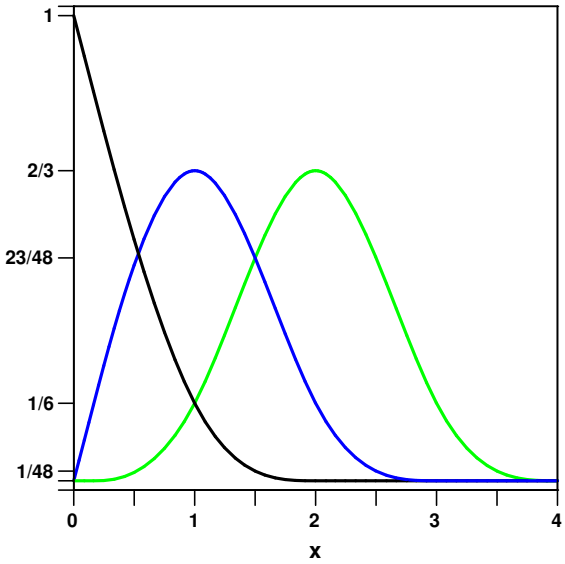

Figure F.3: The border functions $M_{0..2}$ as function of x.

To be able to directly represent $M_{0..2}(x)$ one has to invert $x(u)$

$$x^{-1}(t) = \begin{cases} \text{undefined} & t < 0 \\ \sqrt[3]{6u} - 1 & t < \frac{1}{6} \\ 2\sqrt{2}\cos\left(\frac{1}{3}(\pi + \arccos(\frac{3\sqrt{2}(t-1)}{4}))\right) + 1 & t < 1 \\ t & t \geq 1 \end{cases} \tag{F.27}$$

With an explicit inverse one obtains a direct representation of the functions $M_{0..2}$ shown in figure F.3 We see that for the evaluation on a grid with spacing 1 only the weight exactly at the border has to be changed (to 1), whereas for an uniform refinement, i.e. to prolongate to a grid with spacing 1/2, the border and the points just before it have to be changed. Approximately $M_{0...2}$ have the following values at the important points:

$$\begin{aligned} M_0(0) &= 1 & M_0(\tfrac{1}{2}) &= 0.51797770339331435652 9532 \\ M_1(0) &= 0 & M_1(\tfrac{1}{2}) &= 0.46404459321337128694 0937 \\ M_2(0) &= 0 & M_2(\tfrac{1}{2}) &= 0.01797770339331435652 9531. \end{aligned} \tag{F.28}$$

Thus using the weights given by M_0, M_1, M_2 instead of the ones given by N^3 at the border the simplicity of the uniform spline schema can be kept and linear functions can be correctly interpolated. The upper border is just symmetric.

In 3d we have to look at non-uniform B-Spline of order 3 in 3 dimensions, which are parametric 3d surfaces in a 4d dimensional space, i.e. a $\boldsymbol{R}^3 \to \boldsymbol{R}^4$ function

$$g(u, v, t) = \sum_{ijk} P_{ijk} N^3(u - i) N^3(v - j) N^3(t - k), \tag{F.29}$$

where P_{ijk} is a 3d grid (indexed by the integer i, j, k) of 4-dimensional vectors.

Looking at it one can see that the fact that the weight functions are just a direct product of the 1d weighting functions is preserved with boundaries along the border of a box. Assuming that the lower left corner of the box is for $(i, j, k) = (0, 0, 0)$

$$f(x, y, z) = \sum_{ijk} v_{ijk} M_i(x) M_j(y) M_k(z), \tag{F.30}$$

with M_i as defined in the 1d case.

F.0.5 Non-periodic prolongation/restriction

The prolongation and restriction operation can be calculated just as before

$$P_j^i = \tilde{T}_j^i (\tilde{S}^i)^{-1} \tag{F.31}$$

$$R_i^j = (P_j^i)^T = ((\tilde{S}^i)^T)^{-1} (\tilde{T}_j^i)^T \tag{F.32}$$

where $\tilde{S}^i$ and $\tilde{T}_j^i$ are different from S^i and T_j^i because they use $M_i(x)$ instead of the $N^3(x - i)$. This means that $\tilde{S}^i$ differs from S^i only at the border where in each dimension 1 is used instead of 2/3 as weight and the 1/6 contribution from the neighboring point is ignored. This breaks the symmetry of S^i and makes the sum of the contributions of the weights c close to the border differ from 1. Likewise $\tilde{T}_j^i$ differs from T_j^ionly at the border using the values of Eq.(F.28).

The inversion of $\tilde{S}^i$ is performed using the same approximate inverse as in the non-periodic case, but setting the weight to 1 instead of 2/3 at the border, and removing the 1/6 contribution from the point next to the border, as with $\tilde{S}$. For the pre-conditioner the contribution from the weight c at the border are scaled in such a way that at the value at the border is 1 (i.e. not just setting the border to one, but also changing the contribution to the close-by v. With this method the same performance as in the periodic case can be achieved on big grids: ≈ 12 iterations for 10^{-10} accuracy, ≈ 20 for machine accuracy (10^{-14}). For small grids other approximate inverse and pre-conditioners (not based on the the periodic solution) would be better, but $\approx 1/3$ more iterations on the small grids is not costly, and not worth extra optimization.

Such a function can describe exactly hyper planes, is efficient to evaluate and has worked very well for the QM/MM implementation in CP2K .

Bibliography

[1] A. Crespo, D. A. Scherlis, M. A. Martí, P. Ordejon, A. E. Roitberg, and D. A. Estrin. A DFT-based QM-MM approach designed for the treatment of large molecular systems: Application to chorismate mutase. **J. Phys. Chem. B**, 107(49), 13728–13736, (2003). ix, 58

[2] A. Laio, J. VandeVondele, and U. Röthlisberger. A Hamiltonian electrostatic coupling scheme for hybrid Car-Parrinello molecular dynamics simulations. **J. Chem. Phys. B**, 106(16), 7300–7307, (2002). ix, 13, 20, 49, 51, 52, 53, 54, 57, 58, 65, 66, 67

[3] M. Head-Gordon, M. Lee, P. Maslen, T. van Voorhis, and S. Gwaltney. **Modern Methods and Algorithms of Quantum Chemistry**, volume 3 of **NIC Series**, Tensors in Electronic Structure Theory: Basic Concepts and Applications to Electron Correlation Models, pages 593–638. John von Neumann Institute for Computing, (2000). 6

[4] F. Krajewski and M. Parrinello. Stochastic linear scaling for metals and non-metals. **Phys. Rev. B**, 71(23), No.233105, (2005). 6

[5] A. Warshel and M. Levitt. Theoretical Studies of Enzymatic Reactions: Dielectric, Electrostatic and Steric stabilization of the carbonium ion in the reaction of Lysozime. **J. Mol. Biol.**, 103(2), 227–249, (1976). 6, 9, 10, 13

[6] J. Gao. Methods and applications of combined quantum mechanical and molecular mechanical potentials. **Reviews in Computational Chemistry**, 7, 119–185, (1996). 9

[7] T.Z. Mordasini and W. Thiel. Combined quantum mechanical and molecular mechanical approaches. **Chimia**, 52(6), 288–291, (1998). 9

[8] P. Sherwood. **Modern Methods and Algorithms of Quantum Chemistry**, volume 1 of **NIC Series**, Hybrid quantum mechanics/molecular mechanics approaches, pages 257–277. John von Neumann Institute for Computing, (2000). 9, 20

[9] M.J. Field, P.A. Bash, and M. Karplus. A Combined Quantum Mechanical and Molecular Mechanical potential for molecular dynamics simulation. **J. Comput. Chem.**, 11(6), 700–733, (1990). 9, 10, 12, 14, 15, 17, 19, 21, 22

[10] U.C. Singh and P.A. Kollman. A combined *ab initio* quantum mechanical and molecular mechanical method for carrying out simulations on complex molecular systems: Applications to the $CH_3Cl + Cl^-$ exchange reaction and gas-phase protonation of polyethers. **J. Comput. Chem.**, 7(6), 718–730, (1986). 10, 12, 13, 20, 50, 58

[11] D. Bakowies and W. Thiel. Hybrid models for combined quantum mechanical and molecular mechanical approaches. **J. Phys. Chem.**, 100(25), 10580–10594, (1996). 11, 12, 14

[12] B. Waszkowycz, I.H. Hillier, N. Gensmantel, and D.W. Payling. Combined quantum mechanical-molecular mechanical study of catalysis by the enzyme phospholipase-A2 - an investigation of the potential energy surface for amide hydrolysis. **J. Chem. Soc., Perkin Trans.**, 2(12), 2025–2032, (1991). 12, 20

[13] R.V. Stanton, D.S. Hartsough, and K.M. Merz. Calculation of solvation free energies using a density functional/molecular dynamics coupled potential. **J. Phys. Chem.**, 97(46), 11868–11870, (1993). 12

[14] Y.S. Lee, M. Hodoscek, B.R. Brooks, and P.F. Kador. Catalytic mechanism of aldose reductase studied by the combined potentials of quantum mechanics and molecular mechanics. **Biophys. Chem.**, 70(3), 203–216, (1998). 12, 21, 22

[15] P.D. Lyne and M. Hodoscek ans M. Karplus. A hybrid QM-MM potential employing Hartree-Fock or density functional methods in the quantum region. **J. Phys. Chem. A**, 103(18), 3462–3471, (1999). 12, 21, 22

[16] A.J. Turner, V. Moliner, and I.H. Williams. Transition-state structural refinement with GRACE and CHARMM: Flexible QM/MM modeling for lactate dehydrogenase. **Phys. Chem. Chem. Phys.**, 1(6), 1323–1331, (1999). 12

[17] K.P. Eurenius, D.C. Chatfield, B.R. Brooks, and M. Hodoscek. Enzyme mechanisms with hybrid quantum and molecular mechanical potentials. 1. Theoretical considerations. **Int. J. Quant. Chem.**, 60(6), 1189–1200, (1996). 12

[18] M. Sierka and J. Sauer. Structure and reactivity of silica and zeolite catalysts by a combined quantum mechanics-shell-model potential approach based on DFT. **Faraday Discuss.**, 106, 41–62, (1997). 13

[19] S. Humbel, S. Seiber, and K. Morokuma. The IMOMO method: Integration of different levels of molecular orbital approximations for geometry optimisation of large systems: Test for n-butane conformation and S_n2 reaction RCl + Cl^-. **J. Chem. Phys.**, 105(5), 1959–1967, (1996). 13

[20] R.D.J. Froese, S. Humbel, M. Svensson, and K. Morokuma. IMOMO(G2MS): A new high-level G2-like method for large molecules and its application to Diels-Alder Reactions. **J. Phys. Chem.**, 101(2), 227–233, (1997). 13

[21] M. Svensson, S. Humbel, R.D.J. Froese, T. Matsubara, S. Sieber, and K. Morokuma. ONIOM: A Multilayered Integrated MO+MM Method for geometry optimizations and single point energy predictions. A test for Diels-Alder reactions and $Pt(P(t\text{-}Bu)_3)_2 + H_2$ oxidative addition. **J. Phys. Chem.**, 100(50), 19357–19363, (1996). 13

[22] T. Vreven and K. Morokuma. Investigation of the $S_0 \rightarrow S_1$ excitation in bacteriorhodopsin with the ONIOM(MO:MM) hybrid method. **Theor. Chem. Acc.**, 109(3), 125–132, (2003). 13

[23] J.J.P. Stewart. **MOPAC2000**. Fujitsu Limited, Tokio, Japan, (1999). 13

[24] J.D. Thompson, C.J. Cramer, and D.G. Truhlar. Parameterization of charge model 3 for AM1, PM3, BLYP, and B3LYP. **J. Comput. Chem.**, 24(11), 1291–1304, (2003). 13

[25] J.J.P. Stewart. Optimization of parameters for semiempirical methods .1. Method. **J. Comput. Chem.**, 10(2), 209–220, (1989). 13

[26] J.J.P. Stewart. Optimization of parameters for semiempirical methods. 2. Applications. **J. Comput. Chem.**, 10(2), 221–264, (1989). 13

[27] J.J.P. Stewart. Optimization of parameters for semiempirical methods .3. extension of PM3 to Be, Mg, Zn, Ga, Ge, As, Se, Cd, In, Sn, Sb, Te, Hg, Tl, Pb and Bi. **J. Comput. Chem.**, 12(3), 320–341, (1991). 13

[28] G. Lippert, J. Hutter, and M. Parrinello. The Gaussian and augmented-plane-wave density functional method for ab initio molecular dynamics simulations. **Theor. Chem. Acc.**, 103(2), 124–140, (1999). 13, 26, 34

[29] M. Krack and M. Parrinello. All-electron ab-initio molecular dynamics. **Phys. Chem. Chem. Phys.**, 2(10), 2105–2112, (2000). 13, 26, 34

[30] M. Persico, G. Granucci, S. Inglese, T. Laino, and A. Toniolo. Semiclassical simulation of photochemical reactions in condensed phase. **J. Mol. Struct. (THEOCHEM)**, 621(1-2), 119–126, (2003). 13, 14

[31] J.H. Harding, A.H. Harker, P.B. Keegstra, R. Pandey, J.M. Vail, and C. Woodward. Hartree-Fock cluster computations of defect and perfect ionic crystal properties. **Physica B**, 131(1-3), 151–156, (1985). 13

[32] D. Wei and D.R. Salahub. A combined density functional and molecular dynamics simulation of a quantum water molecule in aqueous solution. **Chem. Phys. Lett.**, 224(3-4), 291–296, (1994). 13

[33] X.P. Long, J.B. Nicholas, M.F. Guest, and R.L. Ornstein. A combined density functional theory molecular mechanics formalism and its application to small water clusters. **J. Mol. Struct.**, 412(1-2), 121–133, (1997). 13

[34] T.K. Woo, P.M. Margl, P.E. Blöchl, and T. Zeigler. A combined Car-Parrinello QM/MM implementation for *ab initio* molecular dynamics simulations of extended systems: Application to transition metal catalysis. **J. Phys. Chem.**, 101(40), 7877–7880, (1997). 13

[35] M. Eichinger, P. Tavan, J. Hutter, and M. Parrinello. A hybrid method for solutes in complex solvents: Density functional theory combined with empirical forcefields. **J. Chem. Phys.**, 110(21), 10452–10467, (1999). 13, 21, 50, 52, 53, 54

[36] B.R. Brooks, R.E. Bruccoleri, B.D. Olafson, D.J. States, and S. Swaminathan. CHARMM - A program for macromolecular energy, minimization and dynamics calculations. **J. Comput. Chem.**, 4(2), 187–217, (1983). 14, 58

[37] D. Case, D. Pearlman, J. Caldwell, T.E. Cheatham III, W. Ross, C. Simmerling, T. Darden, K. Merz, R. Stanton, A. Cheng, J. Vincent, M. Crowley, V. Tsui, R. Radmer, Y. Duan, J. Pitera, I. Massova, G. Seibel, U. Singh, P. Weiner, and P.A. Kollman. AMBER v.9.0. Technical report, University of California, San Francisco, (2002). 14, 58, 67

[38] J.H. Lii and N.L. Allinger. The MM3 forcefield for amides, polypeptides and proteins. **J. Comput. Chem.**, 12(2), 186–199, (1991). 14, 20

[39] J.R. Maple, M.-J. Hwang, T.P. Stockfisch, U. Dinur, M. Waldman, C.S. Ewig, and A.T. Hagler. Derivation of class-II forcefields. 1. Methodology and quantum forcefield for the alkyl functional group and alkane molecule. **J. Comput. Chem.**, 15(2), 162–182, (1994). 14

[40] B.G. Dick and A.W. Overhauser. Theory of the dielectric constants of alkali halide crystals. **Phys. Rev.**, 112(1), 90–103, (1958). 14, 15

[41] B. W. H. van Beest, G. J. Kramer, and R. A. van Santen. Force fields for silicas and aluminophosphates based on ab initio calculations. **Phys. Rev. Lett.**,

64(16), 1955–1958, (1990). 14, 43, 78, 84, 95

[42] D. Bakowies and W. Thiel. Semiempirical treatment of electrostatic potentials and partial charges in combined quantum mechanical and molecular mechanical approaches. **J. Comput. Chem.**, 17(1), 87–108, (1996). 15

[43] R.A. Bryce, M.A. Vincent, and I.H. Hillier. Binding energy of $F(H_2O)^-$ and the simulation of fluoride water clusters using QM/MM (fluctuating charge) potential. **J. Phys. Chem. A**, 103(20), 4094–4100, (1999). 15

[44] P.L. Cummins and J.E. Gready. The electrostatic potential in the semiempirical molecular orbital approximation. **Chem. Phys. Lett.**, 225(1-3), 11–17, (1994). 15

[45] B.T. Thole. Molecular Polarizabilities calculated with a modified dipole interaction. **Chem. Phys.**, 59(3), 341–350, (1981). 15

[46] M.A. Thompson. QM/MMpol: A consistent model for solute/solvent polarization. Application to acqueous solvation and spectroscopy of formaldehyde, acetaldehyde and acetone. **J. Phys. Chem.**, 100(34), 14492–14507, (1996). 15

[47] I. Antes and W. Thiel. **Combined Quantum Mechanical and Molecular Mechanical Methods**, volume 712 of **ACS Symp.**, page 50. American Chemical Society, Washington, DC, (1998). 15, 19, 20

[48] B.T. Thole and P.T. van Duijnen. On the quantum mechanical treatment of the solvent. **Theor. Chim. Acta**, 55(4), 307–318, (1980). 15

[49] A.H. de Vries, P.T. van Duijnen, A.H. Juffer, J.A.C. Rullmann, J.P. Dijkman, H. Merenga, and B.T. Thole. Implementation of reaction field methods in quantum chemistry computer codes. **J. Comput. Chem.**, 16(1), 37–55, (1995). Correction in **J. Comput. Chem.** 16(11), 1445-1446 (1995). 15

[50] P.T. van Duijnen and A.H. de Vries. Direct reaction field forcefield: A consistent way to connect and combine quantum chemical and classical descriptions of molecules. **Int. J. Quant. Chem.**, 60(6), 1111–1132, (1996). 15

[51] A.H. de Vries and P.T. van Duijnen. Solvatochromism of the $\pi^* \leftarrow n$ transition of acetone by combined quantum mechanical classical mechanical calculations. **Int. J. Quant. Chem.**, 57(6), 1067–1076, (1996). 15

[52] P.T. van Duijnen, F. Grozema, and M. Swart. Some applications of the direct field approach. **J. Mol. Struct. (THEOCHEM)**, 464(1-3), 191–198, (1999). 15

[53] P.A. Bash, L. Lawrence, A.D. MacKerell Jr., D. Levine, and P. Hallstrom. Progress toward chemical accuracy in the computer simulation of condensed phase reactions. **PNAS USA**, 93(8), 3698–3703, (1996). 15

[54] J. Gao. Toward a molecular orbital derived empirical potential for liquid simulations. **J. Phys. Chem. B**, 101(4), 657–663, (1997). 15

[55] M. Freindorf and J. Gao. Optimization of the Lennard-Jones parameters for a combined ab initio quantum mechanical and molecular mechanical potential using the 3-21G basis set. **J. Comput. Chem.**, 17(4), 386–395, (1996). 15

[56] P.L. Cummins and J.E. Gready. Coupled semiempirical molecular orbital and molecular mechanics model (QM/MM) for organic molecules in aqueous solution. **J. Comput. Chem.**, 18(12), 1496–1512, (1997). 15

[57] Y.Q. Tu and A. Laaksonen. On the effect of Lennard-Jones parameters on the quantum mechanical and molecular mechanical coupling in a hybrid molecular

dynamics simulation of liquid water. **J. Comput. Chem.**, 111(16), 7519–7525, (1999). 15, 49, 50

[58] Sherwood et al. Hyperchem Users Manual, Computational Chemistry. Technical report, Hypercube Inc., Ontario, Canada, (1994). 15

[59] I. Antes and W. Thiel. Adjusted connection atoms for combined quantum mechanical and molecular mechanical methods. **J. Phys. Chem. A**, 103(46), 9290–9295, (1999). 16, 17

[60] Y.K. Zhang, T.S. Lee, and W.T. Yang. A pseudobond approach to combining quantum mechanical and molecular mechanical methods. **J. Chem. Phys.**, 110(1), 46–54, (1999). 16, 85

[61] V. Thery, D. Rinaldi, J.-L. Rivail, B. Maigret, and G.G. Ferenczy. Quantum mechanical computations on very large molecular systems: The local self consistent field method. **J. Comput. Chem.**, 15(3), 269–282, (1994). 16

[62] G. Monard, M. Loos, V. Thery, K. Baka, and J.-L. Rivail. Hybrid classical quantum force field for modeling very large molecules. **Int. J. Quant. Chem.**, 58(2), 153–159, (1996). 16, 85

[63] J. Gao, P. Amara, C. Alhambra, and M.J. Field. A Generalized Hybrid Orbital (GHO) Method for treatment of boundary atoms in QM/MM calculations. **J. Phys. Chem.**, 102(24), 4714–4721, (1998). 16, 49, 50, 85

[64] G.A. DiLabio, M.H. Hurley, and P.A. Christiansen. Simple one-electron quantum capping potentials for use in hybrid QM/MM studies of biological molecules. **J. Chem. Phys.**, 116(22), 9578–9584, (2002). 17

[65] O. A. von Lilienfeld, I. Tavernelli, U. Röthlisberger, and D. Sebastiani. Variational optimization of effective atom centered potentials for molecular properties. **J. Chem. Phys.**, 122(1), 141113–14118, (2005). 17

[66] N. Reuter, A. Dejaegere, B. Maigret, and M. Karplus. Frontier bonds in QM/MM methods: A comparison of different approaches. **J. Phys. Chem. A**, 104(8), 1720–1735, (2000). 17, 19

[67] D.M. Phillip and R.A. Friesner. Mixed *ab initio* QM/MM modeling using frozen orbitals and tests with alanine dipeptide and tetrapeptide. **J. Comput. Chem.**, 20(14), 1468–1494, (1999). 17

[68] R.J. Hall, S.A. Hindle, N.A. Burton, and I.H. Hillier. Aspects of Hybrid QM/MM Calculations: The treatment of the QM/MM interface region and geometry optimization with an application to Chorismate Mutase. **J. Comput. Chem.**, 21(16), 1433–1441, (2000). 17

[69] S. Dapprich, I. Komaromi, K.S. Byun, K. Morokuma, and M.J. Frisch. A new ONIOM implementation in Gaussian98. Part I. The calculation of energies, gradients, vibrational frequencies and electric field derivatives. **J. Mol. Str. (THEOCHEM)**, 461-462, 1–21, (1999). 17

[70] T. Vreven and K. Morokuma. The ONIOM (our own N-layered integrated molecular orbital + molecular mechanics) method for first singlet excited (S_1) state photoisomerization path of a retinal protonated Schiff base. **J. Chem. Phys.**, 113(8), 2969–2975, (2000). 17

[71] J. Sauer and M. Sierka. Combining Quantum Mechanics and Interatomic Potential Functions in *ab initio* Studies of Extended Systems. **J. Comput. Chem.**, 21(16), 1470–1493, (2000). 17

[72] F. Maseras and K. Morokuma. A new integrated *ab initio* plus molecular mechanics geometry optimization scheme of equilibrium structures and transition states. **J. Comput. Chem.**, 16(9), 1170–1179, (1995). 18

[73] T.K. Woo, L. Cavallo, and T. Ziegler. Implementation of the IMOMM methodology for performing combined QM/MM molecular dynamics simulations and frequency calculations. **Theor. Chem. Acc.**, 100(5-6), 307–313, (1998). 18

[74] M. Swart. AddRemove: A new link model for use in QM/MM studies. **Int. J. of Quant. Chem.**, 91(2), 177–183, (2003). 18

[75] A.H. de Vries, P. Sherwood, S.J. Collins, A.M. Rigby, M. Rigutto, and G.J. Kramer. Zeolite structure and reactivity by combined quantum - chemical - classical calculations. **J. Phys. Chem. B**, 103(29), 6133–6141, (1999). 19, 20

[76] MariaLore Sulpizi. ***Ab initio* studies of targets for pharmaceutical intervention**. PhD thesis, SISSA - ISAS, (2001). 19

[77] F.A. Momany, R.F. McGuire, A.W. Burgess, and H.A. Scheraga. Energy parameters in polypeptides. VII. Geometric parameters, partial atomic charges, nonbonded interactions, hydrogen bond interactions, and intrinsic torsional potentials for the naturally occurring amino acids. **J. Phys. Chem.**, 79(22), 2361–2381, (1975). 19, 44

[78] P.E. Smith and W.F. van Gunsteren. **Computer Simulation of Biomolecular Systems**, volume 2, pages 182–212. ESCOM, Leiden, (1993). 20

[79] P.E. Sinclair, A. de Vries, P. Sherwood, C.R.A. Catlow, and R.A. van Santen. Quantum chemical studies of alkene chemisorption in chabazite: A comparison of cluster and embedded-cluster models. **J. Chem. Soc., Faraday Trans.**, 94(22), 3401–3408, (1998). 20

[80] P.K. Biswas and V. Gogonea. A regularized and renormalized electrostatic coupling Hamiltonain for hybrid quantum mechanical - molecular mechanical calculations. **J. Chem. Phys.**, 123(16), No. 164114, (2005). 20, 49, 52, 53, 54

[81] T. Laino, F. Mohamed, A. Laio, and M. Parrinello. An efficient real space multigrid QM/MM electrostatic coupling. **J. Chem. Theory Comp.**, 1(6), 1176–1184, (2005). 21, 70, 72, 73, 74

[82] T. Laino, F. Mohamed, A. Laio, and M. Parrinello. An Efficient Linear-Scaling Electrostatic Coupling for treating periodic boundary conditions in QM/MM Simulations. **J. Chem. Theory Comp.**, 2(5), 1370–1378, (2006). 21

[83] P. Sherwood and A.H. de Vries. **ChemShell Users Manual**. CLRC Daresbury Laboratory, (1997). 22

[84] The CP2K developers group. · freely available at the URL:: http://cp2k.berlios.de, released under GPL license., (2007). 25, 28, 57, 68, 70, 80, 105

[85] J. VandeVondele, M. Krack, F. Mohamed, M. Parrinello, T. Chassaing, and J. Hutter. QUICKSTEP: Fast and accurate density functional calculations using a mixed Gaussian and plane waves approach. **Comp. Phys. Comm.**, 167(2), 103–128, (2005). 25, 27, 29, 32, 33, 34, 58, 65, 74, 95

[86] P. Hohenberg and W. Kohn. Inhomogeneous electron gas. **Phys. Rev. B**, 136(3B), B864–B871, (1964). 25, 27, 95

[87] W. Kohn and L. J. Sham. Self-consistent equations including exchange and correlation effects. **Phys. Rev.**, 140(4A), A1133–A1139, (1965). 25, 27, 95

[88] S. Goedecker. Linear scaling electronic structure methods. **Rev. Mod. Phys.**, 71(4), 1085–1123, (1999). 25, 26

[89] G. Lippert, J. Hutter, and M. Parrinello. A hybrid Gaussian and plane wave density functional scheme. **Mol. Phys.**, 92(3), 477–487, (1997). 25, 26

[90] D. Marx and J. Hutter. *ab-initio* Molecular Dynamics: Theory and Implementation. In J. Grotendorst, editor, **Modern Methods and Algorithms of Quantum Chemistry**, volume 1 of **NIC Series**, pages 329–477. FZ Jülich, Germany, (2000). see also http://www.fz-juelich.de/nic-series/Volume1/. 25, 28

[91] L. Füsti-Molnár and P. Pulay. Accurate molecular integrals and energies using combined plane wave and Gaussian basis sets in molecular electronic structure theory. **J. Chem. Phys.**, 116(18), 7795–7805, (2002). 25

[92] L. Füsti-Molnár and P. Pulay. The Fourier transform Coulomb method: Efficient and accurate calculation of the Coulomb operator in a Gaussian basis. **J. Chem. Phys.**, 117(17), 7827–7835, (2002). 25

[93] L. Füsti-Molnár and P. Pulay. Gaussian-based first-principles calculations on large systems using the Fourier Transform Coulomb method. **Theochem-J. Mol. Struct.**, 666, 25–30, (2003). 25

[94] L. Füsti-Molnár. New developments in the Fourier transform Coulomb method: Efficient and accurate localization of the filtered core functions and implementation of the Coulomb energy forces. **J. Chem. Phys.**, 119(21), 11080–11087, (2003). 25

[95] J. Baker, L. Füsti-Molnár, and P. Pulay. Parallel density functional theory energies using the Fourier transform Coulomb method. **J. Phys. Chem. A**, 108(15), 3040–3047, (2004). 25

[96] J. L. Whitten. Coulombic potential energy integrals and approximations. **J. Chem. Phys.**, 58(10), 4496–4501, (1973). 25

[97] B. I. Dunlap, J. W. D. Connolly, and J. R. Sabin. On first-row diatomic molecules and local density models. **J. Chem. Phys.**, 71(12), 4993–4999, (1979). 25

[98] O. Vahtras, J. Almlöf, and M. W. Feyereisen. Integral approximations for LCAO-SCF calculations. **Chem. Phys. Lett.**, 213, 514–518, (1993). 26

[99] K. Eichorn, O. Treutler, H. Öhm, M. Häser, and R. Ahlrichs. Auxiliary basis sets to approximate Coulomb potentials. **Chem. Phys. Lett.**, 240, 283–290, (1995). 26

[100] K. Eichorn, F. Weigend, O. Treutler, and R. Ahlrichs. Auxiliary basis sets for main row atoms and transition metals and their use to approximate Coulomb potentials. **Theor. Chem. Acc.**, 97, 119–124, (1997). 26

[101] B. Delley. An all-electron numerical method for solving the local density functional for polyatomic molecules. **J. Chem. Phys.**, 92(1), 508–517, (1989). 26

[102] V. Termath and N. C. Handy. A Kohn-Sham method involving the direct determination of the Coulomb potential on a numerical grid. **Chem. Phys. Lett.**, 230, 17–24, (1994). 26

[103] T. L. Beck. Real-space mesh techniques in density-functional theory. **Rev. Mod. Phys.**, 72, 1041–1080, (2000). 26

[104] X. Chen, J.-M. Langlois, and W. A. Goddard III. Dual-space approach for density-functional calculations of two and three-dimensional crystals using Gaussian basis functions. **Phys. Rev. B**, 52, 2348–2361, (1995). 26

[105] P. Ordejón, E. Artacho, and J. M. Soler. Self-consistent order-N density-functional calculations for very large systems. **Phys. Rev. B**, 53, R10441–R10444, (1996). 26

[106] C. M. Goringe, E. Hernández, M. J. Gillan, and I. J. Bush. Linear-scaling DFT-pseudopotential calculations on parallel computers. **Comp. Phys. Comm.**, 102, 1–16, (1997). 26

[107] S. D. Kenny, A. P. Horsfield, and H. Fujitani. Transferable atomic-type basis sets for solids. **Phys. Rev. B**, 62, 4899–4905, (2000). 26

[108] A. A. Mostofi, C.-K. Skylaris, P. D. Haynes, and M. C. Payne. Total-energy calculations on a real space grid with localized functions and a plane-wave basis. **Comp. Phys. Comm.**, 147, 788–802, (2002). 26

[109] Y. Liu, D. A. Yarne, and M. E. Tuckerman. Ab initio molecular dynamics calculations with simple, localized, orthonormal real-space basis sets. **Phys. Rev. B**, 68, 125110, (2003). 26

[110] G. Hura, D. Russo, R. M. Glaeser, T. Head-Gordon, M. Krack, and M. Parrinello. Water structure as a function of temperature from X-ray scattering experiments and ab initio molecular dynamics. **Phys. Chem. Chem. Phys.**, 5, 1981–1991, (2003). 26

[111] I.-F. W. Kuo and C. J. Mundy. An ab Initio Molecular Dynamics Study of the Aqueous Liquid-Vapor Interface. **Science**, 303, 658–660, (2004). 26

[112] I.-F. W. Kuo, C. J. Mundy, M. J. McGrath, J. I. Siepmann, J. VandeVondele, M. Sprik, J. Hutter, B. Chen, M. L. Klein, F. Mohamed, M. Krack, and M. Parrinello. Liquid Water from First Principles: Investigation of Different Sampling Approaches. **J. Phys. Chem. B**, 108(34), 12990–12998, (2004). 26

[113] J. VandeVondele, F. Mohamed, M. Krack, J. Hutter, M. Sprik, and M. Parrinello. The influence of temperature and density functional models in ab initio molecular dynamics simulation of liquid water. **J. Chem. Phys.**, 122(1), No. 014515, (2005). 26

[114] S. Goedecker, M. Teter, and J. Hutter. Separable dual-space Gaussian pseudopotentials. **Phys. Rev. B**, 54(3), 1703–1710, (1996). 26, 27

[115] C. Hartwigsen, S. Goedecker, and J. Hutter. Relativistic separable dual-space Gaussian pseudopotentials from H to Rn. **Phys. Rev. B**, 58(7), 3641–3662, (1998). 26, 27, 28

[116] T. H. Dunning. Gaussian-basis sets for use in correlated molecular calculations .1. the atoms boron through neon and hydrogen. **J. Chem. Phys.**, 90(2), 1007–1023, (1989). 26, 38

[117] J. VandeVondele and J. Hutter. An efficient orbital transformation method for electronic structure calculations. **J. Chem. Phys.**, 118(10), 4365–4369, (2003). 26

[118] S. Goedecker, M. Teter, and J. Hutter. Separable dual-space Gaussian pseudopotentials. **Phys. Rev. B**, 54(3), 1703–1710, (1996). 27, 66, 78, 85

[119] A. D. Becke. Density-functional exchange-energy approximation with correct asymptotic-behavior. **Phys. Rev. A**, 38(6), 3098–3100, (1988). 28, 30

[120] C. T. Lee, W. T. Yang, and R. G. Parr. Development of the Colle-Salvetti correlation-energy formula into a functional of the electron-density. **Phys. Rev. B**, 37(2), 785–789, (1988). 28, 30

[121] B. Miehlich, A. Savin, H. Stoll, and H. Preuss. Results obtained with the correlation-energy density functionals of Becke and Lee, Yang and Parr. **Chem. Phys. Lett.**, 157(3), 200–206, (1989). 28, 30

[122] J. P. Perdew. Density-functional approximation for the correlation-energy of the inhomogeneous electron-gas. **Phys. Rev. B**, 33(12), 8822–8824, (1986). 28

[123] F. A. Hamprecht, A. J. Cohen, D. J. Tozer, and N. C. Handy. Development and assessment of new exchange-correlation functionals. **J. Chem. Phys.**, 109(15), 6264–6271, (1998). 28, 30

[124] J. P. Perdew, K. Burke, and M. Ernzerhof. Generalized gradient approximation made simple. **Phys. Rev. Lett.**, 77(18), 3865–3868, (1996). 28, 30, 94, 95

[125] M. P. Allen and D. J. Tildesley. **Computer Simulations of Liquids**. Claredon Press, Oxford, (1987). 28

[126] A. D. Boese, N. L. Doltsinis, N. C. Handy, and M. Sprik. New generalized gradient approximation functionals. **J. Chem. Phys.**, 112(4), 1670–1678, (2000). 30

[127] A. D. Boese and N. C. Handy. A new parametrization of exchange-correlation generalized gradient approximation functionals. **J. Chem. Phys.**, 114(13), 5497–5503, (2001). 30

[128] N. C. Handy and A. J. Cohen. A dynamical correlation functional. **J. Chem. Phys.**, 116(13), 5411–5418, (2002). 30

[129] J. M. Tao, J. P. Perdew, V. N. Staroverov, and G. E. Scuseria. Climbing the density functional ladder: Nonempirical meta-generalized gradient approximation designed for molecules and solids. **Phys. Rev. Lett.**, 91(212), 146401–1, (2003). 30

[130] A. D. Becke. A new mixing of Hartree-Fock and local density-functional theories. **J. Chem. Phys.**, 98(2), 1372–1377, (1993). 30

[131] A. D. Becke. Density-functional thermochemistry. III. The role of exact exchange. **J. Chem. Phys.**, 98(7), 5648–5652, (1993). 30

[132] P. J. Stephens, F. J. Devlin, C. F. Chabalowski, and M. J. Frisch. Ab Initio Calculation of Vibrational Absorption and Circular Dichroism Spectra Using Density Functional Force Fields. **J. Phys. Chem.**, 98(45), 11623–11627, (1994). 30

[133] J. A. White and D. M. Bird. Implementation of gradient-corrected exchange-correlation potentials in Car-Parrinello total-energy calculations. **Phys. Rev. B**, 50(7), 4954–4957, (1994). 31

[134] L. C. Balbás, J. L. Martins, and J. M. Soler. Evaluation of exchange-correlation energy, potential, and stress. **Phys. Rev. B**, 64(15), No. 165110, (2001). 31

[135] A. D. Becke. A multicenter numerical integration scheme for polyatomic molecules. **J. Chem. Phys.**, 88(4), 2543–2553, (1988). 31

[136] C. W. Murray, N. C. Handy, and G. J. Laming. Quadrature schemes for integrals of density functional theory. **Mol. Phys.**, 78, 997–1014, (1993). 31

[137] O. T. Treutler and R. Ahlrichs. Efficient molecular numerical integration schemes. **J. Chem. Phys.**, 102, 346–354, (1995). 31

[138] S. G. Louie, S. Froyen, and M. L. Cohen. Nonlinear ionic pseudopotentials in spin-density-functional calculations. **Phys. Rev. B**, 26(4), 1738–1742, (1982). 33

[139] P. Pulay. Ab initio calculation of force constants and equilibrium geometries in polyatomic molecules. I. theory. **Mol. Phys.**, 17(2), 197–204, (1969). 36, 37

[140] T. Helgaker and P. R. Taylor. **Modern Electronic Structure Theory, Part II**. World Scientific, Singapore, (1995). 37

[141] EMSL Gaussian Basis Set Order Form. http://www.emsl.pnl.gov/forms/basisform.html. 37

[142] D. E. Woon and T. H. Dunning. Gaussian-basis sets for use in correlated molecular calculations. III. The atoms aluminum through argon. **J. Chem. Phys.**, 98(2), 1358–1371, (1993). 38

[143] D.C. Rapaport. **The Art of molecular dynamics simulation**. University Press, Cambridge, Cambridge, (1998). 40

[144] J. Lennard-Jones. Cohesion. **Proceedings of the Physical Society**, 43(1), 461–482, (1931). 43

[145] P. Vashishta, R. K. Kalia, J. P. Rino, and I. Ebbsjö. Interaction potential for SiO_2: A molecular-dynamics study of structural correlations. **Phys. Rev. B**, 41(17), 12197–12209, (1990). 43

[146] J. Tersoff. New empirical model for the structural properties of silicon. **Phys. Rev. Lett.**, 56(6), 632–635, (1986). 43

[147] K. Sharp. Incorporating solvent ion screening into molecular dynamics using the finite difference Poisson-Boltzmann method. **J. Comput. Chem.**, 12(4), 454–468, (1991). 44

[148] M.K. Gilson. Molecular dynamics simulation with a continuum electrostatic model of the solvent. **J. Comput. Chem.**, 16(9), 1081–1095, (1995). 44

[149] R. Zhou and B.J. Berne. Can a continuum solvent model reproduce the free energy landscape of a β-hairpin folding in water? **Proc. Nat. Ac. Soc.**, 99(20), 12777–12782, (2002). 44

[150] R. S. Mulliken. Electronic Population Analysis on LCAOMO Molecular Wave Functions. I. **J. Chem. Phys.**, 23(10), 1833–1840, (1955). 44

[151] R. S. Mulliken. Electronic Population Analysis on LCAOMO Molecular Wave Functions. II. Overlap Populations, Bond Orders, and Covalent Bond Energies. **J. Chem. Phys.**, 23(10), 1841–1846, (1955). 44

[152] R. S. Mulliken. Electronic Population Analysis on LCAO-MO Molecular Wave Functions. III. Effects of Hybridization on Overlap and Gross AO Populations. **J. Chem. Phys.**, 23(12), 2338–2342, (1955). 44

[153] R. S. Mulliken. Electronic Population Analysis on LCAO-MO Molecular Wave Functions. IV. Bonding and Antibonding in LCAO and Valence-Bond Theories. **J. Chem. Phys.**, 23(12), 2343–2346, (1955). 44

[154] R. S. Mulliken. Criteria for the Construction of Good Self-Consistent-Field Molecular Orbital Wave Functions, and the Significance of LCAO-MO Population Analysis. **J. Chem. Phys.**, 36(12), 3428–3439, (1956). 44

[155] P.-O. Löwdin. On the Non-Orthogonality Problem Connected with the Use of Atomic Wave Functions in the Theory of Molecules and Crystals. **J. Chem. Phys.**, 18(3), 365, (1950). 44

[156] F. J. Momany. Determination of partial atomic charges from ab initio molecular electrostatic potentials. Application to formamide, methanol, and formic acid. **J. Phys. Chem.**, 82(5), 592–601, (1978). 44

[157] S. R. Cox and D. E. Williams. Representation of the molecular electrostatic potential by a net atomic charge model. **J. Comput. Chem.**, 2(3), 304–323, (1981). 44

[158] C. I. Bayly, P. Cieplak, W. D. Cornell, and P. A. Kollman. A well-behaved electrostatic potential based method using charge restraints for deriving atomic charges: the RESP model. **J. Phys. Chem.**, 97(40), 10269–10280, (1993). 44

[159] A. Laio, J. VandeVondele, and U. Röthlisberger. D-RESP: Dynamically Generated Electrostatic Potential Derived Charges from Quantum Mechanics/Molecular Mechanics Simulations. **J. Phys. Chem. B**, 106(29), 7300–7307, (2002). 44

[160] S. Lifson, A.T. Hagler, and P. Dauber. Consistent Force-Fields studies of intermolecular forces in hydrogen bonded crystals.1. Carboxylic acids, amides and the C=O...H - Hydrogen bonds. **J. Am. Chem. Soc.**, 101(18), 5111–5121, (1979). 44

[161] M.P. Allen and D.J. Tildesley. **Computer Simulation of Liquids**. Oxford University Press, Oxford, (1987). 45

[162] A. Warshel. Bicycle-pedal model for the first step in the vision process. **Nature**, 260(5553), 679–683, (1976). 45

[163] J.A. McCammon, B.R. Gelin, and M. Karplus. Dynamics of folded Proteins. **Nature**, 267(5612), 585–590, (1977). 45

[164] M. Levitt. Molecular dynamics of native proteins. II. analysis and nature of motion. **J. Mol. Biol.**, 168(3), 621–657, (1983). 45

[165] D. Das, K. P. Eurenius, E. M. Billings, P. Sherwood, D. C. Chatfield, M. Hodoscek, and B. R. Brooks. Optimization of quantum mechanical molecular mechanical partitioning schemes: Gaussian delocalization of molecular mechanical charges and the double link atom method. **J. Chem. Phys.**, 117(23), 10534–10547, (2002). 49, 50, 52

[166] M. J. Field, P. A. Bash, and M. Karplus. A combined quantum-mechanical and molecular mechanical potential for molecular-dynamics simulations. **J. Comput. Chem.**, 11(6), 700–733, (1990). 50, 58

[167] D. A. McQuarrie. **Statistical Mechanics**. University Science Books, Sausalito, CA, (2000). p. 234. 50

[168] P. K. Biswas. A new ab initio method of calculating Zeff and hence the positron annihilation rates using T-matrix scattering amplitudes. **Eur. Phys. J. D**, 29(1), 321–327, (2004). 52

[169] G. Karlström, R. Lindh, P.-A. Malmqvist, B. O. Roos, U. Ryde, V. Veryazov, P.-O. Widmark, M. Cossi, B. Schimmelpfennig, P. Neogrady, and L. Seijo. MOLCAS: a program package for computational chemistry. **Computational Material Science**, 28(2), 222, (2003). 57

[170] M. W. Schmidt, K. K. Baldridge, J. A. Boatz, S. T. Elbert, M. S. Gordon, J. H. Jensen, S. Koseki, N. Matsunaga, K. A. Nguyen, S. Su, T. L. Windus, M. Dupuis, and J. A. Montgomery. General atomic and molecular electronic-structure system. **J. Comput. Chem.**, 14(11), 1347–1363, (1993). 57

[171] CPMD, Version 3.9.1. copyright IBM Corp. 1990-2005, copyright MPI für Festkörperforschung Stuttgart 1997-2005; http://www.cpmd.org/. 57, 65, 91

[172] L. Fusti-Molnar and P. Pulay. Accurate molecular integrals and energies using combined plane wave and Gaussian basis sets in molecular electronic structure theory. **J. Chem. Phys.**, 116(18), 7795–7805, (2002). 57

[173] M. Eichinger, P. Tavan, J. Hutter, and M. Parrinello. A hybrid method for solutes in complex solvents: Density functional theory combined with empirical force fields. **J. Chem. Phys.**, 110(21), 10452–10467, (1999). 57, 66

[174] P. Sherwood. **Modern Methods and Algorithms of Quantum Chemistry**, volume 1 of **NIC Series**, Hybrid quantum mechanics/molecular mechanics approaches, pages 257–277. John von Neumann Institute for Computing, (2000). 58, 84

[175] T. Laino. ˙The Mathematica Notebook used to develop the GEEP technology is part of the CP2K distribution and can be freely downloaded. Released under GPL license. 59

[176] W. Hackbusch. **Multi-Grid Methods and Applications**, volume 4 of **Series in Computational Mathematics**. Springer Verlag, Berlin, (1985). 61

[177] W.L. Briggs. **A Multigrid Tutorial**. SIAM Books, Philadelphia, (1987). 61

[178] G. Feng. Data smoothing by cubic spline filters. **IEEE Trans.on Signal Process.**, 46(10), 2790–2796, (1998). 61

[179] P. Pulay. Ab initio calculation of force constants and equilibrium geometries in polyatomic molecules .I. Theory. **Mol. Phys.**, 17(2), 197–204, (1969). 64

[180] H. J. C. Berendsen, J. P. M. Postma, W. F. van Gunsteren, and J. Hermans. **Intermolecular Forces**, Interaction models for water in relation to protein hydration, pages 331–342. Reidel, Dordrecht, The Netherlands, (1981). 65

[181] A. D. Becke. Density-Functional Exchange-energy approximation with correct asymptotic-behavior. **Phys. Rev. A**, 38(6), 3098–3100, (1988). 66

[182] C. Lee, W. Yang, and R.G. Parr. Development of the Colle-Salvetti correlation-energy formula into a functional of the electron density. **Phys. Rev. B**, 37(2), 785–789, (1988). 66

[183] C. Sagui and A. Darden. Molecular Dynamics simulations of biomolecules: Long-Range electrostatic effects. **Ann. Rev. Biophys. Biomol. Struct.**, 28, 155–179, (1999). 69

[184] H. Resat and J. A. McCammon. Free energy simulations: Correcting for electrostatic cutoffs by use of the Poisson equation. **J. Chem. Phys.**, 104(19), 7645–7651, (1996). 69

[185] G. S. Del Buono, T. S. Cohen, and P. J. Rossky. Effects of long-range interactions on the dynamics of ions in aqueous-solution. **J. Mol. Liq.**, 60(1-3), 221–236, (1994). 69

[186] H. Resat. Correcting for solvent-solvent electrostatic cutoffs considerably improves the ion-pair potential of mean force. **J. Chem. Phys.**, 110(14), 6887–6889, (1999). 69

[187] X. Rozanska and C. Chipot. Modeling ion-ion interaction in proteins: A molecular dynamics free energy calculation of the guanidinium-acetate association. **J. Chem. Phys.**, 112(22), 9691–9694, (2000). 69

[188] M. Brunsteiner and S. Boresch. Influence of the treatment of electrostatic interactions on the results of free energy calculations of dipolar systems. **J. Chem. Phys.**, 112(16), 6953–6955, (2000). 69

[189] D. M. York, T. A. Darden, and L. G. Pedersen. The effect of long-range electrostatic interactions in simulations of macromolecular crystals - A comparison of the ewald and truncated list methods. **J. Chem. Phys.**, 99(10), 8345–8349, (1993). 69

[190] P. P. Ewald. The calculation of optical and electrostatic grid potential. **Ann. Phys.**, 64(3), 253–287, (1921). 69, 72, 73, 74

[191] A. Y. Toukmaji and J. A. Board Jr. Ewald summation techniques in perspective: a survey. **Comp. Phys. Comm.**, 95(2-3), 73–92, (1995). 69

[192] M. Deserno and C. Holm. How to mesh up Ewald sums. I. A theoretical and numerical comparison of various particle mesh routines. **J. Chem. Phys.**, 109(18), 7678–7693, (1998). 69, 72

[193] U. Essmann, L. Perera, M. L. Berkowitz, T. Darden, H. Lee, and L. G. Pedersen. A smooth particle mesh ewald method. **J. Chem. Phys**, 103(19), 8577–8593, (1995). 69

[194] T. Darden, D. York, and L. Pedersen. Particle mesh ewald - an N log(N) method for ewald sums in large systems. **J. Chem. Phys.**, 98(12), 10089–10092, (1993). 69, 72

[195] Y. Shan, J. L. Klepeis, M. P. Eastwood, R. O. Dror, and D. E. Shaw. Gaussian split Ewald: A fast Ewald mesh method for molecular simulation. **J. Chem. Phys.**, 122(5), No. 054101, (2005). 69

[196] A. Tongraar, K. R. Liedl, and B. M. Rode. Born-Oppenheimer ab initio QM/MM dynamics simulations of Na+ and K+ in water: From structure making to structure breaking effects. **J. Phys. Chem. A**, 102(50), 10340–10347, (1998). 69

[197] A. Tongraar and B. M. Rode. A Born-Oppenheimer ab initio quantum mechanical/molecular mechanical molecular dynamics simulation on preferential solvation of Na+ in aqueous ammonia solution. **J. Phys. Chem. A**, 105(2), 506–510, (2001). 69

[198] C. F. Schwenk, H. H. Loeffler, and B. M. Rode. Structure and dynamics of metal ions in solution: QM/MM molecular dynamics simulations of Mn2+ and V2+. **J. Am. Chem. Soc.**, 125(6), 1618–1624, (2003). 69

[199] S. Chalmet and M. F. Ruiz-Lopez. The reaction field of a water molecule in liquid water: Comparison of different quantum/classical models. **J. Chem. Phys.**, 115(11), 5220–5227, (2001). 69

[200] S. Chalmet, D. Rinaldi, and M. F. Ruiz-Lopez. A QM/MM/continuum model for computations in solution: Comparison with QM/MM molecular dynamics simulations. **Int. J. Quant. Chem.**, 84(5), 559–564, (2001). 69

[201] P. Bandyopadhyay and M. S. Gordon. A combined discrete/continuum solvation model: Application to glycine. **J. Chem. Phys.**, 113(3), 1104–1109, (2000). 69

[202] J. Gao and C. Alhambra. A hybrid semiempirical quantum mechanical and lattice-sum method for electrostatic interactions in fluid simulations. **J. Chem. Phys.**, 107(4), 1212–1217, (1997). 69

[203] K. Nam, J. Gao, and D. M. York. An efficient linear-scaling Ewald method for long-range electrostatic interactions in combined QM/MM calculations. **J. Chem. Theory Comp.**, 1(1), 2–13, (2005). 70

[204] F. Dehez, M. T. C. Martins-Costa, D. Rinaldi, and C. Millot. Long-range electrostatic interactions in hybrid quantum and molecular mechanical dynamics using a lattice summation approach. **J. Chem. Phys.**, 122(23), No. 234503, (2005). 70

[205] D. A. Yarne, M. E. Tuckerman, and G. J. Martyna. A dual length scale method for plane-wave-based, simulation studies of chemical systems modeled using mixed ab initio/empirical force field descriptions. **J. Chem. Phys.**, 115(8), 3531–3539, (2001). 70, 78

[206] F. Zipoli, T. Laino, A. Laio, M. Bernasconi, and M. Parrinello. A QUICKSTEP -based quantum mechanics/molecular mechanics approach for silica. **J. Chem. Phys.**, 124(15), No. 154707, (2006). 70, 78

[207] M. Allen and D. Tildesley. **Computer Simulation of Liquids**. Oxford University Press, Oxford, (1987). 73

[208] G. Lippert, J.E. Hutter, and M. Parrinello. The Gaussian and augmented-plane-wave density functional method for ab initio molecular dynamics simulations. **Theor. Chem. Acc.**, 103(2), 124–140, (1999). 74, 114, 121

[209] G. J. Martyna and M. E. Tuckerman. A reciprocal space based method for treating long range interactions in ab initio and force-field-based calculations in clusters. **J. Chem. Phys**, 110(6), 2810–2821, (1999). 75, 78

[210] P. E. Blöchl. Density derived atomic point charges. **J. Chem. Phys.**, 103(17), 7422–7428, (1995). 75, 76, 78, 100

[211] L. Levien, C. T. Prewitt, and D. J. Weidner. Structure and elastic properties of quartz at pressure. **Am. Mineral.**, 65(9-10), 920–930, (1980). 76, 88

[212] C. M. Nelson and R. A. Weeks. Trapped electrons in irradiated quartz and silica. 1. Optical Absorption. **J. Am. Ceram. Soc.**, 43(8), 396–399, (1960). 76, 94

[213] R. A. Weeks. Paramagnetic resonance of lattice defects in irradiated quartz. **J. Appl. Phys.**, 27(11), 1376–1381, (1956). 76, 94

[214] R. A. Weeks and C. M. Nelson. Trapped electrons in irradiated quartz and silica .2. Electron spin resonance. **J. Am. Ceram. Soc.**, 43(8), 399–404, (1960). 76, 94

[215] R. H. Silsbee. Electron spin resonance in neutron-irradiated quartz. **J. Appl. Phys.**, 32(8), 1459–1461, (1961). 76, 94

[216] M. G. Jani, R. B. Bossoli, and L. E. Halliburton. Further characterization of the E_1' center in crystalline SiO2. **Phys. Rev. B**, 27(4), 2285–2293, (1983). 76, 94

[217] W. L. Warren, E. H. Poindexter, M. Offenberg, and W. Müller-Warmuth. Paramagnetic point-defects in amorphous-silicon dioxide and amorphous-silicon nitride thin-films .1. a-SiO2. **J. Electrochem. Soc.**, 139(3), 872–880, (1992). 76, 94

[218] E. H. Poindexter and W. L. Warren. Paramagnetic point-defects in amorphous thin-films of SiO2 and Si3N4 - Updates and additions. **J. Electrochem. Soc.**, 142(7), 2508–2516, (1995). 76, 94

[219] D. R. Hamann. Generalized Gradient Theory for Silica Phase Transitions. **Phys. Rev. Lett.**, 76(4), 660–663, (1996). 76

[220] P. E. Blöchl. First-Principles calculations of defects in oxygen-deficient silica exposed to hydrogen. **Phys. Rev. B**, 62(10), 6158–6179, (2000). 76, 78, 79, 94, 95, 97, 99, 101

[221] K. C. Snyder and W. B. Fowler. Oxygen vacancy in alpha-quartz - A possible bistable and metastable defect. **Phys. Rev. B**, 48(18), 13238–13243, (1993). 76, 94

[222] D. C. Allan and M. P. Teter. Local density approximation total energy calculations for silica and titania structure and defects. **J. Am. Ceram. Soc.**, 73(11), 3247–3250, (1990). 76, 88, 94

[223] M. Boero, A. Pasquarello, J. Sarnthein, and R. Car. Structure and hyperfine parameters of E'(1) centers in a-quartz and in vitreous SiO2. **Phys. Rev. Lett.**, 78(5), 887–890, (1997). 76, 94, 95, 97, 99

[224] G. Pacchioni and G. Ierano. Optical absorption and nonradiative decay mechanism of E_1' center in silica. **Phys. Rev. Lett.**, 81(2), 377–380, (1998). 76, 93, 94

[225] A. H. Edwards and W. B. Fowler. Semi-empirical molecular-orbital techniques applied to silicon dioxide - MINDO/3. **J. Phys. Chem. Solids**, 46(7), 841–857, (1985). 76, 94

[226] J. K. Rudra and W. B. Fowler. Oxygen vacancy and the E_1' center in crystalline SiO2. **Phys. Rev. B**, 35(15), 8223–8230, (1987). 76, 94

[227] G. Pacchioni, A. M. Ferrari, and G. Ierano. Cluster model calculations of oxygen vacancies in SiO2 and MgO - Formation energies, optical transitions and EPR spectra. **Faraday Discuss.**, 106(1), 155–172, (1997). 76, 88, 94

[228] J. Sauer and M. Sierka. Combining quantum mechanics and interatomic potential functions in ab initio studies of extended systems. **J. Comput. Chem.**, 21(16), 1470–1493, (2000). 78, 84, 88

[229] V.B. Sulimov, P.V. Sushko, A.L. Shluger A.H. Edwards, and A.M. Stoneham. Asymmetry and long-range character of lattice deformation by neutral oxygen vacancy in alpha-quartz. **Phys. Rev. B**, 66(2), 24108–24114, (2002). 78, 84, 85, 88, 90, 94, 97

[230] A.S. Mysovsky, P.V. Sushko, A.H. Edwards S. Mukhopadhyay, and A.L. Shluger. Calibration of embedded-cluster method for defect studies in amorphous silica. **Phys. Rev. B**, 69(8), No.085202, (2004). 78, 84, 94, 97

[231] V.B. Sulimov, S. Casassa, C. Pisani, J. Garapon, and B. Poumellac. Embedded cluster ab initio study of the neutral oxygen vacancy in quartz and cristobalite. **Modell. Simul. Mater. Sci. Eng.**, 8(5), 763–773, (2000). 78, 84

[232] C. Pisani, M. Busso, F. Lopez-Gejo, S. Casassa, and L. Maschio. Quasi-periodic ab initio models in material science: the case of oxygen-deficient centers in optical fibers. **Theor. Chem. Acc.**, 111(2-6), 246–254, (2004). 78, 84

[233] D. Erbetta, D. Ricci, and G. Pacchioni. Simplified embedding schemes for the quantum-chemical description of neutral and charged point defects in SiO2 and related dielectrics. **J. Chem. Phys.**, 113(23), 10744–10752, (2000). 78, 84

[234] V.A. Nasluzov, E.A. Ivanova, A.M. Shor, G.N. Vayssilov, U. Birkenheuer, and N. Rosch. Elastic polarizable environment cluster embedding approach for covalent oxides and zeolites based on a density functional method. **J. Phys. Chem. B**, 107(10), 2228–2241, (2003). 78, 84

[235] J.S. Tse, D.D. Klug, and Y.L. Page. High-pressure densification of amorphous silica. **Phys. Rev. B**, 46(10), 5933–5938, (1992). 78, 85

[236] H. R. Philipp. Optical transitions in crystalline and fused quartz. **Solid State Comm.**, 4(1), 73–75, (1966). 78

[237] S. Miyazaki, H. Nishimura, M. Fukuda, L. Ley, and J. Ristein. Structure and electronic states of ultrathin SiO2 thermally grown on Si(100) and Si(111) surfaces. **Appl. Surf. Sci.**, 114, 585–589, (1997). 78

[238] G. Pacchioni, L. Skuja, and D. L. Griscom, editors. **Defects in SiO_2 and Related Dielectrics: Science and Technology**. Kluwer Academic Publisher, (2000). 83

[239] J. Sarnthein, A. Pasquarello, and R. Car. Origin of the high-frequency doublet in the vibrational spectrum of vitreous SiO2. **Science**, 275(5308), 1925–1927, (1997). 83

[240] N. Binggeli and J.R. Chelikowsky. Structural transformation of quartz at high-pressures. **Nature**, 353(6342), 344–346, (1991). 83

[241] L.S. Dubrovinsky, S.K. Saxena, P. Lazor, R. Ahuja, O. Eriksson, J.M. Wills, and B. Johansson. Experimental and theoretical identification of a new high-pressure phase of silica. **Nature**, 388(6640), 362–365, (1997). 83

[242] M.-H. Du and H.-P. Cheng. Transparent interface between classical molecular dynamics and first-principles molecular dynamics. **Int. J. Quant. Chem.**, 93(1), 1–8, (2003). 84, 88

[243] M.-H. Du, A. Kolchin, and H.-P. Cheng. Water-silica surface interactions: A combined quantum-classical molecular dynamic study of energetics and reaction pathways. **J. Chem. Phys.**, 119(13), 6418–6422, (2003). 84, 88

[244] I. Laika-Voivod, F. Sciortino, T. Grande, and P.H. Poole. Phase diagram of silica from computer simulation. **Phys. Rev. E**, 70(6), No. 61507, (2004). 85

[245] C.S. Carmer, B. Weiner, and M. Frenklach. Molecular-dynamics with combined quantum and empirical potentials - C2H2 adsorption on Si(100). **J. Chem. Phys.**, 99(2), 1356–1372, (1993). 85

[246] J.R. Shoemaker, L.W. Burggraf, and M.S. Gordon. SIMOMM: An integrated molecular orbital/molecular mechanics optimization scheme for surfaces. **J. Phys. Chem. A**, 103(17), 3245–3251, (1999). 85

[247] M. Frenklach, M. Skokov, and B. Weiner. An atomistic model for stepped diamond growth. **Nature**, 372(6506), 535–537, (1994). 85

[248] V. Kairys and J.H. Jensen. QM/MM Boundaries Across Covalent Bonds: A Frozen Localized Molecular Orbital-Based Approach for the Effective Fragment Potential Method. **J. Phys. Chem. A**, 104(28), 6656–6665, (2000). 85

[249] R. Murphy, D. Philipp, and R. Friesner. A mixed quantum mechanics/molecular mechanics (QM/MM) method for large-scale modeling of chemistry in protein environments. **J. Comput. Chem.**, 21(16), 1442–1447, (2000). 85

[250] T. Narasimhamurty. Photoelastic constants of alpha-quartz. **J. Opt. Soc. Am.**, 59(6), 682–686, (1969). 88

[251] C.M. Carbonaro, V. Fiorentini, and S. Massidda. Ab initio study of oxygen vacancies in alpha-quartz. **J. Non-Cryst. Solids**, 221(1), 89–96, (1997). 88

[252] N. Capron, S. Carniato, A. Lagraa, and G. Boureau. Local density approximation and generalized gradient approximation calculations for oxygen and silicon vacancies in silica. **J. Chem. Phys.**, 112(21), 9543–9548, (2000). 88

[253] B.B. Stefanov and K. Raghavachari. Photoabsorption of the neutral oxygen vacancy in silicate and germanosilicate glasses: First-principles calculations. **Phys. Rev. B**, 56(9), 5035–5038, (1997). 88

[254] G. Boureau and S. Carniato. Apparent discrepancies between thermodynamic data and theoretical calculations of the formation energy of an oxygen vacancy in silica. **Solid State Commun.**, 98(6), 485–487, (1996). Correction in **Solid State Commun.** 99(1), R1-R4 (1996). 88

[255] D.R. Lide, editor. **CRC Handbook of Chemistry and Physics**. CRC Press, 78th edition edition, (1997-1998). 89

[256] Frank Jensen. **Introduction to Computational Chemistry,**. John Wiley & Sons, (1999). 89

[257] S. Baroni, S. de Gironcoli, A. Dal Corso, and P. Giannozzi. Phonons and related crystal properties from density-functional perturbation theory. **Rev. Mod. Phys.**, 73(2), 515, (2001). 91

[258] T. Laino. ˙For the CPMD calculations we have used norm-conserving pseudopotentials and plane wave expansion of the Kohn-Sham orbitals up to a kinetic cutoff of 90 Ry. The disilane molecule is at the center of a cubic box of edge 15 Å. 91

[259] G. Roma, Y. Limoge, and S. Baroni. Oxygen self-diffusion in alpha-quartz. **Phys. Rev. Lett.**, 86(20), 4564–4567, (2001). 91

[260] K. O. Hill, Y. Fujii, D. C. Johnson, and B. S. Kawasaki. Photosensitivity in optical fiber waveguides - Application to reflection filter fabrication. **Appl. Phys. Lett.**, 32(10), 647–649, (1978). 93

[261] R. A. Myers, N. Mukherjee, and S.R.I. Brueck. Large second-order nonlinearity in poled fused silica. **Opt. Lett.**, 16(22), 1732–1735, (1991). 93

[262] E. Franchina, C. Corbari, P.G. Kazansky, N. Chiodini, A. Lauria, and A. Paleari. Oxygen-deficiency effect on thermal poling of silica-based glasses. **Solid State Comm.**, 136(5), 300–303, (2005). 93

[263] D. Griscom and E. J. Friebele. Fundamental radiation-induced defect centers in synthetic fused silicas - atomic chlorine, delocalized e' centers, and a triplet-state. **Phys. Rev. B**, 34(11), 7524–7533, (1986). 93, 94, 101

[264] C.M. Carbonaro, V. Fiorentini, and F. Bernardini. Proof of the Thermodynamical Stability of the E000 Center in SiO_2. **Phys. Rev. Lett.**, 86(14), 3064–3067, (2000). 93, 94

[265] F. J. Feigl, W. L. Fowler, and K. L. Yip. Oxygen vacancy model for E_1' center in SiO2. **Solid State Comm.**, 14(3), 225–229, (1974). 94

[266] K. L. Yip and W. B. Fowler. Electronic structure of E_1' centers in SiO2. **Phys. Rev. B**, 11(6), 2327–2338, (1975). 94

[267] E. P. O'Reilly and J. Robertson. Theory of defects in vitreous silicon dioxide. **Phys. Rev. B**, 27(6), 3780–3795, (1983). 94

[268] J.P. Perdew and A. Zunger. Self-interaction correction to density-functional approximations for many-electron systems. **Phys. Rev. B**, 23(10), 5048–5079, (1981). 94, 100

[269] V. B. Sulimov, V. O. Sokolov, E. M. Dianov, and B. Poumellec. Photoinduced structural transformations in silica glass: the role of oxygen vacancies in the mechanism of formation of refractive-index gratings by UV irradiation of optical fibres. **QUANTUM ELECTRON**, 26(11), 988–993, (1996). 94

[270] J.P. Perdew and Y. Wang. Accurate and simple analytic representation of the electron-gas correlation energy. **Phys. Rev. B**, 45(23), 13244–13249, (1992). 95

[271] G. Mills and H. Jónsson. Quantum and thermal effects in H-2 dissociative adsorption - Evaluation of free-energy barriers in multidimensional quantum-systems. **Phys. Rev. Lett.**, 72(7), 1124–1127, (1994). 96, 99

[272] G. Mills, H. Jónsson, and G. Schenter. Reversible work transition-state theory - Application to dissociative adsorption of hydrogen. **Surf. Sci.**, 324(2-3), 305–337, (1995). 96, 99

[273] G. Henkelman and H. Jónsson. Improved tangent estimate in the nudged elastic band method for finding minimum energy paths and saddle points. **J. Chem. Phys.**, 113(22), 9978–9985, (2000). 96, 99

[274] D. Donadio, M. Bernasconi, and M. Boero. Ab initio Simulations of Photoinduced Interconversions of Oxygen Deficient Centers in Amorphous Silica. **Phys. Rev. Lett.**, 87(19), 195504–195507, (2001). 97

[275] Y. Zhang and W. Yang. A challenge for density functionals: Self-interaction error increases for systems with a noninteger number of electrons. **J. Chem. Phys.**, 109(7), 2604–2608, (1998). 100

[276] S.F. Boys. Electronic Wave Functions.I. A General Method of Calculation for the Stationary States of Any Molecular System. **Proc. Roy. Soc. A**, 200(1063), 542, (1950). 110

[277] M. Primorac. New Expansion of the Boys Function. **Int. J. Quant. Chem.**, 68(5), 305–315, (1998). 110

[278] R. P. Feynman, R. B. Leighton, and M. Sands. **The Feynman Lectures on Physics**, volume 1. Addison-Wesley, xs, (1963). 30-11. 117